UNIVERSITY OF CALIFORNIA,
IRVINE

SEARCHES FOR EXOTIC BARYON NUMBER-VIOLATING PROCESSES AT SUPER-KAMIOKANDE

DISSERTATION

submitted in partial satisfaction of the requirements
for the degree of

DOCTOR OF PHILOSOPHY

in Physics

by

Volodymyr Takhistov

Dissertation Committee:
Professor Henry W. Sobel, Chair
Professor Mu-Chun Chen
Professor William R. Molzon

2016

TABLE OF CONTENTS

LIST OF FIGURES

LIST OF TABLES

ACKNOWLEDGMENTS

First and foremost, I would like to express significant gratitude to Hank Sobel. I have been tremendously lucky to have him as my advisor. He has believed in me and provided me with unparalleled support, encouragement and freedom to pursue orthogonally-related projects throughout my studies. I am not sure my "ventures" into both theoretical and experimental physics would have been possible if I had another advisor. He was always available to consult and assist me with any issues that might have occurred and I can't thank him enough for this. Additionally, he was willing to seriously entertain any random idea that I had whilst walking to his office, even if it was nonsense. Despite having a long and successful career, I have seen him many times discussing with great passion new developments in science and technology, even unrelated to his field. He is a prime example of a gentleman and a scientist, in the best connotations associated with these words. I know of many good things that have happened because of his leadership and involvement (direct or indirect).

I would also like to express large appreciation to Mu-Chun Chen, who has acted as my unofficial advisor for theoretical work. She has agreed to work with me while knowing about my involvement with experiment and has been very understanding. I would like to especially thank her for patience and bearing with my stubbornness in general. Thanks to her support, I was able to attend various theoretical physics schools, which proved to be a very positive experience. She has also been very encouraging of me proceeding, unimpeded, in directions different to the original research themes that we were working on, catering to my interests. I really appreciate this.

My best regards are extended to Ed Kearns, one of the conveners of the Super-Kamiokande nucleon decay and atmospheric neutrino (high energy) group. Many times has he provided me with mentorship and encouragement on work not only related to Super-Kamiokande, but also on scientific ventures in general. A lot of the Super-Kamiokande analysis results would have been drastically weaker (or not possible at all) without his input and general knowledge of many areas of physics. He is one of the leading world experts on nucleon decay and it has been a pleasure working with him.

Additionally, I would like to thank Michael Smy, Shunichi Mine and Roger Wendell, with whom I have closely collaborated on SK-related work. Their knowledge of Super-Kamiokande and willingness to help was instrumental in my successful and speedy completion of analyses. I would also like to stress, that Michael Smy's thorough and broad understanding of experimental techniques has been directly responsible for timely completion of more than one thesis at UCI.

I would also like to acknowledge Mark Vagins and Michael Ratz for many enlightening discussions. Collaborating with Michael Ratz, who commands vast knowledge of various topics in theoretical high energy physics, has been a valuable learning experience. I would also like to thank other faculty, students and researchers at UCI, including Bill Kropp, James Rutledge, Pearce Weatherly and Muhammad Elnimr for being helpful in various situations.

Super-Kamiokande is an international effort and would not have been possible without vigorous and extensive labor of many people, especially researchers at the Kamioka Observatory (Yasunori Hayato, Makoto Miura and others). I would especially like to accentuate Masato Shiozawa, the other convener of the SK high energy group and the person in charge of the upcoming Hyper-K experiment, for his leadership and encouragement. The first SK $p \rightarrow e^+\pi^0$ analysis, which he conducted for his 1998 PhD. work, has served as a useful guide for multiple future theses, including this one. I must also express my gratitude to Masayuki Nakahata (spokesperson of Super-K) and Yoichiro Suzuki (previous Super-K spokesperson), who with tireless effort have been steering the collaboration in the right direction for many years. Without the leadership of above individuals, it would not have been possible to maintain the high level of quality and effort that permeates all areas of Super-K work.

Finally, I would like to thank numerous other people who have been un-named but who also deserve gratitude and who have positively influenced me and my world view, including various scientists and thinkers (of past and present), friends and family. I appreciate that members of the thesis committee (Hank Sobel, Mu-Chun Chen and Bill Molzon) took the time out of their busy schedules to deal with my defense and thesis.

I acknowledge support of the U.S. Department of Energy. The Super-Kamiokande experiment was built and has been operated with funding from the Japanese Ministry of Education, Culture, Sports, Science and Technology and the U.S. National Science Foundation. Special thanks goes to Kamioka Mining and Smelting Company for helping to host the experiment.

CURRICULUM VITAE

Volodymyr Takhistov

EDUCATION

Doctor of Philosophy (PhD.), Physics **2016**
University of California, Irvine Irvine, CA, USA

Bachelor of Science (BSc.), Physics and Philosophy **2010**
Rutgers University New Brunswick, NJ, USA

SELECTED PUBLICATIONS

V. Takhistov, "Review of Nucleon Decay Searches at Super-Kamiokande", *Proc. of Moriond-2016 (Electroweak Int. and Unified Theor.)*, (2016), arXiv:1605.03235 [hep-ex]

J. Huang, M.C. Chen and V. Takhistov, "Beyond Minimal Lepton Flavored Dark Matter", *J. High Energy Phys.* **1602**, 060 (2016), arXiv:1510.04694 [hep-ph]

V. Takhistov *et. al.* (Super-Kamiokande Collaboration), "Search for Nucleon and Dinucleon Decays with an Invisible Particle and a Charged Lepton in the Final State at the Super-Kamiokande Experiment", *Phys. Rev. Lett.* **115**, 121803 (2015), arXiv:1508.05530 [hep-ex]

M.C. Chen, M. Ratz and V. Takhistov, "R-parity violation from discrete R-symmetries", *Nucl. Phys.* **B891**, 322 (2015), arXiv:1410.3474 [hep-ph]

V. Takhistov *et. al.* (Super-Kamiokande Collaboration), "Search for Trilepton Nucleon Decay via $p \to e^+\nu\nu$ and $p \to \mu^+\nu\nu$ in the Super-Kamiokande Experiment", *Phys. Rev. Lett.* **113**, 101801 (2014), arXiv:1409.1947 [hep-ex]

M.C. Chen and V. Takhistov, "Charged Lepton Spectrum Approximation in a Three Body Nucleon Decay", *Phys. Rev.* **D89**, 095003 (2014), arXiv:1402.7360 [hep-ph]

OTHER PUBLICATIONS

K. Abe *et. al.* (Super-Kamiokande Collaboration), "Real-Time Supernova Neutrino Burst Monitor at Super-Kamiokande", *Astropart. Phys.* **81**, 39 (2016), arXiv:1601.04778 [astro-ph.HE]

E. Richard *et. al.* (Super-Kamiokande Collaboration), "Measurements of the atmospheric neutrino flux by Super-Kamiokande: energy spectra, geomagnetic effects, and solar modulation", *Proc. of Sci. (Int. Cosmic Ray Conf. 2015)* **1044**, (2015) arXiv:1510.08127 [hep-ex]

Y. Zhang *et. al.* (Super-Kamiokande Collaboration), "First measurement of radioactive isotope production through cosmic-ray muon spallation in Super-Kamiokande IV", *Phys. Rev.* **D93**, 012004 (2016), arXiv:1509.08168 [hep-ex]

J. Gustafson *et. al.* (Super-Kamiokande Collaboration), "Search for dinucleon decay into pions at Super-Kamiokande", *Phys. Rev.* **D91**, 072009 (2015), arXiv:1504.01041 [hep-ex]

K. Abe *et. al.* (Super-Kamiokande Collaboration), "Test of Lorentz invariance with atmospheric neutrinos" *Phys. Rev.* **D91**, 052003 (2015), arXiv:1410.4267 [hep-ex]

K. Abe *et. al.* (Super-Kamiokande Collaboration) "Limits on sterile neutrino mixing using atmospheric neutrinos in Super-Kamiokande", *Phys. Rev.* **D91**, 052019 (2015), arXiv:1410.2008 [hep-ex]

D.D. Stancil *et. al.* (MINERνA Collaboration), "Demonstration of Communication using Neutrinos", *Mod. Phys. Lett.* **A27**, 1250077 (2012), arXiv:1203.2847 [hep-ex]

ABSTRACT OF THE DISSERTATION

SEARCHES FOR EXOTIC BARYON NUMBER-VIOLATING PROCESSES AT SUPER-KAMIOKANDE

By

Volodymyr Takhistov

Doctor of Philosophy in Physics

University of California, Irvine, 2016

Professor Henry W. Sobel, Chair

Various theoretical considerations suggest that baryon number should be violated. Nucleon decay, which typically appears within the context of unified theories, would provide a definitive signature of baryon number violation. In this dissertation, we report on the search results for $p \to e^+ X$, $p \to \mu^+$ (where X is an invisible, massless particle), $n \to \nu\gamma$, $p \to e^+\nu\nu$, $p \to \mu^+\nu\nu$, $np \to e^+\nu$, $np \to \mu^+\nu$ and $np \to \tau^+\nu$ nucleon and dinucleon decays at the Super-Kamiokande experiment. Some of these searches are novel. Using data from a combined exposure of 273.4 kton·years and a χ^2 spectral fitting technique, a search for these decays yields a result consistent with no signal. Accordingly, lower limits on the partial lifetimes of $\tau_{p\to e^+X} > 7.9 \times 10^{32}$ years, $\tau_{n\to\nu\gamma} > 5.5 \times 10^{32}$ years, $\tau_{p\to\mu^+X} > 4.1 \times 10^{32}$ years, $\tau_{p\to e^+\nu\nu} > 1.7 \times 10^{32}$ years, $\tau_{p\to\mu^+\nu\nu} > 2.2 \times 10^{32}$ years, $\tau_{np\to e^+\nu} > 2.6 \times 10^{32}$ years, $\tau_{np\to\mu^+\nu} > 2.0 \times 10^{32}$ years and $\tau_{np\to\tau^+\nu} > 3.0 \times 10^{31}$ years at a 90% confidence level are obtained. These results provide stringent test of new physics and also limit the parameter space of models that allow for such processes.

Chapter 1

Introduction

1.1 Baryon Number Violation

One of the primary goals of physics is to establish fundamental laws that govern Nature. At the microscopic level, these laws can be stated in terms of symmetries and corresponding conserved quantum numbers, which impose restrictions on particle interactions. An illustrative example of this is the baryon number (B). The conservation of B was originally proposed in 1929 by Weyl [1], to explain why protons, which make up matter and carry a charge of $B = 1$, are stable. After discovery of the positron e^+ by Anderson in 1933 [2], this issue became more pressing, since a natural question arises why the $p \to e^+\gamma$ decay is not observed. Hence, the concept of baryon number conservation was further reinforced in 1939 by Stuckelberg [3] and in 1949 by Wigner [4].

In the 1960s, a coherent relativistic quantum field theory (QFT), which describes interactions coming from three of the four known forces, has been developed. This QFT, the Standard Model (SM) of particle physics, is based on electroweak-theory combined with the strong force, but without gravity. The fundamental forces in QFTs are mathematically described by gauge (local) symmetries. In the SM, baryon number happens to be an accidental global symmetry, which ensures that protons are stable within the theory at the classical level.

Since then, various theoretical arguments have been put forward that suggest that B is only an approximate symmetry and should be violated. Already in 1966, Sakharov [5] has pointed out that to explain the observed matter-anti-matter asymmetry of the Universe [6] one needs baryon number violating processes. In fact, even within the SM itself, the baryon number is violated by a minute amount due to quantum non-perturbative effects [7]. When one ventures beyond the SM in search of a deeper underlying theory, the baryon number is also typically violated. This is the case, for example, when QFTs based on supersymmetry or Grand Unification are considered [8]. More so, in the more fundamental theories of quantum gravity, global symmetries are expected to be violated in general [9]. This issue is of some importance, since even a small amount of B-violation can have profound effect on the ultimate fate of the Universe [10]. For a comprehensive review of baryon number violation in various contexts see Ref. [11].

Thus far, baryon number violation has not been experimentally established. An observation of B-violation would not be the first time that a "non-fundamental" symmetry is found to be only approximate. Conservation of some quantities, such as the electric charge [12], CPT [13] and energy-momentum [14] follow directly from the fundamental principles on which QFTs are built: gauge invariance, Lorentz invariance and unitarity. On the other hand, several of the conservation laws which did not follow from any fundamental principles have been later found to be violated. These include: parity (P) in 1956 [15], charge conjugation combined with parity (CP) in 1964 [16], lepton family symmetries (the muon lepton symmetry (L_μ) in 1998 [17] and the electron lepton family symmetry (L_e) in 2001 [18]) as well as time reversal (T) in 2012 [19]. Since 1998, it has been established that neutrinos oscillate and thus are massive [17]. If neutrinos are found to possess Majorana mass [20], which along with the Dirac mass is one of the two options, this would indicate [21] that lepton number L is violated also. Given the above, continuation of testing B-conservation remains a high priority.

In this Thesis, we will describe searches for exotic-baryon number violating processes at a large underground water Cherenkov experiment, Super-Kamiokande (SK, Super-K) [22]. The Thesis is organized as follows. Throughout Chapter 1 we will review in more detail various theoretical motivations for baryon number violation as well as outline some of the possible experimental signatures. We then describe and motivate our analysis. In Chapter 2, we will describe the mechanism of the Cherenkov radiation and then provide an overview of the Super-Kamiokande experiment, including the description of its design and calibration. In Chapter 3, we discuss the Monte Carlo (MC) simulation for nucleon decay, SK detector as well as the atmospheric neutrino background. Then, in Chapter 4, we will outline the event reconstruction algorithms used in the experiment. Later, in Chapter 5, we describe the fully contained (FC) data reduction algorithm, used to select useful events for the physics analyses. Chapter 6 contains the actual nucleon decay analysis, including the description of the utilized data and MC samples, the event selection, systematics as well as the fitting technique and finally the results. Lastly, Chapter 7 provides a summary and gives an outlook for the future.

1.1.1 In the Standard Model

Review of the Standard Model

We start with a brief overview of the Standard Model and refer the reader to standard texts [23] for a more comprehensive description. The SM is a QFT based on the

$$SU(3)_C \times SU(2)_L \times U(1)_Y \tag{1.1}$$

gauge group. The $SU(2)_L \times U(1)_Y$ sector describes interactions of the electro-weak force, through the Glashow-Weinberg-Salam [24, 25, 26] theory. The $SU(3)_C$ sector describes the strong force interactions, which allow for confinement and asymptotic freedom [27, 28]. The field content, summarized in Table 1.1, consists of spin-0 (the Higgs boson), spin-1/2 (the matter quarks and leptons) and spin-1 (the gauge bosons) fields. The matter fields, which

Field	Spin	$SU(3)_C$	$SU(2)_L$	$U(1)_Y$	B	L
Q_L^i	1/2	**3**	**2**	1/6	1/3	0
u_R^i	1/2	**3**	**1**	2/3	1/3	0
d_R^i	1/2	**3**	**1**	-1/3	1/3	0
L_L^i	1/2	**1**	**2**	-1/2	0	1
e_R^i	1/2	**1**	**1**	-1	0	1
H	0	**1**	**2**	1/2	0	0
G_μ^A	1	**8**	**1**	0	0	0
W_μ^a	1	**1**	**3**	0	0	0
B_μ	1	**1**	**1**	0	0	0

Table 1.1: Standard Model field content and the respective symmetry transformations. Index i labels the generation.

come in three generations labeled by index i, are the left handed doublets $Q_L^i = (u_L^i, d_L^i)$ and $L_L^i = (\nu_L^i, e_L^i)$ as well as the right-handed singlets u_R^i, d_R^i and e_R^i. The gauge fields mediate the forces and are given by G_μ^A, W_μ^a and B_μ, where the indices are $A = 1, ..., 8$ and $a = 1, 2, 3$. Finally, H is the Higgs boson. The discrepancy between the description of the left- and the right-handed fields signifies that SM is a chiral theory. The field transformations under the

SM gauge groups, as well as the global baryon number B and the lepton number L, are displayed.

The Lagrangian description of the Standard Model is given by

$$\mathscr{L}_{\text{SM}} = \mathscr{L}_{\text{gauge}} + \mathscr{L}_{\text{kinetic}} + \mathscr{L}_{\text{Higgs}} + \mathscr{L}_{\text{Yukawa}} \ , \tag{1.2}$$

where the gauge and Lorentz invariant components are

$$\begin{aligned}
\mathscr{L}_{\text{gauge}} &= -\frac{1}{2}\text{Tr}(G_{\mu\nu}G^{\mu\nu}) - \frac{1}{8}\text{Tr}(W_{\mu\nu}W^{\mu\nu}) - \frac{1}{4}B_{\mu\nu}B^{\mu\nu} \\
\mathscr{L}_{\text{kinetic}} &= \overline{Q}^i_L i\not{D} Q^i_L + \overline{L}^i_L i\not{D} L^i_L + \overline{u}^i_R i\not{D} u^i_R + \overline{d}^i_R i\not{D} d^i_R + \overline{e}^i_R i\not{D} e^i_R \\
\mathscr{L}_{\text{Higgs}} &= (D_\mu H)^\dagger (D^\mu H) - \lambda\Big(H^\dagger H - \frac{v^2}{2}\Big)^2 \\
\mathscr{L}_{\text{Yukawa}} &= -Y_u^{ij}\overline{Q}\epsilon H^* u^j_R - Y_d^{ij}\overline{Q}^i_L H d^j_R - Y_e^{ij}\overline{L}^i_L H e^j_R + \text{h.c.}
\end{aligned}$$

Here, $\mathscr{L}_{\text{gauge}}$ is built from the field strength tensors $G_{\mu\nu}, W_{\mu\nu}, B_{\mu\nu}$ which are functions of the gauge fields and describe their dynamics. The spinor and color indices have been neglected. The $\mathscr{L}_{\text{kinetic}}$ component provides dynamics for the fermion matter fields. The covariant derivative D_μ, in case of the quark doublet Q^i_L, is given by

$$D_\mu = \partial_\mu + igG^A_\mu T^A + ig_2 W^a_\mu T^a + ig_1 B_\mu Y \ , \tag{1.3}$$

where T^A, T^a, Y are the $SU(3)_C$, $SU(2)_L$, $U(1)_Y$ generators and g, g_2, g_3 are the corresponding couplings. The $\mathscr{L}_{\text{Higgs}}$ sector is responsible for the Higgs kinetic and potential terms. Finally, $\mathscr{L}_{\text{Yukawa}}$ describes the (generically complex) couplings of fermions with the Higgs boson and contains the "flavor structure" of the SM. Due to the mismatch between the mass and the weak eigenstates, the up and down quark mass matrices cannot be diagonalized simultaneously. This results in the quark sector Cabbibo-Kobayashi-Maskawa (CKM) mixing [29, 30]. Similarly, the lepton sector has the Pontecorvo-Maki-Nakagawa-Sakata (PMNS) mixing[1] [31, 32, 33].

The $SU(2)_L \times U(1)_Y$ sector is spontaneously broken down to the electromagnetic (EM) $U(1)_{EM}$, according do the "Higgs mechanism" [34, 35, 36]. This is implemented by having the Higgs doublet acquire a vacuum expectation value (vev)

$$H = \begin{pmatrix} H^+ \\ H^0 \end{pmatrix} \rightarrow \langle H \rangle = \frac{1}{\sqrt{2}}\begin{pmatrix} 0 \\ v \end{pmatrix} \ . \tag{1.4}$$

[1] The PMNS CP violating phases depend on whether the neutrinos are Majorana or Dirac fermions, which is still unknown.

After spontaneous symmetry breaking, the interaction gauge fields are the photon γ (EM), the $W^{\pm}$ and the Z^0 bosons (weak force)[2] and the gluons g (strong force). The Higgs mechanism provides fermions as well as the $W^{\pm}$ and the Z^0 bosons with masses, according to

$$M_W = \frac{g_2^2 v^2}{4} \quad \text{and} \quad M_Z^2 = (g_2^2 + g_1^2)\frac{v^2}{4} = \frac{M_W^2}{\cos^2\theta_W} \ , \tag{1.5}$$

where θ_W is the Weinberg angle defined as

$$\sin^2\theta_W = \frac{g_1^2}{g_2^2 + g_1^2} = 1 - \frac{M_W^2}{M_Z^2} \ . \tag{1.6}$$

The electric coupling e is given by $e = g_2 \sin\theta_W$.

The SM has been extremely successful, as can be illustrated by the agreement between the theoretical prediction and the experimental measurement of the anomalous magnetic moment of electron being good to more than 10 significant digits [37]. That being said, many observations suggest that there exists a more fundamental underlying theory. For example, the SM contains more than 15 unexplained parameters, does not account for the dark matter and the massive neutrinos and also does not provide an explanation for the observed electric charge quantization. Moreover, a complete description of nature should also include gravity.

Baryon Number Violation in the Standard Model

As already mentioned, the baryon number B and lepton number L are global accidental symmetries of the SM and there are no gauge invariant renormalizable (dimension $\leqslant 4$) operators which could be written down that violate them. The lowest allowed operator in the SM which violates B, is the non-renormalizable dimension-6 term

$$\mathcal{O}^{(6)}_{\not{B}} \sim \frac{QQQL}{\Lambda^2} \ , \tag{1.7}$$

where Λ is a suppression scale associated with some high energy physics, coming from a more fundamental theory. Similarly, for lepton number L, the lowest order L-violating term is the dimension-5 operator $LHLH/\Lambda$. In the above, we have suppressed the relevant indices for brevity.

[2] The photon and the weak bosons are formed from the linear combinations of B_μ and W^a_μ.

At the classical level, the Standard Model B-current $\partial_\mu j^\mu_B$ is given by

$$\partial_\mu j^\mu_B = \partial_\mu \Big[\frac{1}{3} \sum_i (\overline{Q}^i_L \gamma^\mu Q^i_L + \overline{u}^i_R \gamma^\mu u^i_R + + \overline{d}^i_R \gamma^\mu d^i_R) \Big] = 0 \ . \tag{1.8}$$

The description for the L-current $\partial_\mu j^\mu_L$ is similar. At the quantum level, however, these global symmetries are violated by the electro-weak anomalies [38, 39], resulting in

$$\partial_\mu j^\mu_B = \frac{3}{64\pi^2} \epsilon^{\alpha\beta\gamma\delta} \Big(g_2^2 W^a_{\alpha\beta} W^a_{\gamma\delta} + g_1^2 B_{\alpha\beta} B_{\gamma\delta} \Big) \ . \tag{1.9}$$

Importantly, $(B - L)$ still remains conserved, since the equivalent B and L violating contributions can be subtracted. While anomalies associated with gauge symmetries signify an inconsistency of the theory and violation of unitarity, this is not the case for anomalies associated with global symmetries[3]. Although one can attempt to gauge the baryon number B [41], gauge anomaly cancellation will require that extra charged fields are introduced to the theory, which is not desired.

For the $SU(2)_L$, a non-Abelian gauge symmetry of the SM, there exist non-perturbative field configurations ("instantons" [42]) which contribute to $\partial_\mu j^\mu_B$ and violate the baryon number. Due to their non-perturbativate nature, these effects cannot be deduced from the standard perturbative Feynman diagram calculations. Instantons originate from non-uniqueness of the vacuum ground state in non-Abelian theories and represent the tunneling rate between them. In analogy with regular quantum mechanics, these transitions, which violate baryon and lepton number separately, are exponentially suppressed and are proportional to $e^{-8\pi^2/g_2^2}$, in case of $SU(2)_L$. Because the vacua are topologically distinct (can't be morphed into one another), they can be labeled by an integer (the Chern-Simons number), which in a certain gauge is stated as

$$n_{CS} = \frac{g_2^2}{16\pi^2} \int d^3x \epsilon^{ijk} \Big(\partial_i W^a_j W^a_k + \frac{g}{3} \epsilon_{abc} W^a_i W^b_j W^c_k \Big) \ . \tag{1.10}$$

The field configurations at the top of the barriers, which need to be tunneled for a vacuum transition, are the "sphalerons" [43]. In the electro-weak case, the barrier height (sphaleron energy) is given by $E_{sp} \sim 8\pi M_W / g_2^2$. It was found by 't Hooft [44] that the lowest order baryon number violation in the SM due to instanton effects can be described by 12-fermion operator

$$\mathcal{O}_{sp} \sim \Big(\frac{1}{M_W} \Big)^{14} e^{-8\pi^2/g_2^2} \prod_i^3 \Big(\epsilon_{\alpha\beta\gamma} Q^i_{\alpha L} Q^i_{\alpha L} Q^i_{\alpha L} L^i_L \Big) \ , \tag{1.11}$$

[3] The decay rate of $\pi^0 \to \gamma\gamma$ is explained in the SM through global axial anomalies [40].

where α, β, γ represent color indices. This transition leads to $\Delta B = \Delta L = 3$. Its rate, however, is suppressed by $\Gamma_{sp} \sim |e^{-8\pi^2/g_2^2}|^2 \approx 10^{-173}$ and is thus negligible. The above calculations have assumed $T = 0$ temperature, but for finite temperature the rate of thermal fluctuations across a vacuum barrier is found to be [7, 45, 46]

$$\Gamma_{sp} = T^4 e^{-E_{sp}/T} \ . \tag{1.12}$$

Hence, at high enough temperatures (e.g. the early Universe), these processes become significant and are important for baryogenesis, as we will discuss.

In the above discussion, we have followed the review of Dine [48]. A comprehensive treatment of the subject can be found in Coleman's textbook [47].

1.1.2 In Unified Theories

Review of Grand Unified Theories

Grand Unified Theories (GUTs) are some of the most well motivated theoretical concepts beyond the SM. In GUTs, the three gauge groups of the SM are combined together. This allows to treat quarks and leptons similarly, explain charge quantization, gauge coupling unification and naturally include neutrino masses, among other things. Since leptons can interact with quarks in GUTs, within this context, baryon number violation is inevitable.

The two simplest unifications accounts are the Georgi-Glashow $SU(5)$ [49] model and the Pati-Salam (PS) $SU(4)_C \times SU(2)_L \times SU(2)_R$ [50] theory[4]. In the PS model, leptons are included as the "4^{th} color", by extending the QCD $SU(3)_C$ to $SU(4)_C$. One family of particles $[(Q_L, L_L), (Q_R, L_R)]$ transforms as $[(\mathbf{4}, \mathbf{2}, \mathbf{1}), (\overline{\mathbf{4}}, \mathbf{1}, \overline{\mathbf{2}})]$ under PS, where $Q_R = (d_R, u_R)$ and $L_R = (e_R, \nu_R)$ under $SU(2)_R$. Unlike the SM, in the PS model the left- and right-handed fields are treated on the same footing. Additionally, it includes $(B - L)$ as subgroup and contains a right handed neutrino ν_R, which is absent in the SM but desirable for neutrino mass generation. Since it is not built from a simple gauge group, strictly speaking it is not

The Georgi-Glashow $SU(5)$ is the minimal simple group which fully contains the SM[5]

[4] Since PS is not based on a simple gauge group which would include the SM, strictly speaking it is not a GUT, but rather a theory of "matter unification". This is also the reason why in PS coupling unification is not a prediction.

[5] This can be seen from the fact that both groups have rank = 4.

and we will discuss it in more detail. The theory has one universal gauge coupling, α_G, defined at the grand unification scale of the three SM couplings, M_G.

Within the $SU(5)$, quark and lepton fields reside in two irreducible representations: $\overline{\mathbf{5}} = [d_R, L_L]$ and $\mathbf{10} = [Q_R, u_R, e_R]$. This can be visualized diagrammatically as

$$\overline{\mathbf{5}} = \begin{pmatrix} d^{c,1} \\ d^{c,2} \\ d^{c,3} \\ e^- \\ -\nu_e \end{pmatrix} \quad \text{and} \quad \mathbf{10} = \begin{pmatrix} 0 & u^{c,3} & -u^{c,2} & u^1 & d^1 \\ -u^{c,3} & 0 & u^{c,1} & u^2 & d^2 \\ u^{c,2} & -u^{c,1} & 0 & u^3 & d^3 \\ -u^1 & -u^2 & -u^3 & 0 & e^c \\ -d^1 & -d^2 & -d^3 & -e^c & 0 \end{pmatrix}, \tag{1.13}$$

where the numerical superscripts represent color indices and c stands for charge conjugation[6]. The gauge sector contains 24 bosons that form a **24**-plet[7], which can be seen diagrammatically as

$$V_\mu = \begin{pmatrix} G^1_1 - \frac{2B}{\sqrt{30}} & G^1_2 & G^1_3 & \overline{X^1} & \overline{Y^1} \\ G^2_1 & G^2_2 - \frac{2B}{\sqrt{30}} & G^2_3 & \overline{X^2} & \overline{Y^2} \\ G^3_1 & G^3_2 & G^2_3 - \frac{2B}{\sqrt{30}} & \overline{X^3} & \overline{Y^3} \\ X_1 & X_2 & X_3 & \frac{W^3}{\sqrt{2}} + \frac{3B}{\sqrt{30}} & W^+ \\ Y_1 & Y_2 & Y_3 & W^- & -\frac{W^3}{\sqrt{2}} + \frac{3B}{\sqrt{30}} \end{pmatrix}, \tag{1.14}$$

where G^j_i are the 8 gluons and the W^a and the B combine to form the γ, Z^0 and $W^\pm$ bosons of the SM. The other 12 X and Y bosons are new. Identifying the lower right 2×2 quadrant of the above 5×5 matrix with $SU(2)_L$ rotations and the upper left 3×3 quadrant with the $SU(3)_C$ rotations, it can be seen that the off-diagonal X and Y gauge bosons can contribute to both and thus give lepto-quark interactions. These interactions can mediate proton decay.

The $SU(5)$ is spontaneously broken $SU(5) \to SU(3)_C \times SU(2)_L \times U(1)_Y$ to the Standard Model through the vev of the $\mathbf{24}_H$ Higgs multiplet, as depicted in Equation (1.15), which is proportional to the hypercharge generator Y with $-3Y = \text{diag}(2, 2, 2, -3, -3)$. After the breaking, the heavy X and Y gauge bosons decouple with mass M_G.

[6] Since gauge boson couplings observe helicity, left and right handed fields cannot be in the same multiplets. Hence, the right-handed fields are replaced by corresponding conjugated left-handed ones.

[7] The adjoint **24**-plet can be constructed from the $SU(5)$ fundamental **5**-plet according to $\mathbf{5} \times \overline{\mathbf{5}} = \mathbf{24} + \mathbf{1}$.

$$\langle \mathbf{24_H} \rangle \rightarrow \frac{v}{\sqrt{30}} \begin{pmatrix} 2 & 0 & 0 & 0 & 0 \\ 0 & 2 & 0 & 0 & 0 \\ 0 & 0 & 2 & 0 & 0 \\ 0 & 0 & 0 & -3 & 0 \\ 0 & 0 & 0 & 0 & -3 \end{pmatrix} . \tag{1.15}$$

The electro-weak Higgs doublet $H = (H^+, H^0)$ resides in the $\mathbf{5}_H$ of $SU(5)$, according to $\mathbf{5}_H = [T^1, T^2, T^3, H^+, H^0]$. Here, $T = (T^1, T^2, T^3)$ represents a new Higgs triplet. The fermion Yukawa couplings are formed via $\overline{\mathbf{5}}\,\mathbf{10}\,\overline{\mathbf{5}}_H$ and $\mathbf{10}\,\mathbf{10}\,\mathbf{5}_H$. Thus, the new Higgs triplet will also couple to fermions and allow them to transform into one another. This leads to rapid proton decay mediation, unless the T mass is $> 10^{11}$ GeV [51].

The charge operator $Q = T_3 + Y/2$ is a linear combination of the $SU(2)_L$ and $U(1)_Y$ generators, which can be identified with the $SU(5)$ generators. Since $SU(N)$ generators are traceless, this implies that Q eigenvalues add up to 0. Hence, this leads to one family of fermions having a quantized charge, according to

$$Q(\overline{\nu}_e) + Q(e^+) + 3Q(q) = 0 \quad \rightarrow \quad Q(q) = -\frac{1}{3}e \; . \tag{1.16}$$

Thus, charge quantization is explained in GUTs, which is not the case for the SM.

While $SU(5)$ has many virtues, there are also issues. To achieve light Higgs doublet but a heavy Higgs triplet, a tuning in the choice of vev that breaks $\mathbf{5}_H$ is required, resulting in the doublet-triplet splitting problem. Some proposed solutions include considering more complicated representations and their combinations (e.g the "hidden partner mechanism") [52], but this is not very satisfactory. Additionally, $SU(5)$ gives prediction for the Weinberg angle $\sin\theta_W$ inconsistent with experiment [53], showing that coupling unification doesn't really work out. Finally, as we will discuss later, minimal $SU(5)$ is ruled out by proton decay limits.

Going to $SO(10)$ [54] allows to unify all the matter fields in a single $SO(10)$ multiplet $\mathbf{16} = [\mathbf{10} + \overline{\mathbf{5}} + \mathbf{1}]$, where the multiples in the parenthesis transform under $SU(5)$ and $\mathbf{1}$ represents a right-handed neutrino singlet. Because the group rank of $SO(10)$ is 5, its breaking proceeds to SM in two steps. The breaking patterns can be visualized as

$$SO(10) \rightarrow \left\{ \begin{array}{c} SU(4)_C \times SU(2)_L \times SU(2)_R \\ SU(3)_C \times SU(2)_L \times SU(2)_R \times U(1)_{B-L} \\ SU(5) \times U(1)_X \end{array} \right\} \rightarrow SU(3)_C \times SU(2)_L \times U(1)_Y \ ,$$

among which we can identify the Pati-Salam and the $SU(5)$ sub-groups. If Q_{EM} is part of the extra $U(1)_X$, one obtains a "flipped" $SU(5)$ model [55, 56] instead of the usual $SU(5)$. Typically, the $SO(10)$ breaking is done by rather large Higgs multiplets, residing in $\mathbf{10}_H, \mathbf{45}_H, \mathbf{126}_H, \mathbf{54}_H$ representations. The doublet-triplet problem of $SU(5)$ also persists in $SO(10)$. The Yukawa couplings originate from $\mathbf{10}_H\,\mathbf{16}\,\mathbf{16}$ and the neutrino masses are typically implemented via "see-saw" mechanism [57, 58, 59, 60, 61], since it requires a right handed neutrino with mass around the GUT scale. To successfully account for the observed fermion masses and mixing one can impose additional "flavor symmetries"[8].

Supersymmetry (SUSY) can be added to GUTs, allowing to make gauge coupling unification precise[9], as depicted in Figure 1.1. There are many reasons why SUSY is appealing and we point the reader to a comprehensive review of Ref. [65] for details. It is the maximal possible extension of the Poincare symmetry (Haag-Lopuszanski-Sohnius theorem [66]) for 4-D QFTs[10] and allows to solve the gauge hierarchy problem of the SM (why is there such a discrepancy between the electroweak and the Planck scales), more so, it is thought to be a consistency requirement for string theory and is motivated phenomenologically. With SUSY, the fermions and the bosons are related. Hence, in the minimal supersymmetric SM with global supersymmetry (the MSSM) each field has an accompanying superpartner. The resolution of hierarchy problem requires superpartners to be around the TeV scale, which so far have not been observed at the Large Hadron Collider (LHC) [67, 68]. At the cost of abandoning the hierarchy problem, one could raise the scale of SUSY breaking / superpartner masses and thus alleviate the experimental constraints. When combined with GUTs, SUSY GUTs can ease some of difficulties encountered within non-SUSY GUTs, such as precise coupling unification. SUSY GUTs can have significantly different predictions for nucleon decay than the non-SUSY GUTs, as we will discuss below.

To conclude the overview of unified theories, let us briefly mention ventures beyond

[8] For an overview of discrete flavor symmetries and how they can be applied to GUTs see Ref. [62].

[9] If one considers complicated enough breaking of $SO(10)$ with appropriate intermediate scales, coupling unification consistent with experiment can be achieved without SUSY [63]. Such models, however, are overly contrived.

[10] These combined Super-Poincare transformations are the reason why gauged (local) SUSY, the supergravity, automatically incorporates General Relativity.

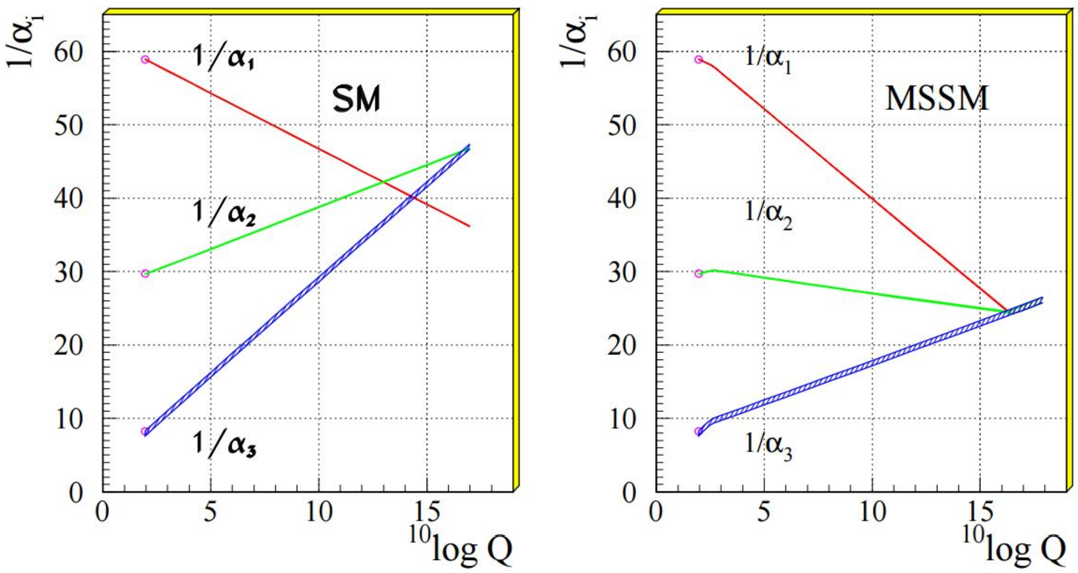

Figure 1.1: Evolution of the inverse of the three coupling constants in the SM [left] and in the MSSM [right]. Only in the latter case unification is obtained. The SUSY particles are assumed to contribute only above the effective SUSY scale M_{SUSY} of ∼TeV. From Ref. [64].

4-D GUTs and SUSY. String theory (ST) is the only known consistent theory of quantum gravity. While there is a strong model building effort (e.g. [69, 70, 71, 72]) to get concrete phenomenological predictions from ST, due to a large number of possibilities how the 10-D theory can be "compactified" to the 4-D theory, this path is difficult. However, generic predictions (e.g. abundance of axions) do exist [73] and string-motivated constructions can be both manageable and predictive. For example, some of the recent work has been focused on GUTs in higher dimensions (5-D and 6-D). Such constructions allow to alter proton decay rate predictions [74] and explain various scale hierarchies, by considering a specific arrangement of fields in the higher dimensional space. This also allows to potentially address the doublet-triplet splitting issue, outlined earlier. With this approach, however, one substitutes the choice of a selecting a specific Higgs vev in 4-D with the choice of boundary conditions in extra dimensions [75]. Similarly, motivated by $E^8 \times E^8$ symmetry of ST and the embedding $E_8 \supset E_6 \supset SO(10)$, one can consider even larger GUT groups with more complicated breaking patterns than those of $SO(10)$. However, the number of extra fields and parameters introduced is substantial and the models become overly contrived with not very general predictions. A comprehensive review of unified theories and supersymmetry can be found in Mohapatra's textbook [8].

Baryon Number Violation in Unified Theories

We will now discuss several of the most popular nucleon decay signatures. In the context of $SU(5)$, nucleon decay is mediated by the X and Y gauge boson exchange. This gives effective dim-6 baryon number-violating operators. Figure 1.2 displays diagrams for $p \to e^+\pi^0$ mediation, which is typically the dominant decay channel in non-SUSY GUTs. The

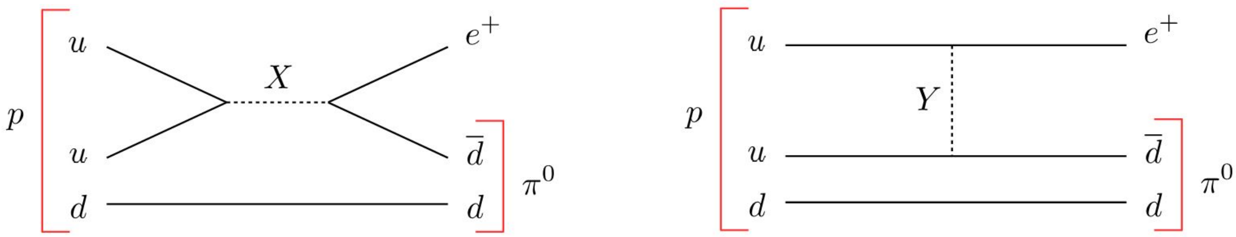

Figure 1.2: Nucleon decay $p \to e^+\pi^0$ from X, Y gauge boson exchange, resulting in effective dim-6 contribution. This is typically the dominant nucleon decay channel within non-SUSY GUTs.

lifetime of the proton is then given by

$$\tau_{p\to e^+\pi^0} \quad \sim \quad \frac{M_G^4}{m_p^5} \,, \tag{1.17}$$

where m_p is the mass of the proton and the X and Y masses have been taken as M_G. Minimal Georgi-Glashow $SU(5)$ [49] predicts the lifetime of $p \to e^+\pi^0$ to be around $4.5 \times 10^{29\pm1.7}$ years, which has been decisively ruled out by experimental limits of $\tau_{p\to e^+\pi^0} > 10^{33}$ years [77, 78, 79, 80].

Once SUSY is introduced, the unification scaled is pushed up from 10^{15} GeV to more than 10^{16} GeV. This leads to significant suppression of the dim-6 $\not{B}$ terms [81, 82, 83], which are proportional to $1/M_G^2$, resulting in an increased proton lifetime of $\tau > 10^{34-38}$ years. On the other hand, SUSY also introduces new dim-4 and dim-5 operators that could also mediate nucleon decay. The most dangerous are the dim-4 baryon number-violating $\overline{UDD}$ and the lepton number-violating $QL\overline{D}, LL\overline{E}$ terms[11]. If both of these are allowed, they lead to very fast proton decay, with lifetime proportional to the squark mass $\tau \sim 1/M_{SUSY}^2$. By itself, this can be taken as supersymmetry predicting baryon number violation even without any Grand Unification scheme. In order to suppress nucleon decay coming from these operators, one can forbid either $\not{L}$ or $\not{B}$ terms independently (leading to R-parity

[11] Here, $\overline{U}, \overline{D}, L, Q$ and $\overline{E}$ denote superfields and contain both the original fermion and a boson superpartner. Recall that fermions contribute with a mass dimension of 3/2 and bosons with 1.

violation [84]), or forbid both $\not{L}$ and $\not{B}$ terms simultaneously (e.g. with R-parity[12] [85] or $\mathbb{Z}_4^R$ [86]). If only the L-violating or the B-violating terms are forbidden independently, however, the resulting scenario will not be compatible with $SU(5)$ or $SO(10)$, where these terms are allowed or forbidden simultaneously. Although, in this case, Pati-Salam compatibility is still an option [84].

Having forbidden SUSY dim-4 operators, the dominant contribution will typically come from the dim-5 terms $QQQL$ and $\overline{UUDE}$. Within supersymmetric GUTs, these terms arise from the Yukawa couplings of the triplet T Higgs-superpartner (Higgsino) and they are proportional to $1/M_T$. As the final state sfermion superpartners are not observed, they need to be converted to the regular SM fermions ("dressed") by a gaugino (Wino or Higgsino) loop. Usually, these considerations lead to $p \to \overline{\nu}K^+$ being the dominant nucleon decay mode in SUSY GUTs. In Figure 1.3 we depict typical diagrams originating from dim-4 and dim-5 baryon number-violating operators. The lifetime of the proton coming from the effective

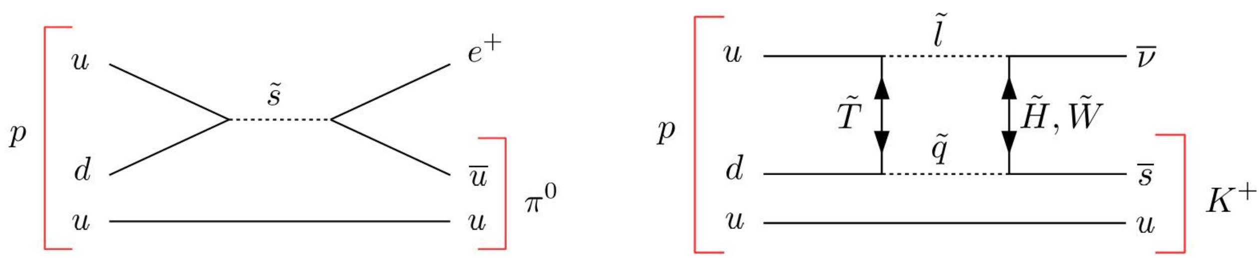

Figure 1.3: Typical nucleon decay diagrams in SUSY GUTs. On the left is $p \to e^+\pi^0$, coming from dim-4 terms and a squark exchange. On the right is $p \to \overline{\nu}K^+$, coming from dim-5 triplet Higgsino exchange with the superpartners dressed by a Wino or Higgsino loop.

dim-5 terms is then given by

$$\tau_{p\to\overline{\nu}K^+} \quad \sim \quad \frac{M_G^2 M_{SUSY}^2}{m_p^5} \ , \tag{1.18}$$

where we have substituted M_G for M_T (assuming the triplet Higgsino is at the GUT scale). In a full nucleon decay calculation (e.g. see Ref. [87]) one needs to also determine the loop factor and the matrix element. The matrix element represents transition between vacuum state and creation of the nucleon $\langle 0|qqq|N\rangle$. It can found via Chiral Lagrangian [88] or lattice calculations [89]. The final amplitude has a strong dependence on the fermion masses and mixing and the details of SUSY breaking / arrangement of the SUSY spectrum. The minimal

[12] Matter parity is a discrete $\mathbb{Z}_2$ symmetry under which the matter superfields $Q, \overline{U}, \overline{D}, L$ and $\overline{D}$ are odd and the Higgs superfields H_u and H_d are even. This forbids the unwanted dim-4 (R-parity violating) $\not{B}$ and $\not{L}$ terms. A combination of matter parity with a discrete subgroup of the Lorentz group gives R-parity, under which all SM fields are even and superpartners odd.

SUSY $SU(5)$, with SUSY taken at the TeV scale as motivated by the hierarchy problem, is also ruled out [90] by experimental constraints on $\tau_{p\to\overline{\nu}K^+} > 10^{33}$ years [91].

Thus far we have discussed nucleon decay in the simplest scenarios of minimal SUSY and non-SUSY $SU(5)$. Going to larger groups such as $SO(10)$ adds more variation in model constructions and thus predictions. In the case of SUSY GUTs, there is a large theoretical uncertainty coming from SUSY breaking sector and the resulting superpartner spectrum. Additionally, because in GUTs many model sectors are related, there are typically multiple nucleon decay channels which are predicted with various branching ratios. These predictions have strong dependency on such things as the fermion mass and mixing spectrum. Overall, majority of models predict that the dominant channels will have $\tau_p < 10^{36}$ years [92].

Aside from regular single nucleon decay, it is also worthwhile to mention other baryon number violating processes. One such process is neutron - anti-neutron oscillation $n-\overline{n}$ (see Ref. [93] for review). It can be described by an effective 6-fermion operator

$$\mathcal{O}_{n-\overline{n}} \quad \sim \quad \frac{1}{\Lambda^5}\Big(Q_LQ_LQ_LQ_Ld_Rd_R + u_Rd_Rd_Ru_Rd_Rd_R\Big) \;, \tag{1.19}$$

where Λ is the suppression scale. The $n-\overline{n}$ lifetime can be calculated using the usual quantum mechanical 2-state Hamiltonian approach. Taking the current experimental limit of $\tau_{n-\overline{n}} > 0.86 \times 10^8$ s. [94] yields Λ of the order of ~ 100 TeV [93]. If SUSY is introduced, superpartner appearance in the above operator lowers its dimension, which in turn allows to raise the suppression scale. Even with SUSY, unlike regular proton decay, $n-\overline{n}$ allows to test scales far below the GUT scale. Inside matter, the neutron and anti-neutron potentials are different and the $n-\overline{n}$ lifetime in matter is related to the lifetime in vacuum according to

$$\tau_{n-\overline{n}}^{Nuc.} = R(\tau_{n-\overline{n}})^2 \;, \tag{1.20}$$

where $R \sim 0.3 \times 10^{24}\text{s}^{-1}$ is a nuclear suppression factor. This gives $\tau_{n-\overline{n}}^{Nuc.} \sim 10^{32}$ years, comparable to the regular proton decay limits. An additional feature that separates this process from the typical $p \to e^+\pi^0$ and $p \to \overline{\nu}K^+$ channels, is that neutron oscillation is a $|\Delta(B-L)| = 2$ transition. It is possible to construct models [95] where this process arises within the context of GUTs and is connected to baryogenesis and Majorana neutrino masses, which have $\Delta L = 2$ and thus also break $(B-L)$ symmetry.

Another example of how baryon number violation can occur is through monopoles [96] catalyzing nucleon decay. When a breaking of a simple GUT gauge group leads to a residual $U(1)$ (i.e. $G \to H \times U(1)$), magnetic monopoles which carry a $U(1)$ charge will appear

[97, 98]. With a mass of the order M_G, they are expected to be abundant in the early Universe. Since central core of a GUT monopole contains heavy gauge bosons, they can violate baryon number. In fact, monopoles can catalyze proton decay through the Callan-Rubakov effect [99, 100], resulting in

$$M + p \to M + e^+ + mesons \ . \tag{1.21}$$

The striking feature of this process is that the amplitude is not suppressed by $1/M_G$. The problem lies in estimating the exact expected proton decay rate from this reaction. There are other objects, such as supersymmetric Q-balls [101], which can be produced in the early Universe and could catalyze nucleon decay [102].

Finally, effects of quantum gravity can also lead to baryon number violation. As an example, consider proton decay catalyzed by virtual black holes. As already mentioned, it is thought that quantum gravity generally violates global symmetries (e.g. baryon number) [9]. Consider the process [76] where 2 quarks of a proton fall into a small black hole of mass $m_{BH} \sim M_{Pl}$ and that baryon number is violated (e.g. $q + q \to \overline{q} + l$). Then, one can roughly estimate the proton's lifetime as

$$\tau_p \sim 10^{36} \times \left(\frac{M_{QG}}{10^{16}\mathrm{GeV}}\right)^4 \mathrm{yrs} \ , \tag{1.22}$$

which for $M_{QG} = M_{PL}$ gives $\tau_p \sim 10^{45}$ yrs.

For an exhaustive review of possible baryon number-violating mechanisms and their signatures see Ref. [76].

1.1.3 In Cosmology

The Standard Model of Cosmology is Λ-CDM. It is described by the Big Bang cosmology, a cosmological constant Λ, associated with dark energy, and abundance of cold dark matter (CDM). It is well supported by observation of light element abundance from Big Bang nucleosynthesis (BBN), Hubble expansion and cosmic microwave background (CMB). Fitting the astronomical data to parameters of Λ-CDM [103] gives a description of the Universe that is composed of 68.5% dark energy, 26.5% dark matter and 4.9% of ordinary matter (baryons). There is an inherent matter - anti-matter asymmetry observed in the Universe. From cosmic microwave background radiation (CMB), the measured ratio of baryon

n_b to photon n_γ density is found to be [104]

$$\eta = \frac{n_b}{n_\gamma} = (6.19 \pm 0.14) \times 10^{-10} \ . \tag{1.23}$$

The lack of anti-baryon excess is reaffirmed by the astrophysical anti-proton flux [105], which is found to be consistent with secondary cosmic ray production.

To explain the cosmologically observed baryon asymmetry, naively, one could expect that there has always been a B asymmetry (i.e. $B > 0$) starting with the Big Bang. However, such an initial asymmetry would be diluted to a negligible quantity by inflation [106, 107, 108], a period of rapid expansion of the Universe. While multiple models of inflation exist (see Ref. [109] for review), the concept itself provides a simple resolution to several key problems in cosmology and thus abandoning it would be undesirable. Namely, inflation addresses the issues of horizon (why the Universe is homogeneous and isotropic), flatness (why spatial curvature of Universe is small) and the exotic-relic abundance (why such exotics as GUT monopoles, produced during the early Universe, have not been observed). Another possibility is that there is no global B asymmetry, and we are just located in a special separated region of the Universe filled with matter and not anti-matter, but in other regions it is the opposite. However, not only is this a non-minimal assumption, there is evidence that if large regions of anti-matter exist, they are on cosmic distance scales away [110]. The final option, which is the one that we shall focus on, is that initially $B = 0$ and then baryon asymmetry was generated via some mechanism of baryogenesis.

For a successful mechanism of baryogenesis, three conditions, as outlined by Sakharov [5], must be satisfied:

1. **B-number violation processes exist:** if all interactions conserve B, then B is globally conserved.

2. **C and CP violation exist:** C and CP symmetries interchange particles $\leftrightarrow$ anti-particles and particles $\leftrightarrow$ anti-particles followed by a parity flip, respectively. The requirement of C and CP violation ensures that B-violating processes are not cancelled out by B-generating processes.

3. **Period with B-violating processes out of equilibrium exists:** CPT theorem assures that masses of particles and anti-particles are equal and hence their thermal equilibrium densities are also same. Thus, even if $\not{B}$ processes which violate C and CP exist, they must happen during thermal non-equilibrium to ensure that the thermal

average of B is non-zero.

While a large number of specific baryogenesis mechanisms have been proposed, we outline below some of the most popular categories and their respective problems, following the subject review by Dine and Kusenko [111]:

- **Electroweak Baryogenesis**: SM by itself satisfies all of the Sakharov's conditions for baryogenesis [7]. While B is a global symmetry in SM, as discussed in Section 1.1.1, $\not{B}$ is induced by sphalerons and at high enough temperatures the rates for these processes can be significant. The CP violation already occurs in quark sector and out of equilibrium condition can happen during the electroweak phase transition. However, if one considers SM alone, CP violation in the quark sector is too small and some difficulties arise with getting the appropriate strength of the phase transition.

- **Planck-scale (gravity-induced) Baryogenesis:** as discussed in Section 1.1.2, global symmetries are violated by quantum gravity effects and one would expect that B-violating processes are present. These effects are suppressed by the Planck scale M_{Pl} and can be significant in the early Universe. However, not only is it difficult to calculate things precisely during that epoch, any early generated $\not{B}$ will be diluted by inflation later.

- **GUT-scale Baryogenesis:** as quarks and leptons transform in common GUT multiplets, baryon number-violating processes, like proton decay, naturally occur within GUTs. It is typically assumed that above the GUT scale there is thermal equilibrium. At a scale below the mass of the new GUT gauge bosons, dynamics of their interactions do not produce them sufficiently fast to maintain the equilibrium. Additionally, their decays have new CP violating couplings. However, inflation again can dilute any generated B number at GUT scale unless reheating temperature is very high, which is problematic for cosmology.

- **Leptogenesis** [112]**:** as already mentioned in Section 1.1.1, the lowest order non-renormalizable operator for the neutrino masses in the SM is a dimenstion-5 L-violating term $LHLH/\Lambda$. This results in Majorana neutrinos. Invoking the see-saw mechanism to explain their mass scale requires introduction of the Dirac and the Majorana mass terms for the additional heavy right-handed neutrinos N_i. In the early Universe, N_i can decay to neutrinos and produce their overabundance, assuming that the new N_i CP violating phases are appropriate. This L-violation can then be transformed by sphalerons into B-violation, since they conserve $B - L$. However, this mechanism is difficult to test.

- **Coherent Motion of Scalar Fields (Affleck-Dine mechanism [113]):** assuming supersymmetry, the scalar superpartners carry B and L. Their potentials typically have flat directions which allow to easily offset the field from the minimum. A large classical value of such field ("coherent field") can carry a large amount of B and later decay to quarks, producing observed B-asymmetry. This scenario is naturally realized primarily within the context of supersymmetric theories and is not very viable otherwise.

Finally, it is important to stress that baryon number-violating processes like proton decay will affect the ultimate fate of the Universe [10]. As quantum gravity effects can catalyze proton decay, the result will affect cosmology on the larger cosmological time scales, during the epoch of $t \geqslant 10^{15-35}$ years. The reactions like $p \to e^+\pi^0$ will power stars (e.g. neutron stars, white dwarfs) through the processes like

$$p + e^- \to \gamma + \gamma + \gamma + \gamma \ , \tag{1.24}$$

with one pair of γs coming from $e^+ + e^-$ annihilation and another from $\pi^0 \to \gamma + \gamma$. The precise determination of the cosmological era when such processes become significant depends on the details of the relevant nucleon decay lifetime calculation.

1.2 Experimental Searches for Nucleon Decay

The experimental considerations of nucleon decay began with Goldhaber [13] in 1954 [114], searching for fission products of thorium (Th^{232}) and placing a limit on proton's lifetime of $\tau_p > 10^{20}$ years. Here, one looks for isotope production due to nucleon decay. This is a very general search technique and does not assume any particular decay mode. At the same time, direct searches for proton decay were conducted by Cowan, Goldhaber and Reines [115]. These were done using scintillator as a source and the detector. Such searches are less general and rely on the decay products coming from specific channels. Many searches have followed, eventually leading up to large underground experiments based

[13] Even before the actual experiments in 1950s, Goldhaber proposed a heuristic argument that proton lifetime should be $> 10^{16}$ years, based on $\sim 10^{29}$ protons in human body and a human lifetime span of $\sim 50 - 100$ years.

on iron calorimeters and water Cherenkov detectors. The iron calorimeters offer great position and energy resolution, but they are expensive and consequently suffer from limited fiducial volume, which for nucleon decay is vital and that is made up in water Cherenkov detectors.

Year	Reference	Lifetime Limit	Technique
1954	Goldhaber [114]	2×10^{20} yrs.	FI (Th^{232})
1954	Reines, Cowan and Goldhaber [115]	1×10^{22} yrs.	SC
1958	Reines, Cowan and Kruse [116]	4×10^{23} yrs.	SC
1958	Flerov *et. al.* [117]	2×10^{23} yrs.	FI (Th^{232})
1960	Backenstoss *et. al.* [118]	3×10^{26} yrs.	SC
1962	Giamati and Reines [119]	7×10^{27} yrs.	SC
1965	Kropp and Reines [120]	4×10^{28} yrs.	SC
1967	Gurr *et. al.* [121]	8×10^{29} yrs.	SC
1974	Bergamasco and Picchi [122]	1×10^{29} yrs.	SC
1974	Reines and Crouch [123]	2×10^{30} yrs.	SC
1977	Steinberg and Evans [124]	2×10^{25} yrs.	FI (Te^{130})
1977	Fireman [125]	2×10^{26} yrs.	FI (K^{39})
1981	Cherry *et. al.* (Homestake) [126]	3×10^{30} yrs.	WC
1982	Battistoni *et. al.* (NUSEX) [127]	2×10^{31} yrs.	FGC (Fe^{26})
1986	Krishnaswamy *et. al.* (KGF) [128]	4×10^{31} yrs.	FGC (Fe^{26})
1987	Bartelt *et. al.* (Soudan) [129]	2×10^{30} yrs.	FGC (Fe^{26})
1989	Hirata *et. al.* (Kamiokande) [79]	3×10^{32} yrs.	WC
1991	Berger *et. al.* (Frejus) [130]	2×10^{32} yrs.	FGC (Fe^{26})
1999	McGrew *et. al.* (IMB) [131]	8×10^{32} yrs.	WC
2012	Nishino *et. al.* (Super-Kamiokande) [132]	8×10^{33} yrs.	WC

Table 1.2: Proton decay searches. We have denoted their operating principle: search for fission fragments from radioactive ore (FI), liquid scintillator (SC), water Cherenkov (WC) and fine-grained calorimeters (FGC).

Many nucleon decay channels have been searched for, including $n - \overline{n}$ and dinucleon np, nn, pp decays. However, no convincing evidence for nucleon decay has been obtained throughout the experiments. We have summarized in Table 1.2 their results, including the operating technique and the best obtained nucleon decay limit. Stringent experimental constraints also exist on other processes which could lead to baryon number violation, such as proton decay-catalysis from the Q-balls [133] and the GUT monopoles [134].

1.3 Overview of the Analysis

As already discussed, the simplest unification scenarios based on minimal non-SUSY and (TeV-)SUSY $SU(5)$ have been strongly constrained by the experimental lifetime limits on $p \to e^+\pi^0$ [77, 78, 79, 80] and $p \to \bar{\nu}K^+$ [91], respectively. Additionally, no signs of (TeV-)SUSY have been observed at the Large Hadron Collider (LHC) [67, 68]. Hence, there is reinvigorated interest in alternative possible signatures.

After $SU(5)$, the next logical GUT to study is $SO(10)$, which is very well theoretically motivated and arguably more appealing than $SU(5)$. However, due to a large number of possible constructions, there are not very many concrete universal predictions from $SO(10)$, as we have discussed in Section 1.1.2. In the schemes of Ref. [135, 136], trilepton decay channels $p \to e^+\nu\nu$ and $p \to \mu^+\nu\nu$ could become significant within the Pati-Salam $SU(4)_C \times SU(2)_L \times SU(2)_R$ [137] model coming from spontaneous breaking of $SO(10)$. Signatures of this breaking pattern have not been very well experimentally explored. Additionally, these channels present unusual decay patterns. We describe in more detail a possible setup and how these channels can arise with significant branching ratios in Appendix A. Assuming trilepton mediation, these scenarios predict proton lifetime of around 10^{30-33} years. On the other hand, the old experimental limits are 1.7×10^{31} years from IMB [131] and 2.1×10^{31} years from Frejus [138], for $p \to e^+\nu\nu$ and $p \to \mu^+\nu\nu$, respectively. Hence, searching for these modes in the current state of the art-experiments would allow to restrict a significant portion of the allowed parameter space for such models. Additionally, observation of these channels, coupled with non-observation of $p \to e^+\pi^0$, may allow to differentiate between PS and its $SO(10)$ embedding [135]. Depending on the combination of neutrinos/anti-neutrinos that are present in the final state, the channels also have $|\Delta(B-L)| = 2$, unusual for single nucleon decay. In Ref. [139] it has been suggested that observation of trilepton modes can have favorable implications for baryogenesis. Interestingly, the proton decay through these channels was offered as a possible explanation [140, 141] of the observed atmospheric neutrino flavor "anomaly" [142, 143], prior to the discovery of the neutrino oscillations [17].

In this work, we will describe a search for the trilepton decay channels using the best available instrument, the largest underground water Cherenkov detector, Super-K [22]. Because neutrinos are invisible within Super-K, one cannot reconstruct the invariant mass and momentum of the parent nucleon from the final state particles. Hence, the only signature of the above two modes is a charged lepton, which produces a showering or a non-showering single Cherenkov ring within the detector. Since these signatures are also common for a class of other channels, we will take this as an opportunity to do a broad search for multiple decay modes, which is important due to a large theoretical uncertainty in predictions, as discussed in Section 1.1.2. In addition to the trilepton channels, we will consider two general 2-body decays $p \to e^+X$ and $p \to \mu^+X$, where X is taken to be single unknown and invisible particle that is assumed to be massless. Note, that our searches for $p \to e^+X$ and $p \to \mu^+X$ are distinct from the model-dependent inclusive analyses of Ref. [126, 144] that are listed in the PDG [37] with the same name[14]. We will also search for $n \to \nu\gamma$, with γ producing the same signature as the $e^\pm$ in the detector. Though this radiative process is suppressed, it has a clean signal and has been considered in the context of SU(5) [145], with some models [76] predicting a lifetime of $10^{38\pm1}$ years.

In addition to the single nucleon decay channels, we will also look for dinucleon decay modes which also produce the above signatures. While single nucleon $\Delta B = 1$ processes have been in general well studied, dinucleon $\Delta B = 2$ channels also pose great interest. These higher-dimensional processes can become significant in models that suppress proton decay and could be connected to baryogenesis [146]. The disappearance $\Delta B = 2$ reactions, with invisible final state particles, have already been studied and no signal excess was observed [138, 147, 148]. We will thus focus on the dinucleon channels $np \to e^+\nu$, $np \to \mu^+\nu$ and $np \to \tau^+\nu$, which violate baryon number by two units and violate lepton number by either two or zero units, depending on neutrino/anti-neutrino final state. They can become significant in models with an extended Higgs sector [146, 149], which could be also considered in the context of GUTs [150]. It is worthwhile to note, that τ final states cannot occur in single nucleon decay due to its large mass of $m_\tau \approx 1.777$ GeV. On the other hand, it can appear within dinucleon decay, as has been stressed in Ref. [151]. The process $np \to \tau^+\nu$ has in fact never been experimentally studied before and in addition to the electron and muon channel searches we present the first search in the τ channel.

Since the signal signatures for all of the above channels are single Cherenkov rings, the signal lies on top of a large amount of background coming from atmospheric neutrinos, as will be discussed later. Previous analyses in older experiments performed the search by using a counting method within some selected signal region. On the other hand, for all our searches, we will be using a spectral χ^2 fit[15] [154]. This will allow us to discriminate between the signal and the background distribution shapes and thus significantly improve the sensitivity of the analyses. This is particularly relevant for trilepton and $np \to \tau^+\nu$ channels, since their

[14] Inclusive analyses were done by assuming specific branching ratios of $SU(5)$ and then adding up all of the contributions from the various decay channels, such as $p \to e^+\pi^0$, weighted by the branching ratios.

[15] The fit is also used in the Super-Kamiokande neutrino oscillation [152] and dark matter analyses [153].

signal comes from 3-body decays and is thus spread out.

The main analyses presented within this Thesis accompany and describe in more detail the published results of Ref. [155] and Ref. [156]. The 3-body spectrum approximation method discussed in Appendix B follows the published results of Ref. [157].

Chapter 2

The Super-Kamiokande Experiment

The Super-Kamiokande experiment operates by detecting the Cherenkov radiation photons produced within the water-based detector. The emitted light produces ring-like patterns on the detector walls. The timing, amount of charge in the photomultiplier tubes (PMTs) of the detector and the shape of these patterns gives information about the kinds of particles that appear within the detector. Below, we describe the physics mechanism behind Cherenkov radiation. Then, we provide an overview of the experimental apparatus. A comprehensive description of the detector and its calibration can be found in Ref. [22] and Ref. [158], respectively.

2.1 Cherenkov Radiation

Cherenkov radiation [159] occurs when a charged particle traverses a dielectric medium with a speed (v_p) greater than the phase velocity of light (c/n) in the same medium, given by

$$c > v_p > \frac{c}{n} \ . \tag{2.1}$$

Here, c is the velocity of light in vacuum and n is the refraction index of the medium ($n = 1.33$ for water at 20° and $\lambda = 580$ nm). The electrically polarized medium then de-excites and coherently radiates back, resulting in a cone-like pattern of emitted light with respect to the particle's trajectory. A schematic diagram for this effect is displayed in Figure 2.1. The

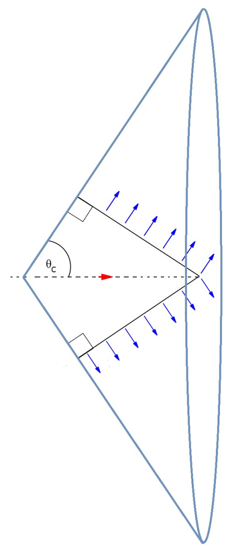

Figure 2.1: Schematic diagram for the emitted cone-like pattern of light resulting from Cherenkov radiation. The direction of the charged particle (red arrow) and the emitted light (blue arrows) is shown.

cone's opening angle θ_C is given by

$$\cos\theta_C = \frac{1}{n\beta} = \frac{1}{n}\sqrt{1+\frac{m^2}{p^2}}\ , \tag{2.2}$$

where $\beta = v/c$ and m, p are the mass and momentum of the charged particle, respectively. From Equation (2.2), one can deduce the momentum threshold ($p_{thr.}$) to emit the Cherenkov light (at $\theta_C = 0$) in a medium of refraction index n as

$$p_{thr.} = \frac{m}{\sqrt{n^2-1}}\ . \tag{2.3}$$

Hence, in water, the Cherenkov radiation threshold of the electrons ($e^{\pm}$), muons ($\mu^{\pm}$), charged pions ($\pi^{\pm}$) and the kaons ($K^{\pm}$) is 0.58 MeV/c, 121 MeV/c, 159 MeV/c and 563 MeV/c, respectively. For an ultra-relativistic particle (with $\beta \rightarrow 1$) traversing water, the Cherenkov angle for the generated cone of light will approach $\theta \sim 42^{\circ}$. The emitted spectra has a wavelength dependence and is described by

$$\frac{d^2N}{dxd\lambda} = 2\pi\alpha\Big(1-\frac{1}{(n\beta)^2}\Big)\frac{1}{\lambda^2}\ , \tag{2.4}$$

where dN, α, $d\lambda$ and dx correspond to the number of emitted photons, fine structure constant, differential unit of the wavelength and the distance, respectively.

2.2 Detector Description

2.2.1 Design

The Super-Kamiokande experiment is located in a zinc mine at Kamioka, Gifu Prefecture, Japan. Being beneath a ~ 1000 m rock overburden (2700 m water equivalent), allows for strong shielding of the cosmic ray muon background, reducing its flux to 6×10^{-8} cm^{-2}s^{-1}sr^{-1} (five orders of magnitude compared to the Earth's surface). A schematic overview of the experiment can be found in Figure 2.2. The Super-Kamiokande detector consists of a cylin-

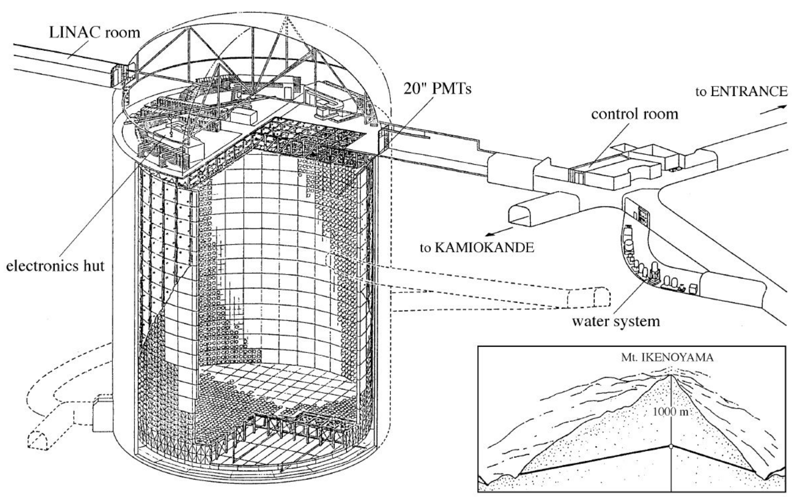

Figure 2.2: Overview of the Super-Kamiokande experiment. From Ref. [22].

drical stainless steel tank (39.3 m in diameter and 41.4 m in height). It is separated into three regions, the inner detector (ID), dead space and the outer detector (OD). The inner detector is comprised of 32 kilotons of water and a size of 36.2 m in height and 33.8 m in diameter. The ID walls are covered with 20-inch (in diameter) 11,146 uniformly distributed and inward-facing PMTs, giving detector a 40% photo-coverage. The dead space is a 0.55 m region between the ID and the OD and contains support structures. The OD fully encloses ID with ~ 2 m thickness of water and contains 1,885 outward-facing 8-inch (in diameter) PMTs. The inner detector walls are lined with an opaque covering to improve signal discrimination. For the OD, a reflective material is used to improve sensitivity, allowing to better reject noise/background. Additionally, Helmholtz coils are used to reduce the Earth's geomagnetic field effect, which can disturb the PMT electronics, from $450 \rightarrow 50$ mG. The purpose of the outer detector is to act as an active veto against background as well as a shield from radiation coming from the surrounding rocks.

2.2.2 Photomultiplier Tubes

The custom design of the SK PMTs maximizes their photo-sensitivity. The quantum efficiency, overlaid with the wave-length dependent spectrum of the Cherenkov radiation in water, as well as the single photo-electron response of the ID PMTs can be found in Figure 2.3. The custom PMTs have their quantum efficiency maximized around ~ 400 nm,

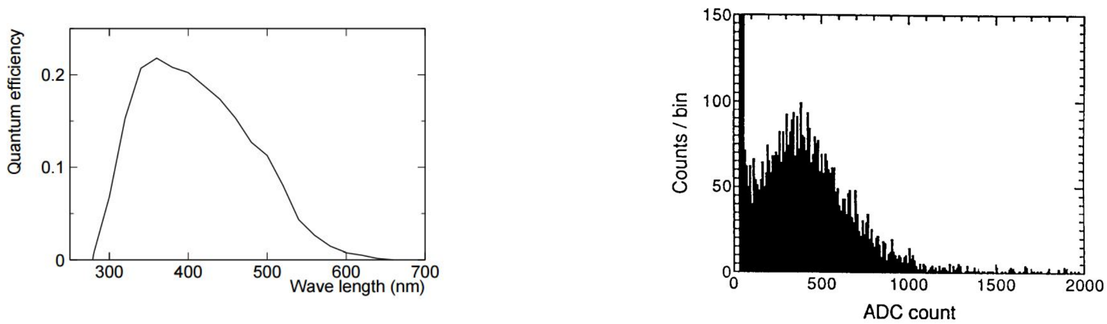

Figure 2.3: [left] Inner detector PMT quantum efficiency as a function of wavelength. [right] Single photo-electron PMT analog-to-digital converter (ADC) response, with the peak around zero being dark noise. From Ref. [22].

which also corresponds to the peak light yield for the Cherenkov radiation spectrum in water described by Equation (2.4).

2.2.3 Water and Air Purification Systems

The SK detector water comes from abundant amounts of spring water in the mine. It is passed through the water filtration system, depicted on Figure 2.4, which improves the purity and thus ensures a high attenuation length of around 100 m at $\lambda = 420$ nm, essential for high sensitivity of the physics analyses. Additionally, the filtration system removes radioactive radon (Rn), which serves as a background for solar neutrino oscillation analysis ($\sim$ MeV energy range). The detector water is continuously circulated through the filtration system at a rate of ~ 35 ton/hour. The purification system allows to reduce the number of particles larger than 0.2 μm to about 6 particles/cm^3. The resistivity of the water is also improved from 11 M$\Omega \cdot$ cm $\rightarrow$ 18.2 M$\Omega \cdot$ cm, approaching the chemical limit.

Additionally, to reduce radon concentration in the experimental area, air is continuously pumped from outside the mine. This allows to keep the radon concentration around $20 - 30$ mBq/m^3 inside the top of the SK tank and $\sim$ 100 Bq/m^3 at the SK dome outside the

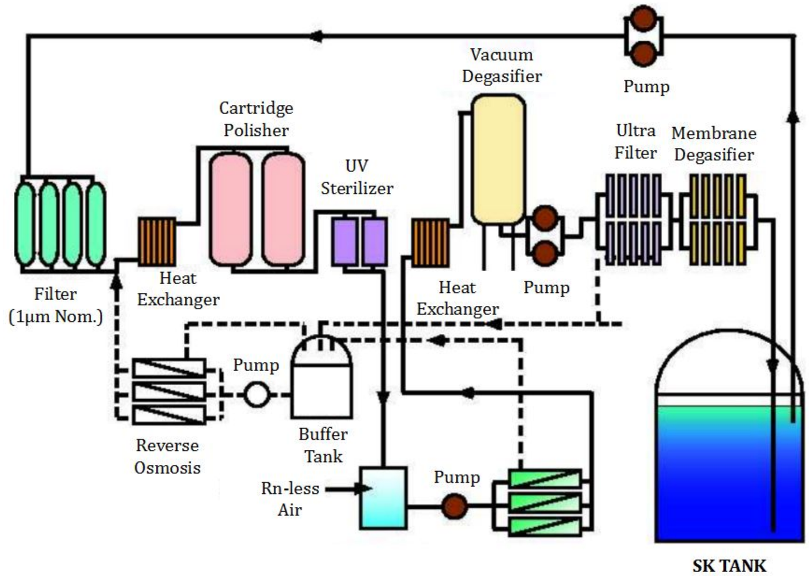

Figure 2.4: Overview of the Super-Kamiokande water purification system. From Ref. [22].

tank (compared to $100 - 3000$ Bq/m^3 in the mine). To ensure that the purified water in the SK detector stays radon free, a separate air-filtration system pumps radon-purified air (Rn concentration 3 mBq/m^3) right above the water within the detector. The air-filtration system is depicted on Figure 2.5.

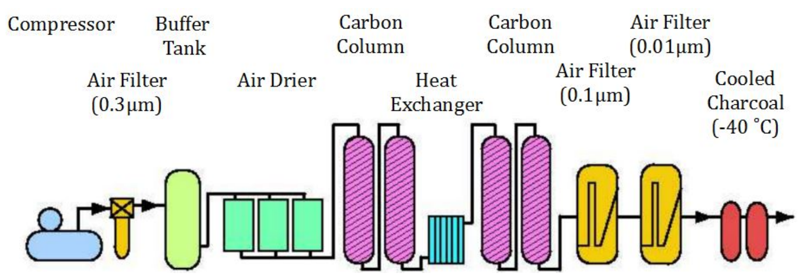

Figure 2.5: Overview of the Super-Kamiokande air purification system. From Ref. [22].

2.2.4 Electronics and Data Acquisition (DAQ) System

A schematic for the ID data acquisition system (DAQ) is presented in Figure 2.6. Signals from ID PMTs are collected by the analog-timing-modules (ATM), located inside Tristan KEK Online (TKO) crates, which are responsible for recording and digitizing the arrival time and the integrated charge for each PMT using an analog-to-digital converter (ADC). The full timing and the integrated charge ranges are 1.6 μs (0.3 ns resolution) and 600 pC

≈ 300 photo-electrons (0.2 pC resolution), respectively. There are 12 PMTs per ATM and 20 ATMs per TKO crate. Eatch TKO crate also contains a go/no-go (GONG) trigger control module and a super-control-header (SCH). The SCH sends information from the ATM to the super-memory-partner (SMP), located within a VME crate. The SMP acts as an information storage buffer, which is to be read out and processed later.

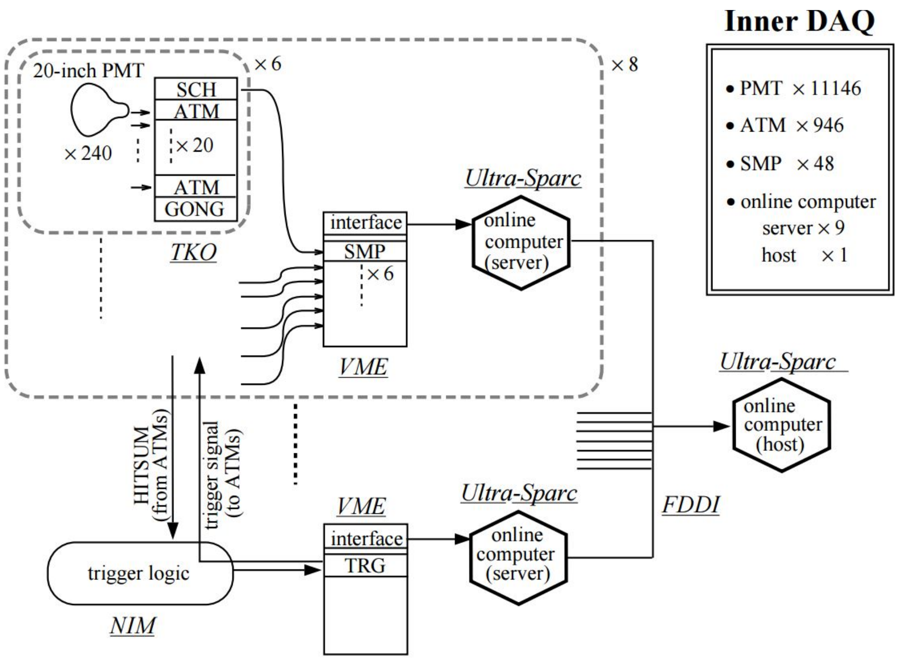

Figure 2.6: Schematic of the data acquisition system for the inner detector (arrows show data flow). From Ref. [22].

The electronics system for the outer detector consists of Charge-To-Timing Converters (QTCs), which read out the OD PMT output signal and generate a timing signal proportional to the total charge. If a 0.25 photo-electron (p.e.) threshold is reached, the signal is then digitized by the Timing-To-Digital Converter (TDC) and merged with the ID data. The signal range of the digitized output is 16 μs (0.5 ns resolution).

Finally, the event hardware trigger system checks the combined total hits from ID ATMs (or OD QTCs) within a 200 ns window. If the number of hits exceeds 29 (19) PMTs for ID (OD), a global trigger signal is issued to the Trigger Module (TRG). The TRG then records the timing and type of the event, generating a global event trigger signal. This initiates the data to be read out and processed.

2.3 Detector Calibration

2.3.1 Relative PMT Gain

To ensure that the PMTs produce a uniform response, their charge gain is measured and each of the high voltages supplying the PMT is individually adjusted. The measurement is performed using a xenon (Xe)-powered scintillator ball, adjusted to give the output at 440 nm, which is near the maximum of the PMT's quantum efficiency. The schematic for this setup is displayed on Figure 2.7. The relative gain G_i of the $i-$th PMT is obtained by

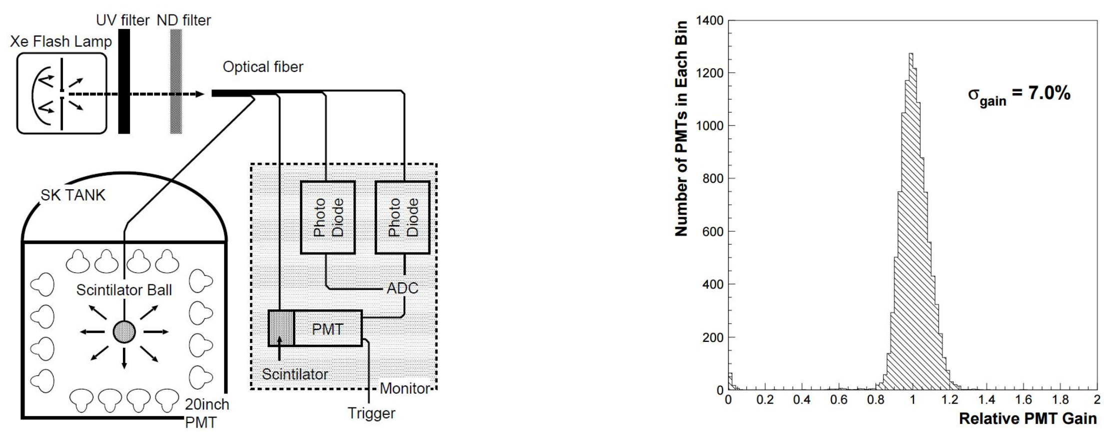

Figure 2.7: Setup for the relative gain calibration system [left] and the relative gain distribution of the PMTs after recalibration [right]. From Ref. [22].

$$G_i = \left(\frac{Q_i}{Q_0 f(\theta)}\right) \cdot l_i \cdot \mathrm{Exp}\left[\frac{l_i}{L}\right] , \tag{2.5}$$

where Q_i is the observed PMT charge, Q_0 is a constant, L is the effective light attenuation length, l_i is the distance to the light source and $f(\theta)$ is the relative PMT photo-sensitivity as a function of the light incident angle.

2.3.2 Relative PMT Timing

Similarly, a uniform PMT timing response is also important. A diffuser ball lighted by the nitrogen laser is used to calibrate the PMT timing response. The laser emits 3 ns light pulses at 337 nm, which are shifted to 384 nm by a dye laser module. This is done for several different positions. PMT timing vs. charge map (TQ map) is constructed for each PMT and is later used within MC and data reconstruction. The calibration setup as well as a sample TQ map for a single PMT are shown in Figure 2.8.

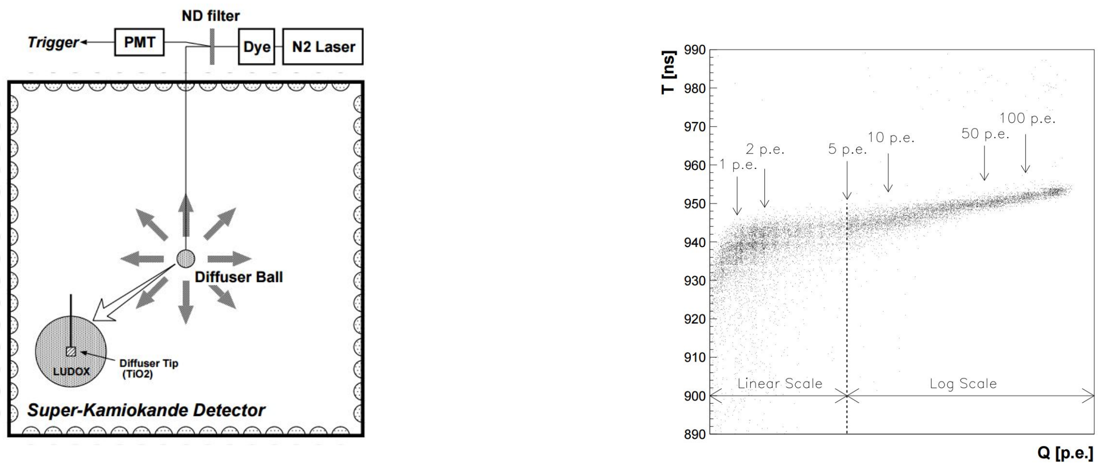

Figure 2.8: Setup for the relative timing calibration system [left] and a sample TQ map for a single PMT [right]. From Ref. [22].

2.3.3 Absolute PMT Gain

To obtain the PMT charge corresponding to 1 p.e., a californium (Cf^{252}) source surrounded by nickel (Ni) wire is used. Neutrons produced by spontaneous fission of Cf are absorbed by Ni, which in turn re-emits γ-rays (mostly at 9 MeV). The observed EM shower deposits no more than 1 p.e. per PMT. For each PMT, charge distribution corresponding to 1 p.e. is determined. The mean value of the charge distribution peaks is found to be 2.055 pC. The calibration system setup as well as the charge distribution of a typical PMT are shown in Figure 2.9.

2.3.4 Water Transparency

Precise measurements of the water transparency are important for obtaining correct MC simulations. The water transparency measurements at SK are performed with three different techniques: using diffuser ball, nitrogen laser beam as well as cosmic ray muons.

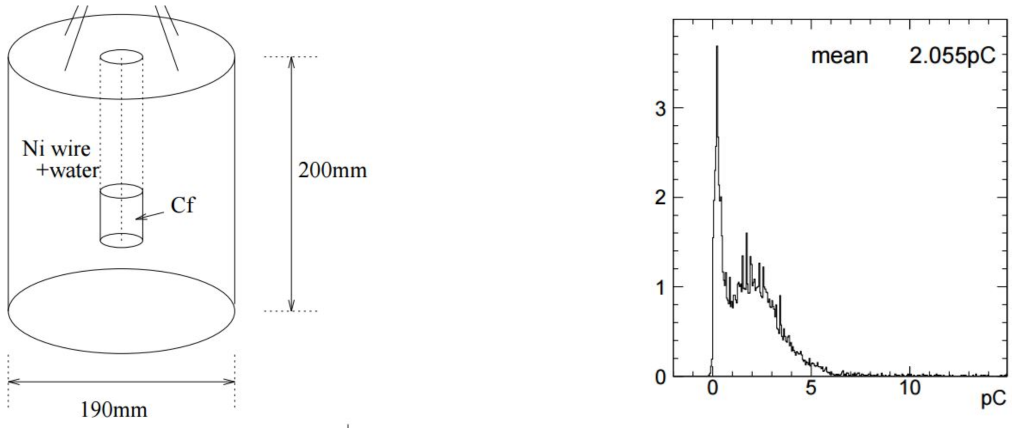

Figure 2.9: Schematic view of the absolute gain calibration system setup [left] as well as the charge distribution of a sample PMT [right]. From Ref. [22].

Diffuser Ball

The attenuation length can be defined as a sum of absorption and scattering coefficients

$$L = \frac{1}{\alpha_{\text{abs}} + \alpha_{\text{scat}}} \ . \tag{2.6}$$

To measure it, a diffuser ball, powered by titanium-sapphire (Ti:Sa) laser pumped by neodymium-doped yttrium aluminium garnet (Nd:YAG) laser, is placed in the detector and the emitted light that passes through water is monitored by a camera on top. The setup is shown on Figure 2.10. After performing several measurements at varying depths and

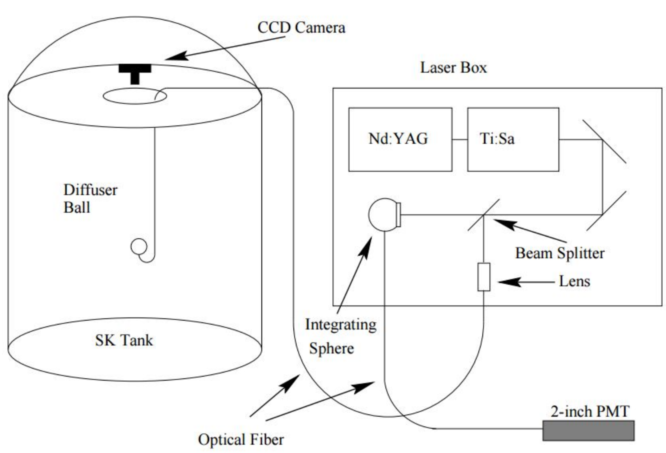

Figure 2.10: Setup for the water transparency measurements using diffuser ball and camera. From Ref. [22].

wavelengths, one can calculate the attenuation length as a function of wavelength using

$$\log\left[\frac{I_{CCD}}{I_{\text{laser}}}\right] = A - \frac{l_d}{L(\lambda)} \ , \tag{2.7}$$

where A is a constant, I_{CCD} is the intensity of light at the charged-coupled device (CCD) camera, I_{laser} is the intensity of light at the monitoring PMT and l_d is the depth of the diffuser ball.

Laser Beam

To measure the absorption and scattering coefficients separately, a nitrogen (N) laser beam is injected from the top of the detector. Each laser, wavelength of 337 nm, 371 nm, 400 nm and 420 nm, fires every 6 seconds during normal data taking. Since the laser shines downward, the measurements of PMT response obtained from the top of the detector correspond to backward light scattering. The setup is depicted in Figure 2.11, along with the measured attenuation coefficient overlaid with the theoretical scattering and absorption models used within the SK MC.

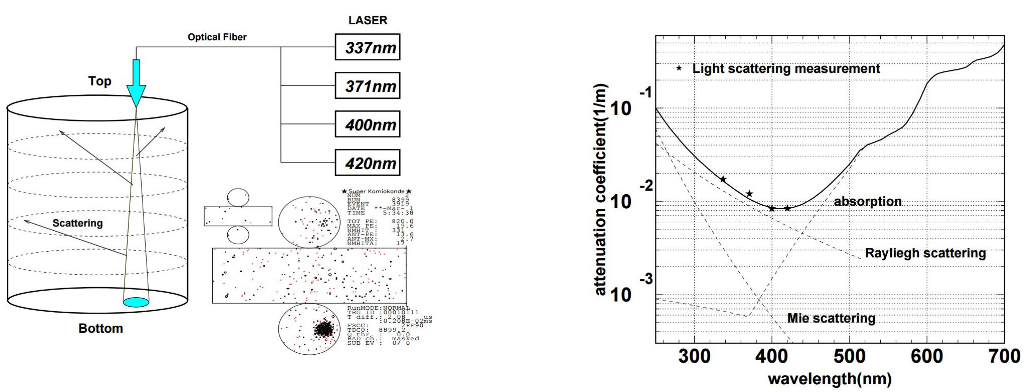

Figure 2.11: Schematic view of the water calibration laser injection setup [left] and the measured attenuation length along with the theoretical predictions [right]. From Ref. [22].

Cosmic Ray Muons

While the previous two methods were intrusive, cosmic ray muons provide continuous detector monitoring throughout regular data-taking periods. We select only the downward going muons. The energetic muons typically deposit nearly a constant 2 MeV/cm amount of energy along their track. The attenuation length can then be inferred from the PMT charge response function

$$Q = Q_0 \cdot \frac{f(\theta)}{l} \cdot \mathrm{Exp}\Big[-\frac{l}{L}\Big] \,, \tag{2.8}$$

where Q_0 is a constant, $f(\theta)$ is the PMT acceptance, l is the photon path length and L is the attenuation length. The results for sample data are shown in Figure 2.12, which yields attenuation length of $\sim$ 100 m. Additionally, time variation of the attenuation length, which is accounted for in the SK MC, is displayed.

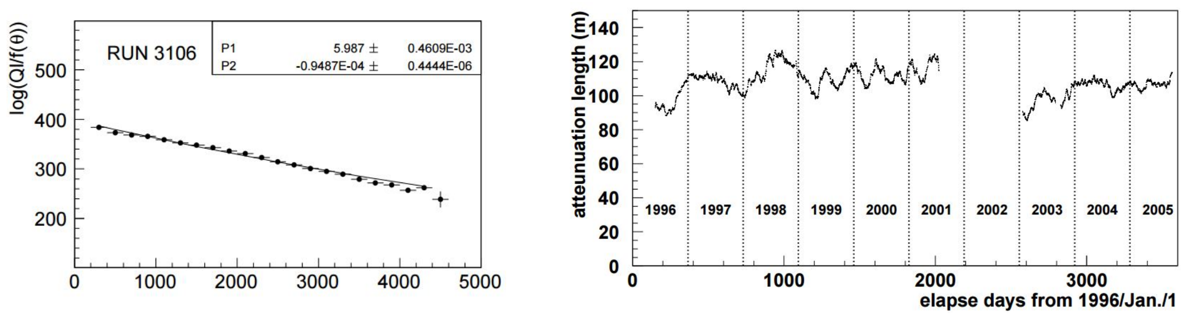

Figure 2.12: Results for $\log[Ql/f(\theta)]$ as a function of l for sample data [left] and water transparency variation over time [right]. From Ref. [22].

2.3.5 Energy Calibration

For the typical nucleon decay searches like $p \to e^+\pi^0$, the analysis is performed by reconstructing the invariant mass and the momentum of the parent particle. For our spectral searches, we will be looking at the momentum distributions of the final state particles. In either case, energy calibration of the detector provides one of the dominant systematic uncertainties for nucleon decay studies. The energy calibration is performed in SK by four independent methods, covering the energy range from $\sim$ 1 MeV/c to 10 GeV/c. These are: decay electrons from stopping muons, π^0 events and the low/high energy stopping muons themselves. The energy calibration is continuously monitored and the uniformity throughout the detector is also accounted for.

Decay Electrons

The energy distribution of the decay electrons produces a well known $\mu \to e^+\nu\nu$ 3-body decay Michel spectrum up to $\sim$ 50 MeV (see also Appendix B). The mean of the Michel spectrum is compared between the data and the MC, as depicted on Figure 2.13 for the SK-I phase of the detector. The decay electrons are selected by the following criteria:

1. time from stopping muon event is $2.0 - 8.0$ μs
2. number of hit PMTs within 50 ns window is > 60 (for SK-I)
3. goodness of vertex fit is > 0.5
4. reconstructed vertex is > 2 m from the ID wall

The (2) criterion rejects 6 MeV γ-rays from μ^- capture on the nucleons. In MC, measured cosmic ray μ^+/μ^- charged muon ratio of 1.37 is used and the μ^- capture is also accounted for.

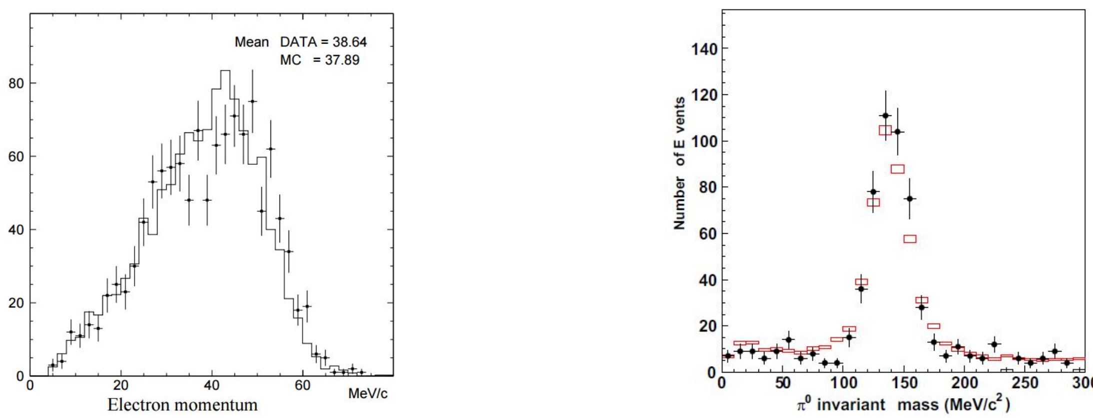

Figure 2.13: Momentum distribution of the stopping muon decay electrons [left] and the reconstructed invariant π^0 mass [right] for SK-I. MC simulation is depicted by continuous line [left] and boxes [right]. From Ref. [22].

Reconstructed Pions

Pions that are produced from the atmospheric neutrino interactions can also be used for energy calibration. As π^0 immediately decays via $\pi^0 \to \gamma\gamma$, the pion invariant mass M_{π^0} can be reconstructed from momenta $P_{\gamma 1}$ and $P_{\gamma 2}$ of the two photons via

$$M_{\pi^0} = \sqrt{2P_{\gamma 1}P_{\gamma 2}(1 - \cos\theta)}\ , \tag{2.9}$$

where θ is the opening angle between γ_1 and γ_2. These events are selected as follows:

1. 2 showering rings
2. 0 decay-electrons
3. reconstructed vertex is > 2 m from the ID wall

where the (2) criterion rejects signal contamination from $\pi^{\pm}\pi^0$ and $\mu^{\pm}\pi^0$ events. The reconstructed pion mass is then compared with MC predictions, as depicted on Figure 2.13, with a clear peak visible around the true pion mass of 135 MeV/c^2.

Low/High Energy Stopping Muons

Recall from Equation (2.2) that the Cherenkov angle depends on the charge particle momentum. One can use the Cherenkov angle of the downward going low-energy ($<$ 400 MeV/c) stopping muons to infer their momenta and then compare with the reconstructed value. The event selection for this study is the following:

1. number of p.e. is < 1500 (for SK-I), i.e. the muon momentum is < 380 MeV/c
2. one cluster of hit OD PMTs
3. entrance point is on the top wall
4. downward going ($\cos\theta_{\text{zenith}} > 0.9$)
5. 1 decay-electron (muon event)

The averaged momentum ratio $P_{p.e.}/P_{\theta}$ of the observed p.e. and the momentum inferred from Cherenkov angle are then compared between the data and the MC.

Since high energy stopping muons deposit about 2 MeV/cm of energy throughout their path, path length can be used to estimate the momentum from 1 to 10 GeV/c independently of the p.e.-based momentum measurement. The event selection for this study is the following:

1. entrance point is on the top wall
2. downward going ($\cos\theta_{\text{zenith}} > 0.94$)
3. 1 decay-electron (muon event)

4. reconstructed muon path length > 7 m

To ensure that energy calibration is precisely accounted for, detector uniformity as well as time variation of the uncertainty is also studied. The combined uncertainty from energy calibration for SK-I is shown in Figure 2.14. The total combined energy calibration uncertainty for each SK phase, SK I-IV, is within 3% for high energies ($\gtrsim 100$ MeV) and $< 1\%$ for low energies ($\sim 10 - 100$ MeV).

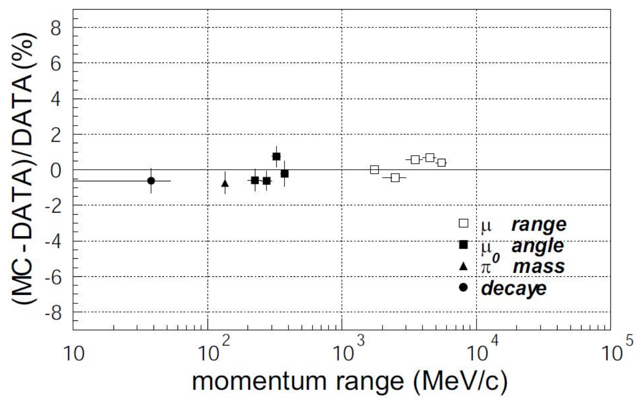

Figure 2.14: Results for SK-I energy calibration. From Ref. [22].

2.4 Data Taking Periods

The Super-Kamiokande has collected data during four different experimental phases: SK-I (May 1996-Jul. 2001, 1489.2 live days), SK-II (Jan. 2003-Oct. 2005, 798.6 live days), SK-III (Sep. 2006-Aug. 2008, 518.1 live days) and the ongoing SK-IV experiment (Sep. 2008-Oct. 2013, 1632.3 live days), corresponding to a combined exposure of 273.4 kton·years. In the SK-II phase of the detector the photo-coverage was only 19%, due to a PMT implosion accident. The full photo-coverage was restored in SK-III and electronics were upgraded in SK-IV, allowing for a better decay-electron detection efficiency.

Chapter 3

Monte Carlo Simulations

3.1 Signal: Nucleon Decay

3.1.1 Assumptions

Nucleon decay generation is typically done by randomly generating the final state particles of the decay in the parent nucleon's center of mass frame, taking into account the 4-momentum (energy and momentum) conservation. The final state particles are then Lorentz boosted to the lab frame, which allows to account for the Fermi motion if the parent nucleons are bound inside the nucleus (i.e. within ^{16}O). Dinucleon decay is generated similarly, but now one obtains a 2-body decaying system (nn, np, pp). The nucleon decay MC is spin-insensitive.

The above approach is a general model independent technique for rare searches, which does not depend on the specifics of how a decay is actually mediated and implicitly assumes a flat phase-space distribution (see Appendix B). This has been a standard approach for the past experimental nucleon decay searches (e.g. at IMB [131] and Frejus [138]). In the case of the typical 2-body decay channel, such as $p \to e^+\pi^0$, the energy distribution of the final state particles is fully determined by kinematics. This is so, since each of the resulting particles takes $\sim m_n/2$ of energy (free nucleon decay) and the above approach works well. On the other, for $n > 2$ body decays, such as $p \to e^+\nu\nu$ or $p \to \mu^+\nu\nu$, the energy spectra is not uniquely determined by the 4-momentum conservation and has a distribution from 0 to $m_n/2 \approx 470$ MeV and a mean of ~ 313 MeV (free nucleon decay). In such a scenario, the energy dependence of the matrix element, which is determined by the mediating mechanism, can play a role in $n > 2$ decays. While we want to keep the searches as model independent as possible, it is also important to understand the degree of approximation used in generating the trilepton nucleon decays with a flat phase-space distribution, which experiments in the past have just assumed.

Using effective 4-fermion interaction formalism of the Fermi theory and employing a relatively general set of assumptions, one can approximate [157] the decay spectra of $p \rightarrow e^+\nu\nu$ and $p \rightarrow \mu^+\nu\nu$. The approximation method is discussed in Appendix B. We have used this result to confirm that the e^+ and μ^+ energy distributions, which we will use in the nucleon decay analysis and which are generated using the standard SK nucleon decay MC that assumes a flat phase-space distribution, are reasonable. In fact, the technique outlined in Ref. [157] can be useful for other decay searches that satisfy the above assumptions, such as $p \rightarrow e^+e^-e^+$.

We note that in the nucleon decay analyses it is generally assumed that the bound and the free nucleons have the same decay rate $\Gamma_{free} \approx \Gamma_{bound}$. The phase space for the two are different, due to nuclear environment, which in principle affects the bound nucleon lifetime $\tau_{bound} = 1/\Gamma_{bound}$. This effect, however, is taken to be negligible.

3.1.2 Nuclear Effects

Fermi Motion and Nucleon Decay Position

If a nucleon decay occurs inside oxygen ^{16}O, the bound parent nucleon has Fermi momentum. On the other hand, if the nucleon originates from hydrogen H, it is free (stationary). All of the dinucleon decays originate from the bound nucleons of ^{16}O. In the SK nucleon decay MC simulations, the Fermi momentum of nucleon decay is based on a spectral function found by the $e-^{12}$C scattering experiments [162]. The S- and P-state momenta based on theoretical calculations and the experimental data are shown on Figure 3.1. On the other hand, atmospheric neutrino MC uses Fermi momentum calculated from the relativistic Fermi gas model, as we will discuss later. The difference between the two models is used to estimate the systematic uncertainty.

The position of the decaying nucleon is determined using the Woods-Saxon model [163],

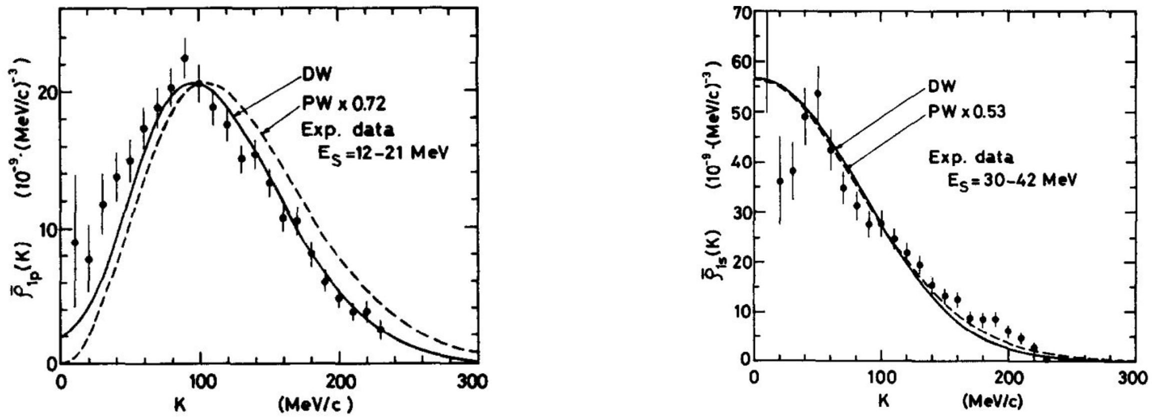

Figure 3.1: Theoretical calculations (solid and dashed lines) [161] for the $1p_{3/2}$ proton state (left) and $1s_{1/2}$ proton state (right) of ^{12}C, compared with experimental data. From Ref. [162].

according to the following distribution

$$\rho_n(r) = \frac{Z}{A} \times \frac{\rho(0)}{1 + \text{Exp}[\frac{r-a}{b}]} \ , \tag{3.1}$$

where $\rho_n(r)$ is the nuclear density as a function of radial distance r from the nuclear center, $\rho_0 = 0.48\ m_\pi^3$, $a = 2.69$ fm is the maximal nuclear radius for oxygen, $b = 0.41$ fm is the "surface thickness" of the oxygen nucleus and Z and A are the atomic and the mass numbers[1]. From the above, one can determine the Fermi surface momentum using

$$p_F(r) = \left(\frac{3}{2}\pi^2 \rho_n(r)\right)^{1/3} \ . \tag{3.2}$$

The Fermi surface momentum is used for studying nuclear interactions of the mesons, which are important in nucleon decay searches such as $p \to l + meson$ (see Ref. [132]). The same technique is used for neutrino meson-production interactions in the atmospheric MC simulations, as discussed later.

Binding Energy

The nuclear binding energy is taken into account by modifying the invariant mass of the nucleon according to $M_n^* = M_n - E_b$, where M_n^* is the modified nucleon mass, M_n is the rest nucleon mass and E_b is the binding energy. Binding energy E_b is assumed to

[1] For ^{16}O, $Z = 8$ and $A = 16$.

have a random Gaussian distribution with a mean and the standard deviation of $(\mu, \sigma) = (39.0\text{ MeV}, 10.2\text{ MeV})$ for the S-state and $(\mu, \sigma) = (15.5\text{ MeV}, 3.82\text{ MeV})$ for the P-state. The results for proton in ^{16}O are shown in Figure 3.2.

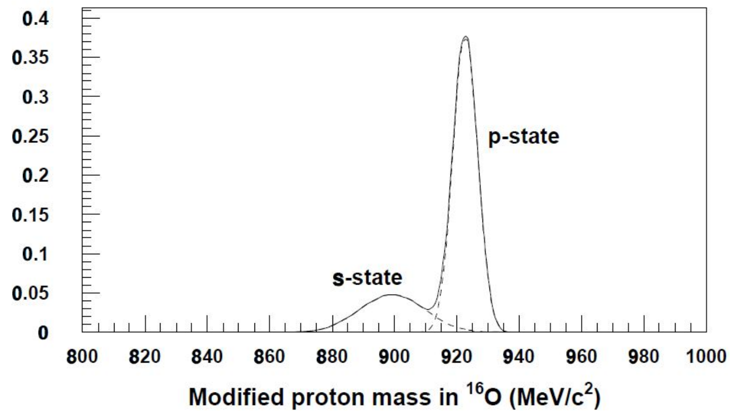

Figure 3.2: Proton invariant mass in ^{16}O, modified by nuclear binding energy. From Ref. [164].

Correlated Decay

In the nuclear environment it is predicted that due to overlapping wave functions of the nucleons, an additional "spectator" nucleon becomes involved in the decay and thus modifies the invariant mass of the decaying system. Pictorially, this effect can be viewed as several bound nucleons, which have Fermi motion, colliding and redistributing momenta. In case this happens, a single nucleon decay effectively becomes a 2-body system decay and dinucleon decay becomes a 3-body system decay. Approximately 10% of nucleon decays are predicted to experience this effect [165], which SK MC simulations take into account. We consider a 100% systematic uncertainty for correlated decay, since it is not well studied.

Nuclear De-excitation

As the nucleon decays, the remaining nucleus (e.g. $^{16}\text{O} \to {}^{15}\text{N}$) can be left in an excited state, which then de-excites through a γ-ray or a nucleon emission. These effects were calculated in Ref. [166] (more recently in Ref. [167]), as summarized in Table 3.1. They are included in SK MC simulations. For the nuclear decays to the states with a de-excitation nucleon, no γ-ray is generated. The de-excitation γs are particularly important for some nucleon decay analyses, such as $p \to \nu K^+$ [168] and $n \to \nu\nu\nu$ [169].

State	Energy of γ	Probability
$p_{3/2}$	6.3 MeV	41%
$p_{3/2}$	9.9 MeV	3%
$s_{1/2}$	7.0 MeV	4%
others	3.5 MeV	16%
p/n emission	-	11%
ground state	-	25%

Table 3.1: Summary of nuclear de-excitation after nucleon decay [166].

3.1.3 Generation of τ and X

Since τ lepton decay is not included in the GEANT-3 [170] package that is used for the SK detector simulation (see Section 3.3), we use the dedicated TAUOLA [171] package for decaying the τ in the $np \to \tau^+\nu$ search[2]. For the $np \to \tau^+\nu$, we will be interested only in the leptonic τ channels $\tau \to e^+\nu\nu$ and $\tau \to \mu^+\nu\nu$. We have confirmed that the e^+ and μ^+ energy spectra from these decays, for both stationary and moving τ, agrees well with the theoretical predictions of the $(V - A)$ SM theory [173], using the calculations of Ref. [157] (see Appendix B).

For the $p \to e^+X$ and $p \to \mu^+X$ decays, X is assumed to be a single unknown massless and invisible particle, which by spin conservation is a boson. For the analysis, X is generated as a neutrino, since SK nucleon decay MC is spin insensitive and the final state neutrino is also effectively massless and invisible.

3.2 Background: Atmospheric Neutrinos

The main background for nucleon decay searches comes from interactions of atmospheric neutrinos, which are produced by cosmic rays. The cosmic rays mainly consist of protons and α-particles ($\sim 99\%$), which strike the atmosphere. The isotropically distributed cosmic rays interact with the air molecule nuclei, producing copious amounts of pions and kaons. The decay of charged pions $\pi^\pm$ leads to an eventual production of two muon neutrinos (ν_μ or $\overline{\nu}_\mu$) and one electron neutrino (ν_e or $\overline{\nu}_e$). These processes result in a specific neutrino flux composition at the surface of the Earth. The whole reaction chain is shown schematically on Figure 3.3. While most of the neutrinos pass through Earth (travelling 10 - 10,000 km

[2] The τ decay is treated in the same manner within the SK ν_τ-appearance analysis [172].

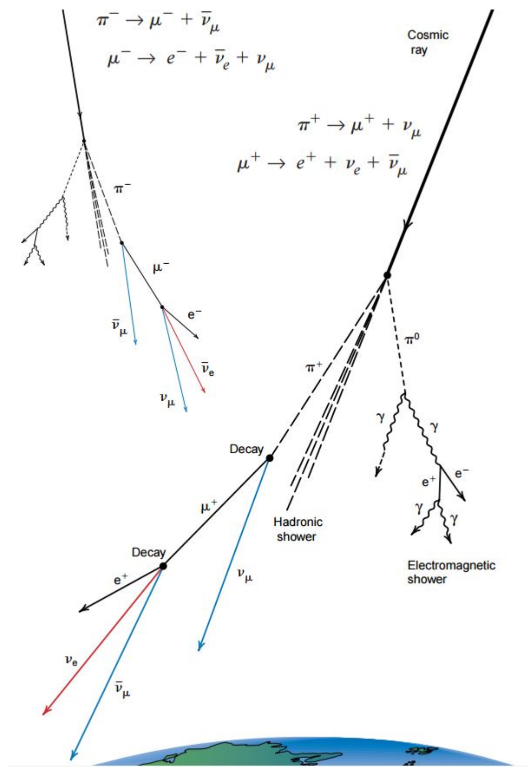

Figure 3.3: Schematic view of cosmic ray interactions in the atmosphere. From Ref. [174].

distance) without interaction, some interact at Super-Kamiokande and a neutrino event rate of about ~ 8 events/day is observed within the detector.

3.2.1 Neutrino Flux

Atmospheric neutrino flux at Super-K is modeled using calculations of Honda *et. al.* (Honda flux) [175], which parametrize and fit experimental cosmic ray data, as shown on Figure 3.4. These 3-dimensional calculations propagate the cosmic rays through the atmosphere and take into account the effects of geomagnetic field and solar wind, which can affect the cosmic ray flux by up to a factor of 2 at 1 GeV and $\sim$10% at 10 GeV energy range. Interactions with the air nuclei are treated using NUCRIN [188] and DPMJET-III [189] models, with the resulting secondary particle profile for mesons and kaons used for neutrino flux computation. Neutrino flux calculations of G. Battistoni *et. al.* (Fluka flux) [190] and G.D. Barr *et. al.* (Bartol flux) [191] are used for comparison with Honda flux, as shown on Figure 3.4, to determine the systematic uncertainty. Flux calculations cover the neutrino energy ranging from 30 MeV to 3 TeV.

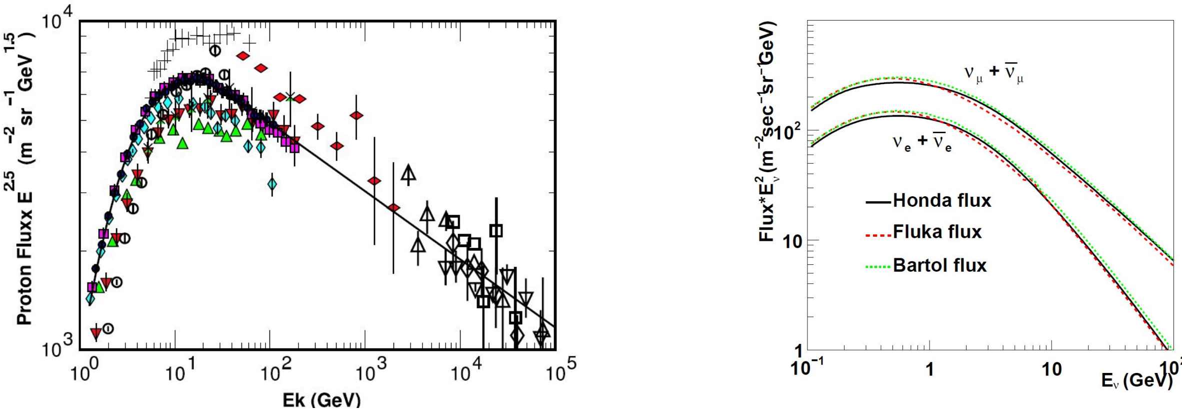

Figure 3.4: [left] Primary cosmic ray flux measurements compared with the Honda flux model (solid line) for protons at solar minimum. The data are taken from Webber *et. al.* [176] (crosses), LEAP [177] (upward triangles), WIZARD-MASS [178] (open circles), CAPRICE-94 [179] (vertical diamonds), IMAX [180] (downward triangles), BESS [181] (closed circles), AMS [182] (squares), Ryan *et. al.* [183] (horizontal diamonds), JACEE [184] (downward open triangles), Ivanenko *et. al.* [185] (upward open triangles), Kawamura *et. al.* [186] (open squares) and RUNJOB [187] (open diamonds). [right] Atmospheric neutrino flux at Super-Kamiokande as predicted by the Honda (solid line), Fluka (dashed line), and Bartol (dotted line) flux models. From Ref. [175].

3.2.2 Neutrino Interactions

At the SK site and within the surrounding rock, neutrino interactions have been simulated using the NEUT [192] model and cross-checked with the NUANCE [193] model. The following interactions are calculated:

$$\begin{aligned}
\text{CC/NC (quasi-)elastic scattering:} \quad & \nu + N \rightarrow l + N' \\
\text{CC/NC single-meson production:} \quad & \nu + N \rightarrow l + N' + \text{meson} \\
\text{CC/NC coherent-pion production:} \quad & \nu +^{16} O \rightarrow l +^{16} O + \pi^{\pm,0} \\
\text{CC/NC deep inelastic scattering (DIS):} \quad & \nu + N \rightarrow l + N' + \text{hadrons}\ .
\end{aligned}$$

Here, ν represents an incoming neutrino or anti-neutrino of some flavor (e or μ), N and N' are the original and the outgoing nucleons (p or n), respectively, and l is an outgoing lepton. The outgoing lepton l can be a charged lepton, if there is a charged current (CC) interaction, or a neutrino, for the neutral current (NC) interaction. Reactions with negligible cross-sections, such as neutrino-electron scattering, are omitted. Below we provide an overview of the above processes. Since CC quasi-elastic (QE) scattering and single-pion production provide the predominant majority of the background for our analyses, they will be discussed in more detail. Further information regarding the neutrino interactions and the associated systematic uncertainties can be found in Ref. [160, 194].

Elastic and Quasi-Elastic Scattering

These events typically result in a single Cherenkov ring pattern and can sometimes give off a recoiling proton above threshold. For a free proton scattering, the cross-section of the charged current quasi-elastic interaction is calculated from the $(V - A)$ theory and is given by Llewellyn-Smith [195] as

$$\frac{d\sigma^{\nu(\overline{\nu})}}{dq^2} = \frac{M^2 G_F^2 \cos^2\theta_C}{8\pi E_\nu^2}\Big[A(q^2) \pm B(q^2)\frac{s-u}{M^2} + C(q^2)\frac{(s-u)^2)}{M^4}\Big] , \tag{3.3}$$

where E_ν is the neutrino energy, M is the target nucleon mass, G_F is the Fermi constant, θ_C is the Cabbibo angle, q is the 4-momentum transferred to the lepton and s and u are the Mandelstam variables. The form factors $A(q^2)$, $B(q^2)$ and $C(q^2)$ can be re-written in terms of axial-vector and vector form factors $F_V^1(q^2)$, $F_V^2(q^2)$ and $F_A(q^2)$ as well as the electric and magnetic form factors $G_E(q^2)$ and $G_M(q^2)$, which are typically the ones used in the experiments. Two additional parameters, the vector mass M_V and the axial-vector mass M_A, are needed to be specified in order to fully determine the form factor structure. They are taken to be $M_V = 0.84$ GeV and $M_A = 1.2$ GeV (see K2K [196] measurement).

For bound nucleon scattering (^{16}O nuclei), the calculation of Smith and Moniz [197] is used. Nucleons are treated using relativistic Fermi gas model with a flat momentum distribution up to 225 MeV/c (Fermi surface momentum). Models of Ref. [198, 199] better account for the intermediate energy ranges and are used to determine the systematic uncertainty. Pauli exclusion principle is enforced by requiring that scattered nucleon has momentum higher than the Fermi surface momentum.

The cross-sections for the neutral current elastic scattering are estimated using the following relations [200, 201]:

$$\begin{aligned}
\sigma(\nu p \to \nu p) &= 0.153 \times \sigma(\nu p \to e^- p) \\
\sigma(\overline{\nu} p \to \overline{\nu} p) &= 0.218 \times \sigma(\overline{\nu} p \to e^+ p) \\
\sigma(\nu n \to \nu n) &= 0.150 \times \sigma(\nu p \to \nu p) \\
\sigma(\overline{\nu} n \to \overline{\nu} n) &= 1.000 \times \sigma(\nu \overline{p} \to \nu \overline{p})
\end{aligned}$$

Comparison between data and NEUT simulations for ν and $\overline{\nu}$ quasi-elastic scattering is shown on Figure 3.5.

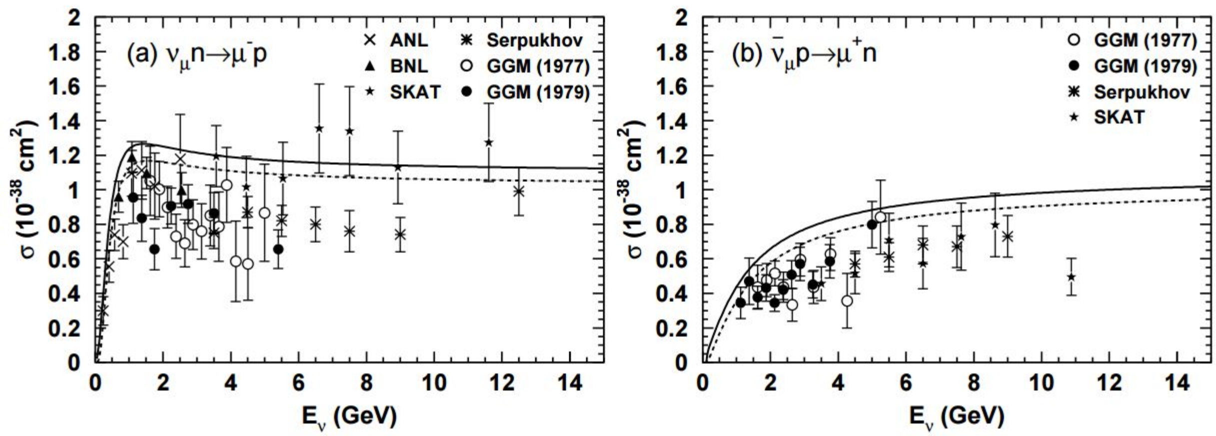

Figure 3.5: Comparison of NEUT MC simulations (solid line) and data for the ν and $\overline{\nu}$ cross- sections of the charged current quasi-elastic scattering. The data from ANL [202], Gargamelle [203, 204, 205], BNL [206], Serpukhov [207] and SKAT [208] are shown. From Ref. [209].

Single-Meson Production

Single-meson production of π, K and η is simulated using the model of Rein and Sehgal [210, 211]. The production happens through baryonic resonance via two steps:

$$\nu + N \to l + N^*$$
$$N^* \to m + N'$$

where m is a meson, N and N' are nucleons and N^* is the baryon resonance. If the decay width of baryon resonance is negligible, the differential cross-section of single meson production is given by

$$\frac{d^2\sigma}{dq^2 dE_\nu} = \frac{1}{32\pi M E_\nu^2} \times \frac{1}{2} \sum_{j,\mathrm{spin}} |T(\nu N \to l N_j^*)|^2 \delta(W^2 - M_j^2) \ , \tag{3.4}$$

where M is the target nucleon mass, E_ν is the neutrino energy, W is the invariant mass of the hadronic system (intermediate baryon resonance), M_j is the baryon resonance mass and $T(\nu N \to l N_j^*)$ is the resonance production amplitude, calculated from the Feynman-Kislinger-Ravndal model [212]. If the resonance width is non-negligible, δ-function in Equation (3.4) is substituted by the usual Breit-Wigner formula

$$\delta(W^2 - M_j^2) \to \frac{1}{2\pi} \frac{\Gamma}{(W - M_j)^2 + \Gamma^2/4} \ . \tag{3.5}$$

For the above calculations, W was restricted to be < 2 GeV/c^2 (region above 2 GeV/c^2 is treated in DIS) and M_A is taken to be 1.2 GeV as for QE scattering. A total of 28 resonances are considered in SK simulations. Angular distribution of the final state pions is found from the $\Delta(1232)$ resonance, while angular distribution of pions coming from other resonances is set to be isotropic. The simulated π^+ angular distribution is found to be in agreement with experimental data from $\nu p \to \mu^- \pi^+ p$ scattering [213]. Pion-less Δ decay [214], where 20% of events only have lepton and a nucleon, is also simulated. As before, Pauli exclusion principle is taken into account by requiring that the scattered nucleon momentum is greater than the Fermi surface momentum.

Coherent-Pion Production

If the incoming neutrino energy is small, it effectively "sees" the whole ^{16}O nucleus. Due to the large mass, the nucleus is not affected much in the interaction and the resulting pion has a distinctive forward scattering in the angular distribution. This process is also simulated using the Rein and Sehgal model [211]. However, the K2K data [215] agrees better with the model of Kartavtsev *et. al.* [216], which is used to determine the systematic uncertainty.

DIS

If the incoming neutrino energy is high, the neutrino can fragment the nucleon it collides with. The DIS is simulated using GRV98 (Glück-Reya-Vogt) [217] parton distribution function. Here, one restricts $W > 1.3$ GeV/c^2. In the region 1.3 GeV/$c^2 < W < 2.0$ GeV/c^2 only pions are considered as the outgoing mesons. Their multiplicity is required to be larger than 1, such that the process does not overlap with the single-pion production, with the mean multiplicity estimated from the Fermilab bubble chamber experiment [218] and its forward-backward asymmetry further studied by the BEBC experiment [219]. For region $W > 2$ GeV/c^2, hadronic system kinematics are determined using PYTHIA/JETSET [220] package, which allows to also treat the K, η and other mesons.

The neutral current DIS cross-section is determined from the DIS charged current cross-section through the means of empirically determined relations [221, 222], similar to the quasi-elastic scattering.

Nuclear Effects

As the mesons are created inside ^{16}O, they may hadronically interact within the nucleus itself via charge exchange, absorption or inelastic scattering. This is particularly relevant for pions, which have large cross-section around $E_\nu \sim 1$ GeV. Their position within the nucleus is calculated by the Woods-Saxon model [163], which is also used for nucleon decay MC. Cascade model is then used to simulate the interaction, which is determined by the the mean free path found from Ref. [223]. Fermi motion and Pauli exclusion principle are taken into account as for the other interactions. The nuclear effect simulations are verified by the experiments using the pion$-^{12}C$ scattering, pion$-^{16}O$ and the pion photo-production $(\gamma +^{12} C \rightarrow \pi^- + X)$ [224, 225]. Other mesons are also considered.

Nucleon re-scattering is also treated with a cascade model. Scattering cross-sections are taken from experiment [226] and the pion production from Δs is taken into account using the isobar production model [227].

Full MC simulation and data comparison of neutrino cross-section is shown on Figure 3.6. Simulations are seen to describe the data well.

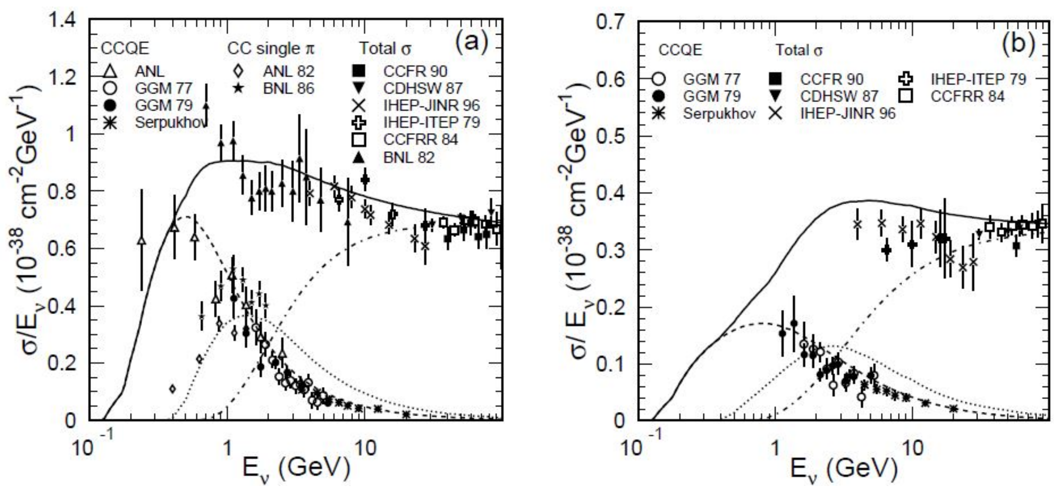

Figure 3.6: Total neutrino (a) [left] and anti-neutrino (b) [right] cross sections as a function of energy. The calculated quasi-elastic scattering cross section is shown in the dashed line, that of single meson production appears in the dotted line, and the dash-dotted line shows deep inelastic scattering. Data from several experiments are overlaid. From Ref. [160].

3.2.3 Neutrino Oscillations

The phenomena of neutrino oscillations [32] originates from the mismatch of the neutrino flavor and mass eigenstates and signifies that neutrinos have mass. This was established by Super-Kamiokande [17] in 1998 for atmospheric $\nu_\mu \leftrightarrow \nu_\tau$ neutrino oscillation. Similarly, the solar neutrino $\nu_e \leftrightarrow \nu_\mu(\nu_\tau)$ oscillation was established by SNO [18] in 2001.

To take into account neutrino oscillations, the generated SK atmospheric neutrino MC events are reweighed accordingly. The following oscillation parameters have been assumed for the atmospheric MC used in our analysis [152, 228]: normal hierarchy, $\Delta m^2_{32} = 2.1\times10^{-3}$ eV^2, $\Delta m^2_{21} = 7.6 \times 10^{-5}$ eV^2 $\sin^2 2\theta_{23} = 1.0$, $\sin^2 2\theta_{12} = 0.84$ and $\delta_{\rm CP} = 0$. The final background rates for each SK data-taking period are normalized by the observed total sub-GeV event rate (see Chapter 5 for sub-GeV sample characteristics).

3.3 Detector

After the initial intra-nuclear interactions, propagation of particles through the detector, Cherenkov radiation, PMT response and the electronics (including the dark noise) are all taken into account by the SK detector simulation software SKDETSIM, which based on the GEANT-3 [170] package.

For hadrons, interactions above 500 MeV are treated with GCALOR [229, 230]. Interactions below 500 MeV are done with a custom package [231] based on the $\pi-^{16}$O [232] and the $\pi - p$ scattering data [233]. For details regarding how $K^0_L \rightarrow K^0_S$ regeneration and Kaon-nucleon interactions are taken into account see Ref. [234].

Cherenkov radiation is included by generating photons according to Section 2.1. Rayleigh scattering, Mie scattering and absorption are all taken into account as shown on Figure 2.11.

For production of the upward-going muons and interactions within the surrounding rock (assumed to be sillicon-oxide (SiO_2), with density of 2.65 g/cm^3) are simulated with NEUT. These processes are not relevant for our analysis.

Chapter 4

Event Reconstruction

The event reconstruction algorithm is applied to fully contained events after data reduction (see Chapter 5). The same algorithm is applied to both, the data and the MC. The reconstruction procedure contains the following steps:

1. **Vertex Fitting:**
   the vertex position point is determined from maximizing a likelihood function based on the PMT timing distributions; Cherenkov cone direction and the ring edges are estimated.

2. **Ring Counting:**
   search for additional rings is performed using a likelihood method and the vertex and position of the dominant ring (as determined in the previous step); the total number of rings is estimated.

3. **Particle Identification (PID):**
   a likelihood function, based on ring pattern and opening angle, is formed to classify each ring as showering or e-like (for $e^{\pm}, \gamma$) and non-showering or μ-like (for $\mu^{\pm}, \pi^{\pm}$).

4. **Momentum Determination:**
   the total ring charge within a 70° cone is converted to ring momentum, using MC simulation and detector calibration data.

5. **Ring Number Correction:**
   "fake" low energy rings that overlap with primary rings are removed.

6. **Decay Electron Search:**
   decay electrons from the primary events are obtained.

In addition the above standard algorithm, alternative and more specialized tools also exist, such as the multi-vertex fitter (MVFIT). However, they are not relevant for the studies presented within this work and thus will be omitted. Below, we provide an overview of each algorithm step. For a more comprehensive description see Ref. [164].

4.1 Vertex Fitting

The vertex fitting algorithm consists of three steps: vertex point fit, ring edge finding and a refined vertex fit (TDC-fit).

4.1.1 Vertex Point Fit

Point fit estimates the vertex position. The fit samples various test vertices and, assuming that all photons originated simultaneously from a single point, maximizes the "vertex goodness" function $G_{ver.}$. The function depends on the subtracted photon time of flight (TOF) recorded PMT timings and is given by

$$G_{ver.} = \frac{1}{N} \sum_i \text{Exp}\Big[- \frac{(t_i - t_0)^2}{2(1.5 \times \sigma)^2} \Big] , \tag{4.1}$$

where N is the number of hit PMTs, t_i is the TOF-subtracted timing of the i^{th} PMT, t_0 is a free parameter chosen to maximize $G_{ver.}$ and σ is the PMT resolution (2.5 ns). Ring direction is also roughly estimated in this step, by summing up the detected p.e. vector.

4.1.2 Ring Edge Finding

Using information from the previous fit portion, the Cherenkov opening angle and the ring edge position are obtained. A distribution $Q(\theta)$ is built from detected p.e.s as a function of Cherenkov opening angle θ. The ring edge is then estimated where the second derivate of $Q(\theta)$ vanishes.

Various directions and opening angles are tested to maximize the "ring direction goodness" function

$$G_{dir} = \frac{\displaystyle\int_0^{\theta_C} Q(\theta)d\theta}{\sin\theta_C} \times \mathrm{Exp}[-\frac{(\theta_C - \theta_{exp})^2}{2\sigma_a^2}] \ , \tag{4.2}$$

where θ_C is the test opening angle, $Q(\theta)$ is the charge distribution relative to the test direction, θ_{exp} is the expected opening angle ($\theta_{exp} = 42^\circ$ for γ) of the ring and σ_a is its resolution. The initial test direction is found by the previous step.

4.1.3 Refined Vertex Fit

The TDC-fit re-computes the vertex position by also utilizing directional and opening angle information found above. Unlike the vertex point fit, which assumed that all photons originated simultaneously at a single vertex point, TDC-fit takes into account that photons originated along the charged particle track length to get the residual PMT timing and maximizes the corresponding likelihood function. Scattered light is also considered here.

An additional fit (MS-Fit), which uses particle ID (described later), further improves on the vertex position identification for the single-ring events.

4.2 Ring Counting

After the main ring has been identified, additional rings (up to 5) are searched for using Hough transform [235] pattern recognition technique and the likelihood method. With the Hough transform, a "virtual ring" pattern (42° Cherenkov angle) is considered around each hit PMT. The "virtual rings" are weighted by the charges from the hit PMTs and a "real" ring is identified from the peak of the overlapping "virtual" distributions. The concept is illustrated in Figure 4.1. In practice, instead of virtual circles, the method is implemented by using charge distribution function for each hit PMT and the a ring candidate is identified by the peak in the overlapping distributions. A log-likelihood method is then used to determine if a true ring has been found.

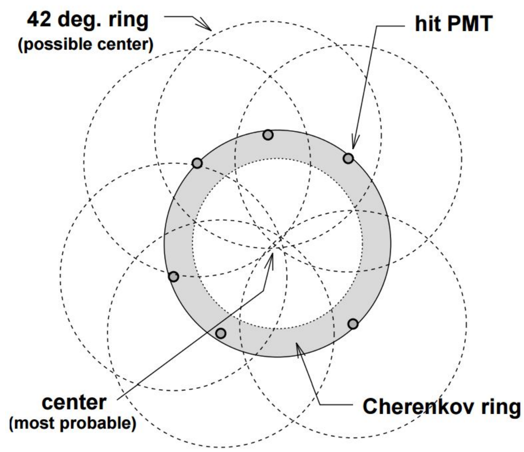

Figure 4.1: The basic concept of the Hough transform applied to Cherenkov rings. The charge in a PMT is distributed along a circle corresponding to a 42° Cherenkov opening angle as seen from the event vertex. The circles of the hit PMTs from the same Cherenkov ring will then overlap in the center of the actual ring. From Ref. [236].

4.3 Particle Identification

Particle identification in SK classifies the observed rings as showering or e-like (for $e^{\pm}, \gamma$) and non-showering or μ-like (for $\mu^{\pm}, \pi^{\pm}$). The e-like rings produce a fuzzy pattern, due to scattering and electromagnetic showers (bremsstrahlung, followed by the $\gamma \to e^+e^-$ pair production). On the other hand, a clear pattern is observed for heavier particles which

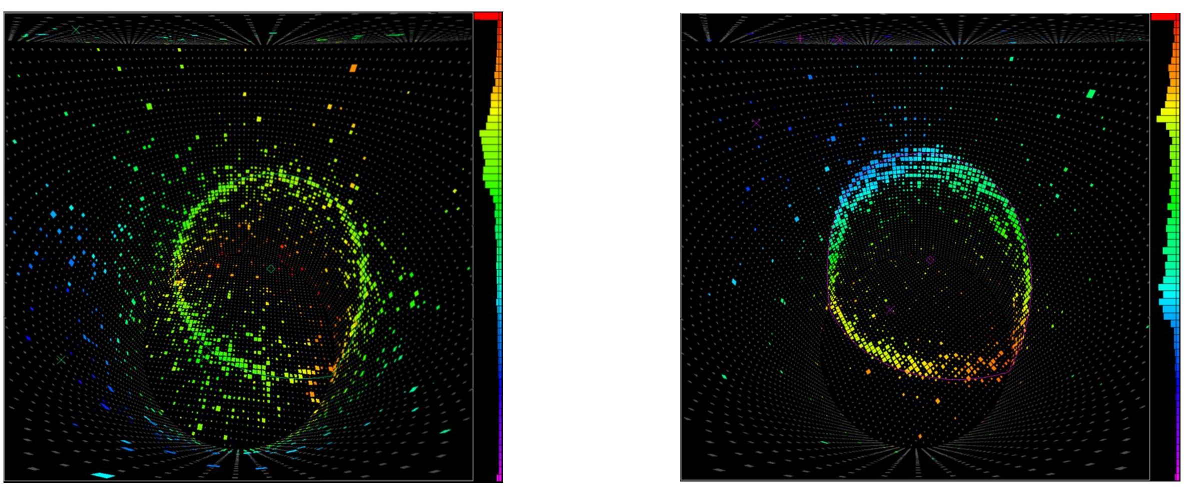

Figure 4.2: Event display of single-ring electron [left] and single-ring muon [right] data events, with reconstructed momenta of 492 MeV and 603 MeV as well as the time scale widths of 130 ns and 162 ns, respectively. Color shows time of arrival of light to PMTs. An e-like event gives diffused ring pattern, while a μ-like event has a sharp ring edge. From Ref. [237].

don't scatter much. The two types of rings are illustrated in Figure 4.2.

The reconstruction PID algorithm considers expected charge distribution functions for the two types of rings, found from the MC simulations and the analytical considerations. A likelihood test is then performed to determine which type of ring is seen. Figure 4.3 shows PID likelihood distribution for SK-I and the relevant contributing MC processes in FC sample with a visible energy below 1.33 GeV. Quality of the PID algorithm has been

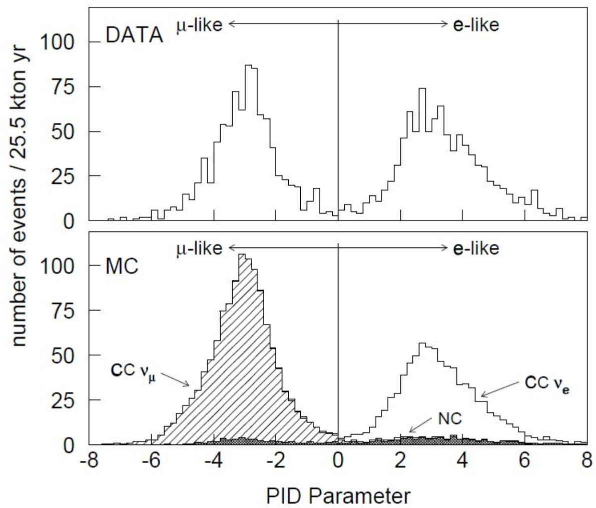

Figure 4.3: PID likelihood distribution for data and atmospheric MC with a visible energy below 1.33 GeV. Good separation between e-like and μ-like events is seen. From Ref. [164].

checked using 1 kiloton water Cherenkov detector with electron and muon beams coming from the 12 GeV synchrotron at KEK [238].

4.4 Momentum Determination

Ring momentum is calculated from the integrated charge within 70° cone around ring's reconstructed direction. The integrated charge for ring n, R^n_{TOT}, is given by

$$R^n_{TOT} = \frac{G_{\mathrm{MC}}}{G_{\mathrm{Data}}}\Big(\alpha \sum_{\substack{\theta_{i,n}<70^\circ \\ -50\ \mathrm{ns}<t_i<250\ \mathrm{ns}}} \Big(q^{\mathrm{Obs.}}_{i,n}\ \mathrm{Exp}[\frac{r_i}{L}]\ \frac{\cos\omega_i}{f(\omega_i)}\Big) - \sum_{\theta_{i,n}<70^\circ} S_i\Big)\ . \tag{4.3}$$

Here, the variables stand for:

α − normalization factor

$G_{\text{Data}}, G_{\text{MC}}$ – relative PMT gain parameter for Data and MC

$\theta_{i,n}$ – opening angle between the n^{th} ring and the i^{th} PMT directions

$q_{i,n}^{\text{Obs.}}$ – observed charge in i^{th} PMT from n^{th} ring

t_i – residual timing of the i^{th} PMT

L – attenuation length in water

r_i – distance from vertex to the i^{th} PMT

$f(\omega_i)$ – PMT acceptance correction as a function of incidence angle ω_i

S_i – expected amount of p.e.s from scattered photons for the i^{th} PMT

The summation timing window is chosen to exclude spurious decay electrons. From R^n_{TOT} the corresponding ring momentum is found using a correspondence table built from MC. Figure 4.4 shows the correspondence of the two for $e^{\pm}, \mu^{\pm}$ and $K^{\pm}$.

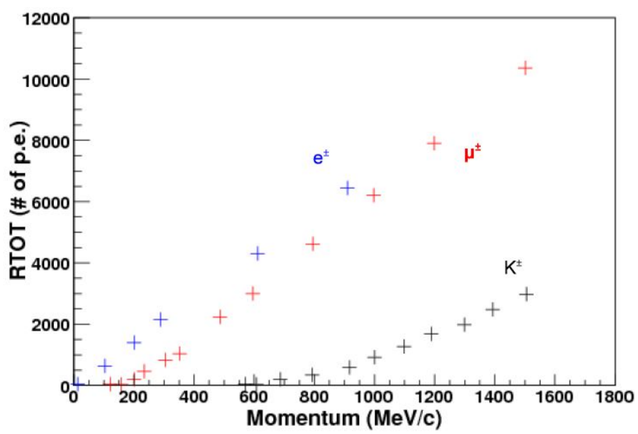

Figure 4.4: RTOT vs. momentum table for the electrons (blue crosses), muons (red crosses) and the kaons (black crosses). From Ref. [239].

The reconstructed momentum resolution for single ring events is estimated to be around $\pm(2.5/\sqrt{P(\text{GeV})} + 0.5)\%$ for the electrons and $\pm 3\%$ for the muons.

4.5 Ring Number Correction

Ring number correction is applied when multiple rings are found. Rings with low momenta and which overlap other visible rings are rejected as "fake rings" (mis-fit).

4.6 Decay Electron Search

The decay electrons are categorized into three sets, those observed in a separate event (sub-event type), those observed with primary event (primary-event type) and those recorded around the end of event timing window (split type). The only ones relevant for our analysis are the primary-event type. They are obtained by the following selection criteria:

1. the time interval to the primary event is $1.2\ \mu\text{s} < \Delta t < 20\ \mu\text{s}$ or $0.1\ \mu\text{s} < \Delta t < 0.8\ \mu\text{s}$
2. number of hit PMTs is > 50
3. vertex is well reconstructed
4. total p.e.s < 2000
5. number of hit PMTs in 50 ns window is > 60
6. number of hit PMTs in 30 ns window is > 40

The last two criteria reject gamma emission from μ^- capture on ^{16}O nuclei. The efficiency for μ^+ is about $\sim 20\%$ higher because it does not capture.

Chapter 5

Fully Contained Data Sample

5.1 FC Reduction

Approximately 10^6 events/day are collected by Super-K. The data relevant for physics studies must be separated from the low-energy radioactivity (e.g. radon) and cosmic ray muon-induced signals. Additionally, "flasher" events, caused by the PMT dynode discharge, further contaminate the data and must be removed. Below, we provide an overview of the automated "data reduction" algorithm for the fully contained (FC) data sample, whose events show activity only within the ID volume. This is the sample relevant for the nucleon decay analyses. Further details of the FC data reduction, as well as the reduction descriptions for the upward-going muon (UPMU) and the partially contained (PC) data samples, can be found in Ref. [160, 240]. Figure 5.1 schematically shows different types of events in SK. For brevity, we focus on SK-I, with other SK periods treated similarly.

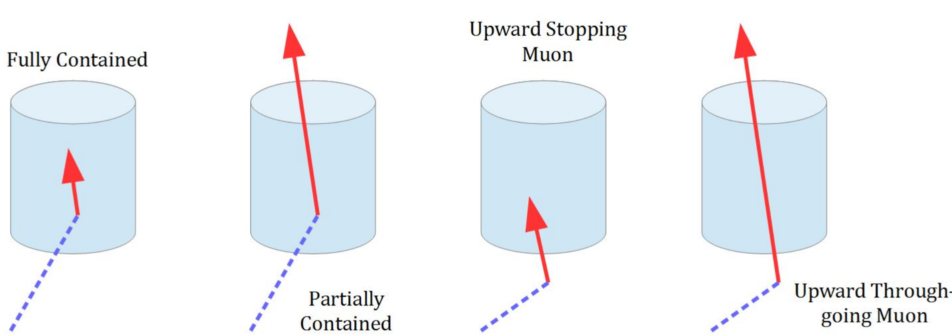

Figure 5.1: Schematic representation of the fully contained, partially contained, upward-going stopping and through-going muon event classes at Super-K.

5.1.1 First and Second Reductions

The selection criteria for the 1^{st} and the 2^{nd} reductions are the following:

1. total ID charge within 300 ns window > 200 p.e. ($\approx$ 22 MeV/c, in case of electron)
2. ratio of (max p.e.s in any ID PMT)/(total number of p.e.s) is < 0.5
3. number of hits in OD within 800 ns window is < 25
4. time interval between events is > 100 μs

Criterion (1) rejects the low energy radioactivity signals, (2) removes the flasher events, (3) ensures that events happen within the ID and (4) rejects the stopping muon decay-electrons.

5.1.2 Third Reduction

The selection criteria for the 3^{rd} reduction is the following:

1. no clusters of > 10 OD PMT hits within 8 m of the detector exit/entrance point of the event
2. number of ID hits in 50 ns residual window is $\geqslant$ 50

This reduction uses reconstruction tools to further reject the radioactivity and the stopping muon-related events.

5.1.3 Fourth Reduction

The 4^{th} reduction focuses on further rejecting spurious events (e.g. flashers), using the following selection criteria:

1. events with very broad timing distribution, typical of flasher events
2. events whose signature has a high correlation match with signal patterns expected from flasher events

5.1.4 Fifth Reduction

The 5^{th} reduction consists of:

1. removal of events with $>$ 10 OD PMT hits in 200 ns preceding the trigger time, rejecting "invisible" cosmic ray muons which are below the Cherenkov threshold but have an observed decay-electron
2. cosmic ray muon removal using a more precise fitter

5.1.5 Final FC Sample

The final reduction consists of selecting events according to:

1. vertex is in the ID fiducial volume (FV), defined as $>$ 2 m away from the wall
2. visible energy ($E_{\text{vis.}}$) $>$ 30 MeV

After the final reduction, data sample contamination from undesired events is $< 1\%$. The estimated efficiency of the reduction for nucleon decay and atmospheric MC is $> 95\%$. The MC detection efficiency is defined as the fraction of events passing the selection criteria compared to the total number of events generated within the true fiducial volume. Table 5.1 summarizes the event rates at each stage of the reduction process for SK-I.

Reduction Step	Data	Atm.-ν MC
Trigger	1269039.1	9.4 (100.00%)
1^{st} Reduction	3083.7	9.4 (99.95%)
2^{st} Reduction	202.7	9.4 (99.94%)
3^{st} Reduction	44.9	9.4 (99.85%)
4^{st} Reduction	18.1	9.3 (99.17%)
5^{st} Reduction	16.1	9.3 (99.15%)
Final Reduction	8.2	9.2 (97.59%)

Table 5.1: Number of events/day after each reduction step for the SK-I FC sample. The atmospheric Monte Carlo numbers and efficiencies down to the fifth reduction are for events whose real vertex is in the fiducial volume, the number of OD hits fewer than 10 and the visible energy larger than 30 MeV. In the last line, the fitted vertex is used for both data and Monte Carlo [160].

5.2 FC Sample Characteristics

The FC data set is made by applying the FC reduction to the data, atmospheric neutrino and nucleon decay MC (see Chapter 3). In Table 5.2, we show the data vs. atmospheric MC reduction summary for the reference SK-I to SK-IV sub-GeV samples (SK-IV here is shown only up to 1294.7 live-days), which are most relevant for our analyses. For the atmospheric MC, 500 years worth of exposure-equivalent are generated for each of the SK periods. Atmospheric MC is normalized by SK livetime for each period. Events are reweighed to take into account the neutrino oscillations and the calculated flux, as described in Chapter 3.

Event Sample	SK-I (1489.2 days)		SK-II (798.6 days)		SK-III (518.1 days)		SK-IV (1294.7 days)	
	Data	MC	Data	MC	Data	MC	Data	MC
FC Total	8608.0	8314.5	4554.0	4473.8	3063.0	2941.8	7318.0	7208.2
sub-GeV e-like	3469.0	3312.6	1856.0	1752.2	1268.0	1171.2	2885.0	2842.3
sub-GeV μ-like	3184.0	3064.7	1684.0	1640.0	1139.0	1090.4	2837.0	2708.8

Table 5.2: Event summary for the reference SK-I to SK-IV single-ring samples.

We display on Figure 5.2 several key distributions for the SK-I to SK-IV FC sub-GeV data samples. Agreement between data and MC is generally observed. The most important distributions for our analysis are the e-like and the μ-like momenta.

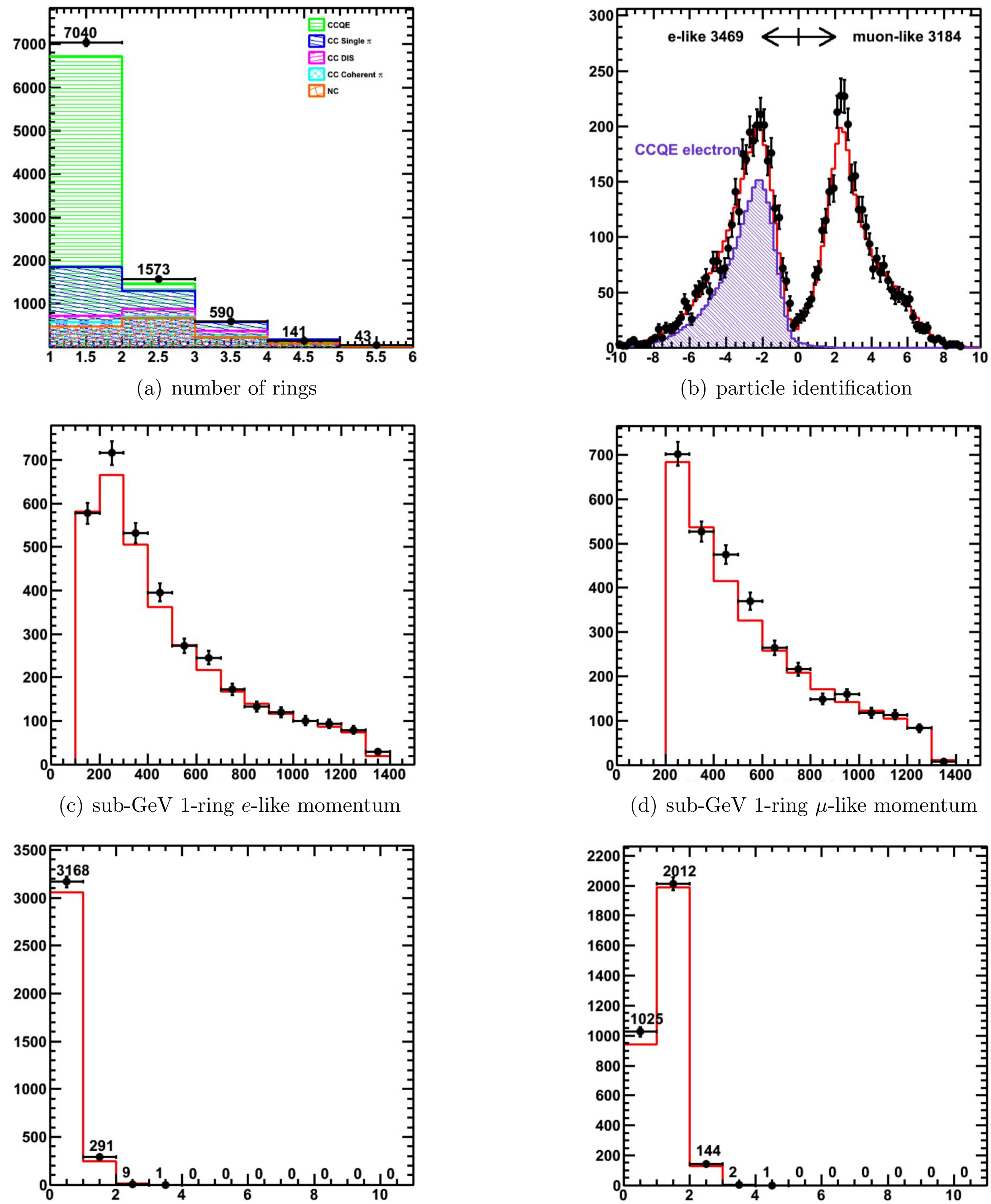

(a) number of rings

(b) particle identification

(c) sub-GeV 1-ring e-like momentum

(d) sub-GeV 1-ring μ-like momentum

(e) sub-GeV 1-ring e-like decay electrons

(f) sub-GeV 1-ring μ-like decay electrons

Figure 5.2: Data vs. atm.-ν MC comparison for the SK-I data set (1489.2 days).

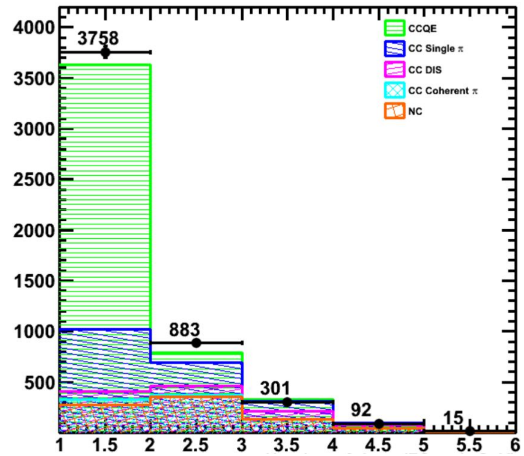

(a) number of rings

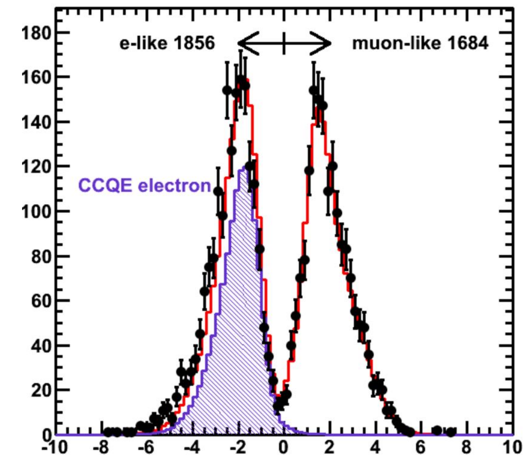

(b) particle identification

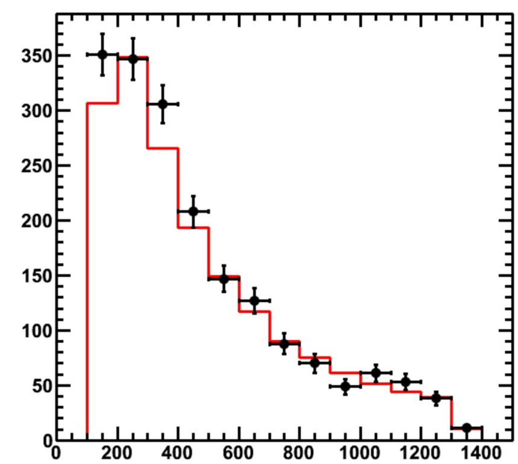

(c) sub-GeV 1-ring e-like momentum

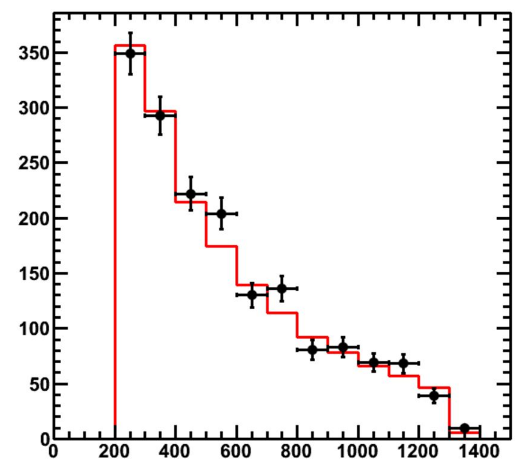

(d) sub-GeV 1-ring μ-like momentum

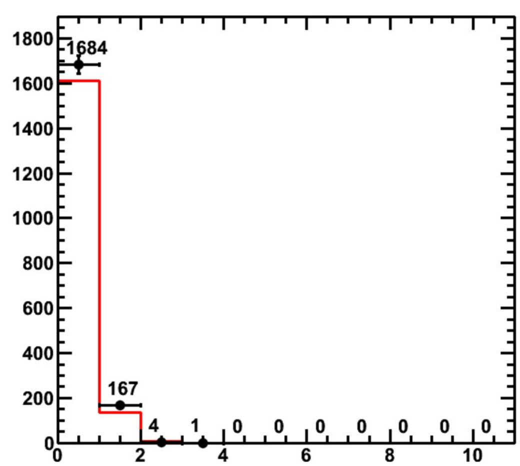

(e) sub-GeV 1-ring e-like decay electrons

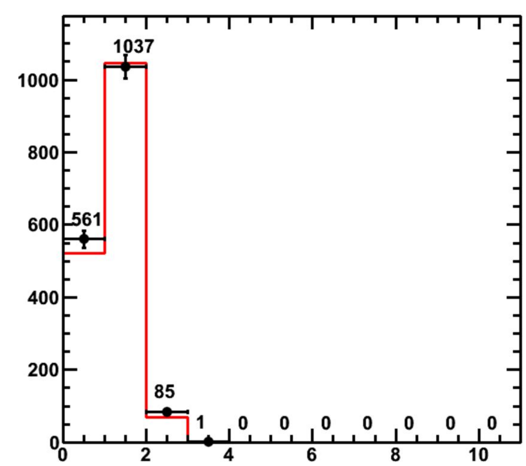

(f) sub-GeV 1-ring μ-like decay electrons

Figure 5.3: Data vs. atm.-ν MC comparison for the SK-II data set (798.6 days).

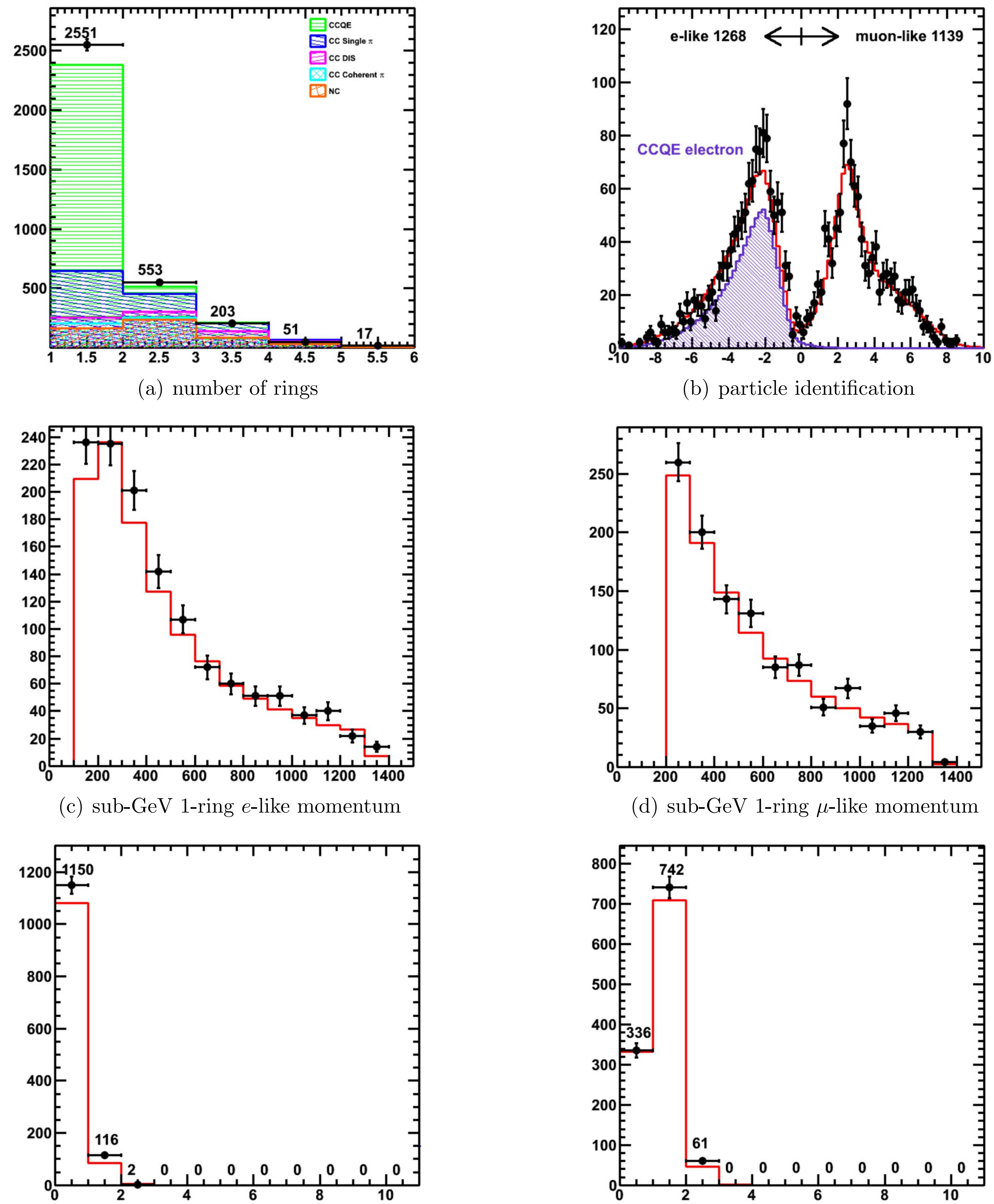

(a) number of rings

(b) particle identification

(c) sub-GeV 1-ring e-like momentum

(d) sub-GeV 1-ring μ-like momentum

(e) sub-GeV 1-ring e-like decay electrons

(f) sub-GeV 1-ring μ-like decay electrons

Figure 5.4: Data vs. atm.-ν MC comparison for the SK-III data set (518.1 days).

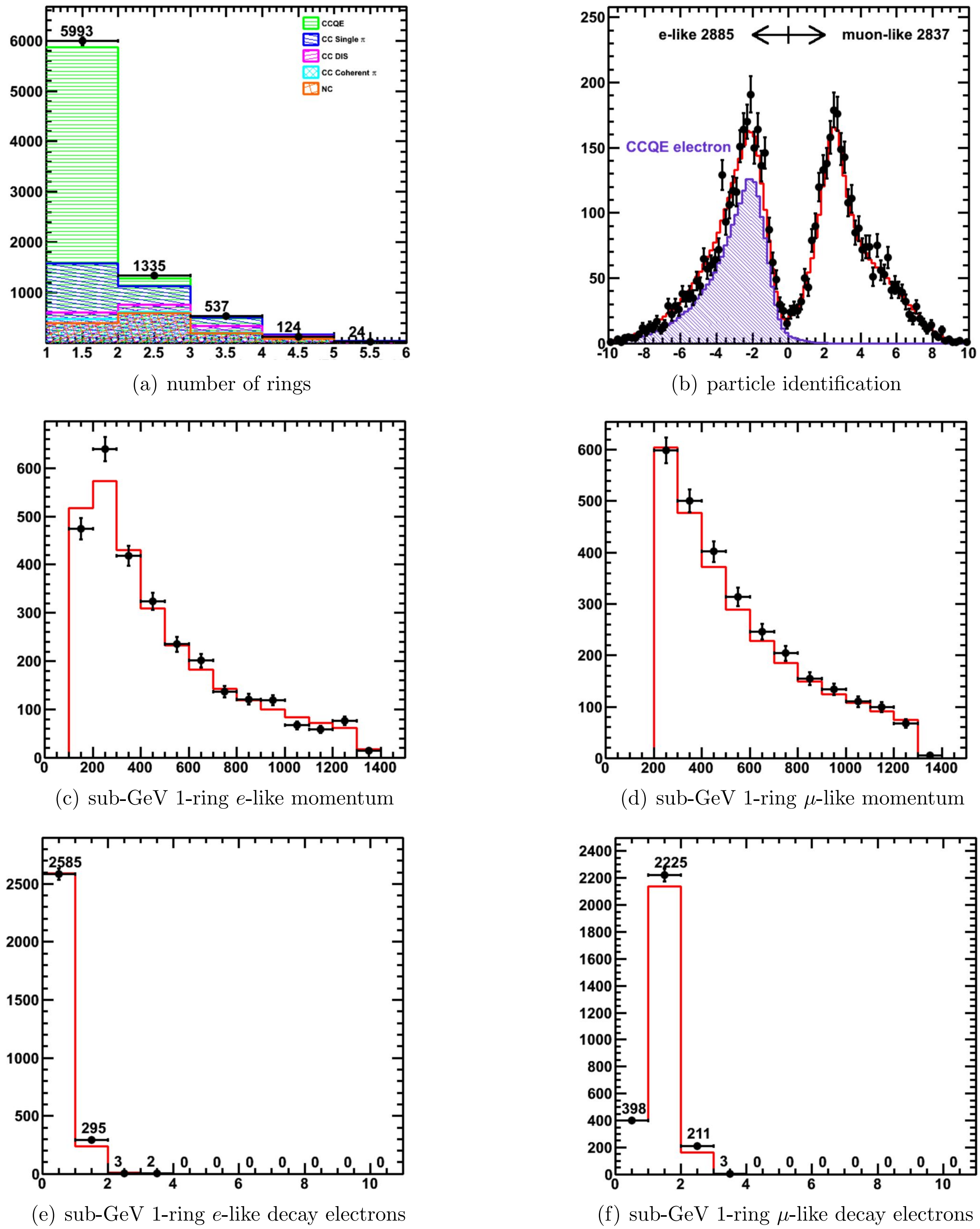

(a) number of rings

(b) particle identification

(c) sub-GeV 1-ring e-like momentum

(d) sub-GeV 1-ring μ-like momentum

(e) sub-GeV 1-ring e-like decay electrons

(f) sub-GeV 1-ring μ-like decay electrons

Figure 5.5: Data vs. atm.-ν MC comparison for the SK-IV data set (1294.7 days).

Chapter 6

Nucleon Decay Analysis

Below we present the analyses for the $p \to e^+X$, $p \to \mu^+X$, $n \to \nu\gamma$, $p \to e^+\nu\nu$, $p \to \mu^+\nu\nu$, $np \to e^+\nu$, $np \to \mu^+\nu$ and $np \to \tau^+\nu$ nucleon decay searches, describing in more detail the published results of Ref. [155] and Ref. [156].

6.1 Data/MC Set

For the analyses, we have employed FC data from the SK-I (1489.2 live-days), SK-II (796.8 live-days), SK-III (518.1 live-days) and SK-IV (1632.3 live-days) Super-K data taking periods, corresponding to a combined exposure of 273.4 kton·years.

The signal and background MC have been generated[1] according to the methods outlined in Chapter 3. For background, we use the same atmospheric-ν MC samples that are used in the SK oscillation analysis [152]. For each SK period, 500 year exposure-equivalent of atmospheric-ν MC is employed. Neutrino oscillations are taken into account by re-weighting the atmospheric-ν MC events[2] (see Chapter 3).

For the nucleon decay signal MC, events were generated 1 m away from the ID wall, which allows to take into account possible event migration across the fiducial volume bound-

[1] Both signal and background MC are simulated using 12p80 version of SKDETSIM (SK detector simulation software) and 11d version of Apfit (SK reconstruction software) for SK-I, SK-II and SK-III. For SK-IV, 13p80 version for SKDETSIM and 15a version for Apfit are used.

[2] The atmospheric MC re-weighting scheme is based on Honda *et. al.* [241] 2006 and Honda *et. al.* [242] 2011 neutrino flux calculations and is different for each SK period.

ary (2 m away from the ID wall). In total, 5,000 signal events ($\sim 4,200$ within FV) were generated for each SK period in the case of single nucleon decay channels, and 10,000 signal events ($\sim 8,400$ within FV) in the case of dinucleon decay channels.

The τ and X are generated according to the procedure outlined in Chapter 3. For the $np \to \tau^+\nu$ analysis only the leptonic τ decay channels $\tau^+ \to e^+\nu\nu$ and $\tau^+ \to \mu^+\nu\nu$ are used, which have the branching ratios of 17.8% and 17.4%, respectively. This allows to treat this channel in a similar manner as the other modes in the spectral fit and thus use a common analysis framework. We have generated in total three different $np \to \tau^+\nu$ MC samples, with τ decaying to $e^+\nu\nu$, $\mu^+\nu\nu$ and with all τ decay channels. The third sample allows us to study contamination from hadronic τ channels in the two selected leptonic channels, which are used in the analysis.

The same FC reduction and reconstruction is applied to both MC and data.

6.2 Preliminaries

6.2.1 Event Selection

After the reduction and reconstruction, event selection is applied to obtain the final analysis sample.

As already mentioned in the introduction, all of the decay modes considered within this analysis contain a neutrino in the final state[3]. Since they are not observable at Super-Kamiokande, one cannot use the final state particles to reconstruct the invariant mass of the parent nucleon(s), which is done, for example, in the $p \to e^+\pi^0$ analysis. The only observables are those related to a single charged lepton (e^+, μ^+) or a γ in the final state. The e^+, μ^+ and γ constitute a single ring signature (showering for γ, e^+ and non-showering for μ^+). Since the muon further decays into an electron, we also account for decay-electrons.

For a single nucleon, a two body decay results in a sharp peak with the energy near $\sim m_n/2$ (free nucleon). Hence, we shall restrict ourselves to the sub-GeV (< 1.33 GeV) analysis sample. The trilepton 3-body decays, $p \to e^+\nu\nu$ and $\tau \to e^+\nu\nu$, have energy spectra that spread out from 0 to $m_n/2$. For the dinucleon decay, the total available invariant mass

[3] Recall that X is generated as a neutrino.

is $\sim 2m_n$, with a peak around m_n in a $2 \to 2$ decay. For dinucleon $np \to \tau^+\nu$ decay, after the $2 \to 2$ decay the τ further decays through trilepton channels, which results in a spread out energy distribution from 0 to $\sim m_\tau/2$. Due to the above considerations, we will enlarge our analysis region to 1500 MeV for the dinucleon decay searches.

For the decay channels $p \to e^+X$, $n \to \nu\gamma$, $np \to e^+\nu$, $np \to \tau^+\nu(\tau^+ \to e^+\nu\nu)$ and $p \to e^+\nu\nu$, the resulting visible energy is from e^+ or γ and thus the observed ring is e-like (showering). The selection criteria for the e-like single nucleon decays is shown in Tabe 6.1. For the dinucleon decay channels, criterion (3) is omitted and (8) is extended to < 1500 MeV/c.

#	Selection	Description
1	evis > 30 and nhitac $\leqslant$ 9[a]	FC
2	wall > 200	within FV, < 2 m away from ID wall
3	evis < 1330	visible energy < 1.33 GeV, sub-GeV
4	nring == 1	1 ring
5	ip[0] == 2	PID is e-like (showering)
6	nmue == 0	0 decay-electrons
7	amome[0] > 100	e-like momentum > 100 MeV/c
8	amome[0] < 1000	e-like momentum < 1000 MeV/c

[a] This is for SK-I, in case of SK-II, SK-III, SK-IV criterion is nhitac $\leqslant$ 15.

Table 6.1: Event selection criteria for nucleon decay channels with one e-like (showering) ring.

Similarly, for the decay channels $p \to \mu^+X$, $np \to \mu^+\nu$, $np \to \tau^+\nu(\tau^+ \to \mu^+\nu\nu)$ the resulting visible energy is from μ^+, producing a μ-like (non-showering) ring, with a decay electron expected to be present. The selection criteria for the μ-like single nucleon decays

#	Selection	Description
1	evis > 30 and nhitac $\leqslant$ 9[a]	FC
2	wall > 200	within FV, < 2 m away from ID wall
3	evis < 1330	visible energy < 1.33 GeV, sub-GeV
4	nring == 1	1 ring
5	ip[0] == 3	PID is μ-like (showering)
6	nmue == 1	1 decay-electron
7	amomm[0] > 200	μ-like momentum > 200 MeV/c
8	amomm[0] < 1000	μ-like momentum < 1000 MeV/c

[a] This is for SK-I, in case of SK-II, SK-III, SK-IV criterion is nhitac $\leqslant$ 15.

Table 6.2: Event selection criteria for nucleon decay channels with one μ-like (non-showering) ring.

is shown in Tabe 6.2. For the dinucleon decay channels, criterion (3) is omitted and (8) is extended to < 1500 MeV/c.

After the event selection, the final single nucleon decay data samples with an e-like ring contain around 8,500 events and 6,000 events for the case of a μ-like ring. The final samples for the dinucleon decays contain around 9,500 events for the e-like channels and 6,500 events for the μ-like ones.

6.2.2 Analysis Momentum Distributions

We can now obtain the final e-like and μ-like momentum distributions that will be used in the spectral χ^2 fit, discussed in the next section. The two representative e-like and μ-like momentum spectra are displayed on Figure 6.1 and Figure 6.2, using $p \to e^+X$ and $p \to \mu^+X$ channels as examples, respectively. The final momentum distributions for the other 6 decay modes can be found in Appendix C. For all our analysis distributions, which serve as input to the fit, we have used 50 MeV momentum binning. Here, the signal has been normalized to the background by area, which in turn is normalized to each SK-period's livetime.

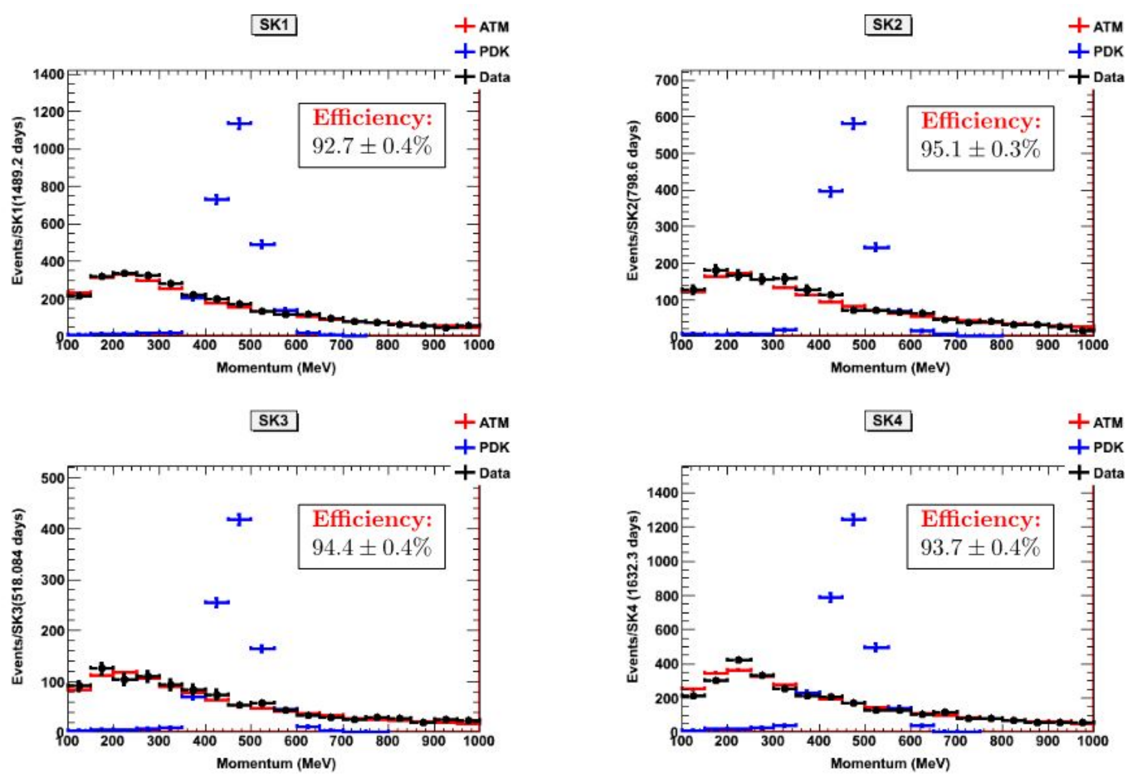

Figure 6.1: Final e-like momentum distributions for $p \to e^+X$.

The signal detection efficiency is defined as before. In Table 6.3 we display the signal detection efficiency for all decay channels. Channels with a μ-like ring have lower overall

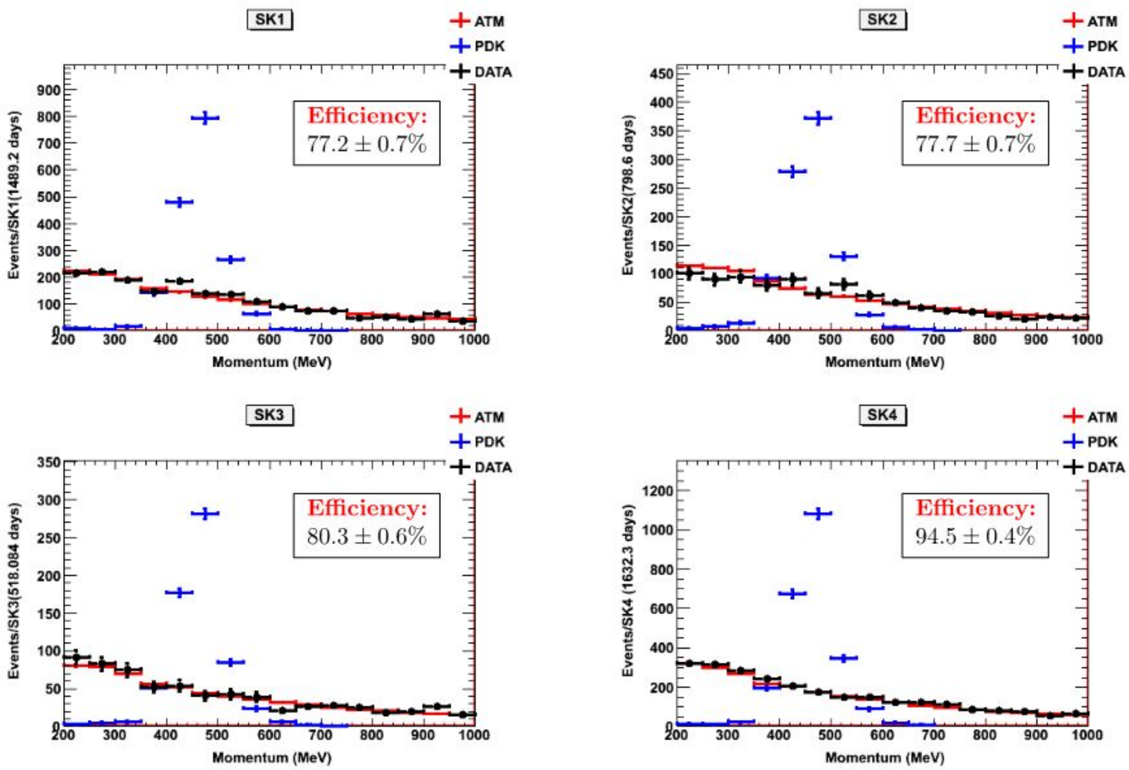

Figure 6.2: Final μ-like momentum distributions for $p \rightarrow \mu^+ X$.

signal efficiency, due to the efficiency of finding the decay-electron of the muon. The increase in efficiency observed in SK-IV for the μ-like channels comes from a 20% improvement in

	Signal Efficiency (%)			
Decay Mode	SK-I	SK-II	SK-III	SK-IV
$p \rightarrow e^+ X$	92.7 ± 0.4	95.1 ± 0.3	94.4 ± 0.4	93.7 ± 0.4
$n \rightarrow \nu\gamma$	93.1 ± 0.4	94.4 ± 0.4	94.3 ± 0.4	93.3 ± 0.4
$p \rightarrow \mu^+ X$	77.2 ± 0.7	77.7 ± 0.7	80.3 ± 0.6	94.5 ± 0.4
$p \rightarrow e^+ \nu\nu$	88.8 ± 0.5	88.0 ± 0.5	89.2 ± 0.5	87.8 ± 0.5
$p \rightarrow \mu^+ \nu\nu$	64.4 ± 0.7	65.0 ± 0.7	67.0 ± 0.7	78.4 ± 0.6
$np \rightarrow e^+ \nu$	93.5 ± 0.3	95.6 ± 0.2	94.2 ± 0.3	94.5 ± 0.3
$np \rightarrow \mu^+ \nu$	73.6 ± 0.5	74.3 ± 0.5	75.6 ± 0.5	89.4 ± 0.3
$np \rightarrow \tau^+(e^+\nu\nu)\nu$	91.9 ± 0.3	96.0 ± 0.3	94.5 ± 0.3	93.5 ± 0.3
$np \rightarrow \tau^+(\mu^+\nu\nu)\nu$	74.6 ± 0.5	76.9 ± 0.5	77.9 ± 0.5	91.2 ± 0.3

Table 6.3: Nucleon decay signal detection efficiency, SK-I through SK-IV.

the decay-electron detection after an upgrade of the SK detector electronics [158]. For the trilepton $p \to e^+\nu\nu$ and $p \to \mu^+\nu\nu$ channels, the average efficiency is slightly lower, due to the spread in the momentum of the charged lepton coming from a 3-body decay combined with a cut at 100 MeV/c for the e-like and 200 MeV/c for the μ-like channels, respectively.

6.2.3 Atmospheric Neutrino Background

On Figure 6.3 and Figure 6.4 we show the remaining atmospheric neutrino background for the e-like and the μ-like single-nucleon decay channels after the event selection, along with the specific contribution of each respective neutrino-interaction channel. This allows us to approximately identify which background systematic errors are expected to be significant.

For the e-like momentum distribution up to 1500 MeV/c, the dominant background contribution, composing about 75.8% of the events, comes from the ν_e charged-current (CC) quasi-elastic (QE) neutrino channel. The ν_e CC single-pion production constitutes around 13.0% of the background, while the ν_e CC coherent-pion, CC multi-pion and neutral-current (NC) single-pion productions contribute around 1.1%, 1.1% and 1.6%, respectively. About 3.5% and 1.1% of events come from ν_μ NC single-pion and coherent-pion production. For the μ-like momentum spectrum up to 1500 MeV/c, the dominant contribution of around 78.6% comes from ν_μ CCQE. Similarly, ν_μ CC single-pion, CC coherent-pion and CC multi-pion as well as NC single-pion production contribute around 16.2%, 1.4%, 1.6% and 0.8%, respectively.

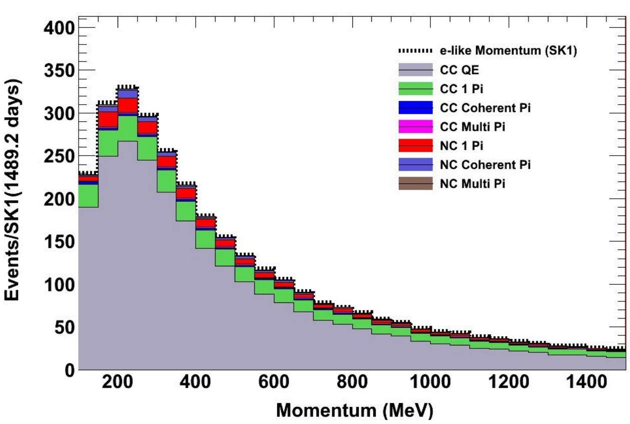

ν-mode	ν_e (%)	ν_μ (%)	$\nu_e + \nu_\mu$ (%)
CC QE	75.83	0.34	76.17
CC 1-π	13.07	0.30	13.37
CC coh.-π	1.13	0.01	1.14
CC multi-π	1.09	0.07	1.16
NC 1-π	1.55	3.53	5.08
NC coh.-π	0.49	1.07	1.56
NC multi-π	0.21	0.51	0.72
Total	93.37	5.83	99.20

Figure 6.3: Contribution of individual atmospheric ν-channels to the background of the e-like analysis spectra, normalized to SK-I livetime of 1489.2 days.

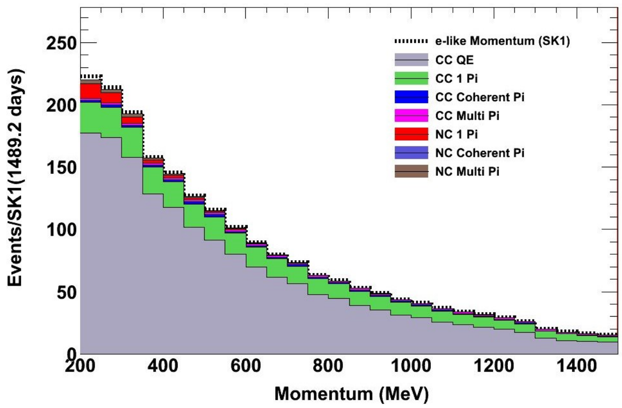

ν-mode	ν_e (%)	ν_μ (%)	$\nu_e + \nu_\mu$ (%)
CC QE	0.00	78.64	78.64
CC 1-π	0.05	16.23	16.28
CC coh.-π	0.01	1.40	1.40
CC multi-π	0.00	1.60	1.60
NC 1-π	0.37	0.81	1.19
NC coh.-π	0.00	0.00	0.00
NC multi-π	0.14	0.31	0.45
Total	0.57	98.99	99.56

Figure 6.4: Contribution of the individual atmospheric ν-channels to the background of the μ-like analysis spectra, normalized to SK-I livetime of 1489.2 days.

6.3 Spectral Fit

We now apply a spectral χ^2 fit to the obtained final momentum distributions[4], allowing us to take into account the information coming from the shape difference between the signal and the background distributions.

6.3.1 Fitting Technique

The χ^2 minimization fit is based on the Poisson distribution, with the systematic uncertainties accounted for by quadratic penalties ("pull terms") [154]. The χ^2 function used in the analysis is

$$\begin{aligned} \chi^2 = & \; 2\sum_{i=1}^{\text{nbins}} \Big(N_i^{\text{exp}} + N_i^{\text{obs}} \Big[\ln \frac{N_i^{\text{obs}}}{N_i^{\text{exp}}} - 1 \Big] \Big) + \sum_{j=1}^{N_{\text{syserr}}} (\frac{\epsilon_j}{\sigma_j})^2 \\ N_i^{\text{exp}} = & \Big[\alpha \cdot N_i^{\text{back}} + \beta \cdot N_i^{\text{sig}} \Big] (1 + \sum_{j=1}^{N_{\text{syserr}}} f_i^j \frac{\epsilon_j}{\sigma_j}) \; , \end{aligned} \tag{6.1}$$

where i labels the analysis bin. The terms N_i^{obs}, N_i^{sig}, N_i^{back}, N_i^{exp} are the numbers of observed data, signal MC, background MC and the total (signal and background) MC events in each

[4] In this analysis, as in other SK searches, a custom SK software algorithm (Osc3++) which performs the spectral fit is used.

bin i. The index j labels the systematic errors, while ϵ_j and f_i^j correspond to the fit error parameter and the fractional change in the N_i^{exp} bin due to 1-sigma error uncertainty σ_j, respectively. The fit is performed for two parameters α and β, which denote the background and signal normalizations, respectively. After the event selection, the signal MC distribution is normalized to the background by the integral, which in turn is normalized to the SK livetime. This allows us to identify the fit point $(\alpha, \beta) = (1, 0)$ with the no-signal hypothesis. Similarly, $(\alpha, \beta) = (0, 1)$ signifies that the data is described by signal only, with the signal amount equal to background MC normalized (pre-fit) to livetime. The χ^2 minimization is carried out over each α and β in the grid according to $\partial\chi^2/\partial\epsilon_j = 0$. The resulting global minimum is defined as the best fit. For the $np \to \tau^+\nu\nu$ mode, after the appropriate event selection is applied to both MC samples of $\tau \to e^+\nu\nu$ and $\tau \to \mu^+\nu\nu$, the samples are combined for the fit, allowing us to obtain a single value for the permitted number of nucleon decays at 90% CL. Further details regarding the fit and the treatment of systematic errors can be found in Ref. [152, 153], where this technique is applied to the standard SK oscillation analysis and the indirect dark matter search. This analysis technique was also applied to the $n \to \nu\pi^0$ and $p \to \nu\pi^+$ [243] nucleon decay searches.

6.3.2 Systematic Errors

The systematic errors in the analysis are considered within the fit through the f_i^j coefficients, as described above. For simplicity, it is assumed that the errors affect linearly the bin content N_i^0 of the analysis bin i. Then, the f_i^j can be defined as a slope of the line between the bin i content changed by $\pm\sigma$ of the systematic error, which can be expressed as

$$f_i^j \equiv \frac{\left(N_i^{+\sigma_j} - Nt_i^{-\sigma_j}\right)}{2N_i^0} . \tag{6.2}$$

For the error estimation in our analysis, unlike Ref. [154], the signal and error bins are split. This ensures that signal systematic is applied to the signal bins and background systematic to the background bins, while a common systematic (such as energy calibration) is applied to both. The two are then merged together for the χ^2 minimization.

The systematics can be divided into signal specific (S), background-specific (B) as well as detector and reconstruction errors, which are common to both signal and background (SB). The two signal specific systematics are from Fermi motion and nucleon-nucleon correlated decay. For background, many systematics, such as the neutrino flux normalization or the neutrino-interaction cross-section uncertainty, can contribute. In order to methodically select the dominant systematics, we started from more than 150 errors employed in the SK oscillation analysis [152] and chose those which affect the e-like and μ-like spectra analyses bins by more than 5% (i.e. $|f_i^j > 0.05|$). Relaxing this criteria to 1% does not significantly alter the results, but complicates the analysis [155]. Some of the most dominant contributions originate from the uncertainties related to the neutrino flux and the energy calibration (common to both signal and background). Including the two signal systematics, a total of 11 errors are considered and they are the same for all channels. In Table 6.4 we display the complete list of systematics, their uncertainties and the fitted pull terms for the two representative decay channels, $p \to e^+X$ and $p \to \mu^+X$.

Decay mode		$p \to e^+X$	$p \to \mu^+X$	
Systematic error	1-σ uncertainty (%)	Fit pull (σ)	Fit pull (σ)	
Final state interactions (FSI)	10	0.10	-0.60	B
Flux normalization ($E_\nu < 1$ GeV)	25 [a]	-0.23	-0.08	B
Flux normalization ($E_\nu > 1$ GeV)	15 [b]	-1.44	-0.50	B
M_A in ν interactions	10	0.69	0.23	B
Single meson cross-section in ν interactions	10	-0.55	-0.14	B
Energy calibration of SK-I	1.1	0.58	-0.54	SB
Energy calibration of SK-II	1.7	-0.91	-0.07	SB
Energy calibration of SK-III	2.7	0.48	0.26	SB
Energy calibration of SK-IV	2.3	0.38	-0.14	SB
Fermi model comparison	10 [c]	-0.08	0.70	S
Nucleon-nucleon correlated decay	100	0.00	0.06	S

[a] Uncertainty linearly decreases with log E_ν from 25% (0.1 GeV) to 7% (1 GeV).
[b] Uncertainty is 7% up to 10 GeV, linearly increases with log E_ν from 7% (10 GeV) to 12% (100 GeV) and then 20% (1 TeV).
[c] Estimated from comparison of spectral function and Fermi gas model.

Table 6.4: Systematic errors of the two representative spectral fits, with 1σ uncertainties and resulting fit pull terms. Errors specific to signal and background are denoted by S and B, while those that are common to both are denoted by SB.

To illustrate the above approach, we describe in more detail how some of the systematics are estimated. For the correlated decay, there is an additional (wave-function correlated) nucleon in the final state (see Chapter 3). Assuming an uncertainty of σ_{corr} = 100%, the number of such events in the final sample is reweighed by a factor of 2 or 0 (corresponding to $\pm\ \sigma_{corr}$ = 100%) and then the event rate change in the e-like and the μ-like analysis bins provides the respective f_i^j.

For the case of Fermi momentum, the error estimation is related to the Fermi momentum model comparison between the signal (uses spectral function) and the background (uses

Fermi gas model), as described in Chapter 3. As an example, we display in Figure 6.5 the Fermi momentum distributions for both signal and background using the $p \rightarrow \mu^+ X$ SK-I sample. This error is estimated by re-weighting every 5 MeV Fermi momentum signal bin to

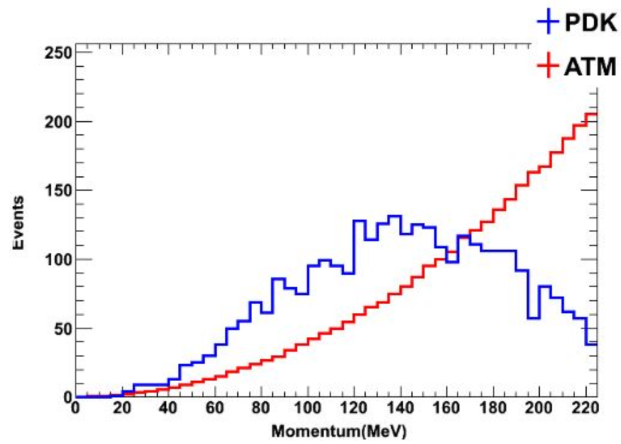

Figure 6.5: Fermi momentum signal (spectral function) and background (relativistic Fermi gas) model comparison for $p \rightarrow \mu^+ X$, using SK-I sample.

match the shape of the background Fermi momentum distribution. Then, we compare the final resulting e-like (or μ-like) analysis spectra, with the bin rates given by $N_i^{old\ model}$ and $N_i^{new\ model}$, respectively. The f_i^j are then estimated via

$$f_i^j \equiv \frac{\left(N_i^{new\ model} - N_i^{old\ model}\right)}{N_i^{old\ model}}, \tag{6.3}$$

where both distributions have been normalized by area.

For energy calibration, which is a common systematic error for both signal and background, we just shift the final energy spectra by $\pm\sigma$ of the energy calibration uncertainty (within 3%) to obtain the new event count in each bin for the f_i^j calculation.

The background systematics are treated similarly. For more details see the SK oscillation analysis [194, 244]. For example, the f_i^j for the uncertainty in meson interaction cross-section is found by generating MC samples with reweighed cross-sections by $\pm\sigma$ and then studying the shifts in the final analysis bins in the manner described above.

In our analysis the systematic errors due to reconstruction (ring counting, PID, etc.) are negligible and are thus omitted.

6.4 Fit Results and Lifetime Calculation

The spectral fit determines the overall background and signal normalizations α and β. The sensitivity reach and lower lifetime limit on the process (in case no excess is observed), can then be computed from the 90% confidence level value of β ($\beta_{90\mathrm{CL}}$), which translates into the allowed amount of signal at 90% confidence level according to $N_{90\mathrm{CL}} = \beta_{90\mathrm{CL}} \times N^{\mathrm{signal}}$, where N^{signal} is the total number of signal events. The partial lifetime limit is then calculated from

$$\tau_{90\mathrm{CL}}/\mathcal{B} \;=\; \frac{\sum_{\mathrm{sk=SK1}}^{\mathrm{SK4}} \lambda_{\mathrm{sk}} \times \epsilon_{\mathrm{sk}} \times N^{\mathrm{nucleons}}}{N_{90\mathrm{CL}}}\,, \tag{6.4}$$

where $\mathcal{B}$ is the branching ratio of a process, ϵ_{sk} and λ_{sk} are the signal efficiency and the exposure in kton·years for each SK phase, $N_{90\mathrm{CL}}$ is the amount of signal allowed at the 90% confidence level and N^{nucleons} is the number of nucleons per kiloton of water, corresponding to 3.3×10^{32}, 2.7×10^{32} and 3.3×10^{31} for the proton, the neutron and the dinucleon decay searches, respectively.

To calculate the MC sensitivity, we use atmospheric MC as "fake data". This corresponds to the scenario where no excess is observed in the data, which follows the background distribution. Hence, in this case, the normalizations of background and signal are $\alpha = 1$ and $\beta = 0$, for background normalized to the SK-period's livetime. As an example of the χ^2 contour output, we display the sensitivity fit results for $p \to e^+X$ on Figure 6.6. In the χ^2

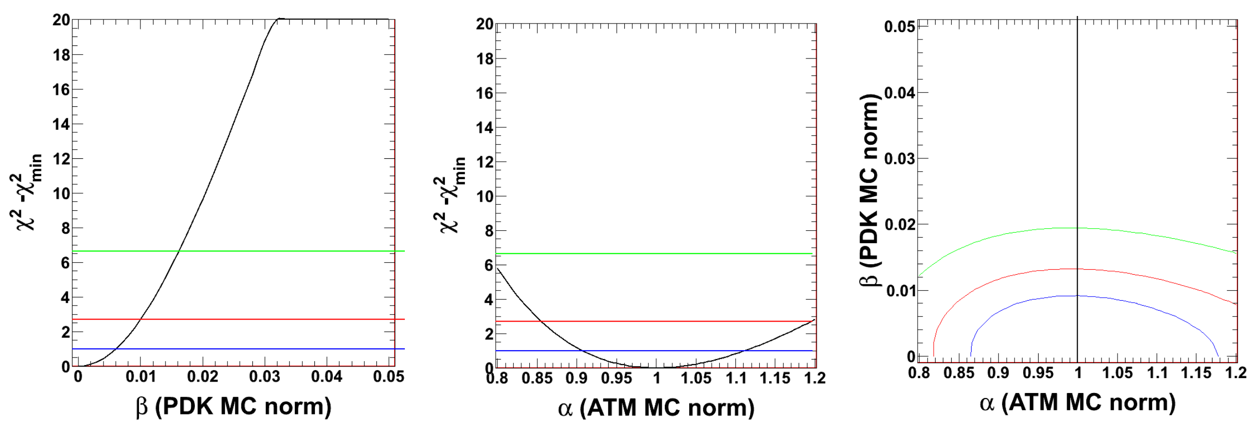

Figure 6.6: MC sensitivity fit for $p \to e^+X$, resulting in $\beta_{90CL} = 0.013$ (at $\alpha = 1$) [right].

contour plots, the red, blue and yellow lines correspond to 68%, 90% and 95% confidence level (C.L.) intervals, respectively. The sensitivity is obtained by finding the β_{90CL} (red curve) at the point of $\alpha = 1$ (right plot, α vs. β). In the given case, this value is $\beta_{90CL} = 0.013$, which corresponds to $N_{90CL} = 108$. Taking into account the signal efficiency (see Table 6.3), N_{90CL}

and the live-time for each of the SK phases, one obtains the $p \rightarrow e^+X$ MC sensitivity reach of 7.9×10^{32} years.

Proceeding similarly with the real data, we obtain χ^2 distributions as shown on Figure 6.7. Here, the β_{90CL} is obtained from the left figure above (χ^2 vs. β) at the intersection

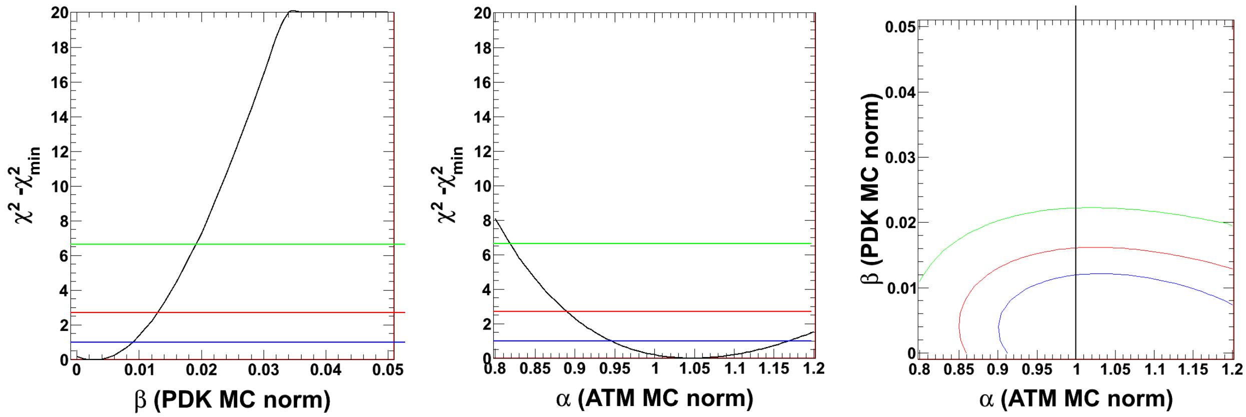

Figure 6.7: Data fit for $p \rightarrow e^+X$, resulting in $\beta_{90CL} = 0.013$ [left].

with the red curve (the 90% CL interval). This corresponds to profiling out α as a nuisance parameter. In our case, the β_{90CL} happens to be 0.013 and the best fit point corresponds to $(\alpha, \beta) = (1.05, 0.002)$. The similarity of the results between the sensitivity and the data fits signify that data is described well by the background. Additionally, $\chi^2/$ d.o.f. $= 70.9/70 \approx 1$, as expected for a properly performed fit. For the data fit $\Delta\chi^2 = \chi^2 - \chi^2_{min}$ is 0.19 and is within 1σ of the background-only hypothesis. Hence, we establish that no significant excess is observed and we proceed to calculate the lower lifetime limit on the process, which for $p \rightarrow e^+X$ is found to be $7.9 \cdot 10^{32}$ years at 90% CL.

We summarize the sensitivity and the data fit results for all 8 channels in Table 6.5. The χ^2 fit contours for other modes can be found in Appendix C.2. The results reported for dinucleon decay channels are per ^{16}O nucleus[5]. For the $np \rightarrow \tau\nu$ mode we have combined the τ decay channels $\tau \rightarrow e^+\nu\nu$ and $\tau \rightarrow \mu^+\nu\nu$, weighted by their respective branching ratios. This limit is then multiplied by 1.15 to account for roughly 85% sample purity of the tau channels. All of the fits have χ^2/d.o.f. ≈ 1, which is expected for correctly executed fits. The fit outcomes show that $\Delta\chi^2$ is within 1σ level of the background only hypothesis for all channels, aside $p \rightarrow \mu^+X$, which is within 2σ. Overall, we conclude that no significant excess has been observed in any of the studied channels.

To visualize the analysis results, we have shown the the fitted spectra for the 273.4

[5] This is consistent with other experiments (e.g. Frejus dinucleon results are reported per iron nucleus).

Decay mode	Best fit (α, β)	Best fit χ^2/d.o.f.	No signal $\Delta\chi^2$	Data $\beta_{90\mathrm{CL}}$	Data $N_{90\mathrm{CL}}$	Sensitivity ($\times 10^{31}$ yr.)	$\tau/\mathcal{B}$ ($\times 10^{31}$ yr.)
$p \to e^+ X$	(1.050, 0.002)	70.9/70	0.19	0.013	108	79	79
$n \to \nu\gamma$	(1.045, 0.004)	70.5/70	0.43	0.015	125	58	55
$p \to \mu^+ X$	(0.960, 0.016)	63.2/62	3.43	0.032	187	77	41
$p \to e^+ \nu\nu$	(1.050, 0.030)	65.6/70	1.50	0.060	459	27	17
$p \to \mu^+ \nu\nu$	(0.990, 0.020)	66.1/62	0.50	0.050	286	25	22
$np \to e^+ \nu$	(0.955, 0.000)	122.5/110	0.00	0.004	33	10	26
$np \to \mu^+ \nu$	(0.910, 0.000)	97.0/102	0.00	0.005	36	11	20
$np \to \tau^+ \nu$	(0.910, 0.000)	224.6/214	0.00	0.006	96	1	3

Table 6.5: Best fit (α, β) parameter values, best fit χ^2/ d.o.f., no signal $\Delta\chi^2$, 90% C.L. value of β parameter, allowed number of nucleon decay events in the full 273.4 kton·years exposure and a partial lifetime limit for each decay mode at 90% C.L. The sensitivity and lifetime limit for dinucleon decay modes are per ^{16}O nucleus.

kton·years of combined SK data in Figure 6.8. The upper figures display best-fit result for atmospheric neutrino background (solid line) without signal fitted to data (black dots) and the corresponding residuals after the fitted MC is subtracted from data. It is seen that the background MC describes the data well. The bottom figures display the 90% C.L. allowed signal multiplied by 10 (hatched histogram), obtained from the fit of background with signal to data, with all the e-like and μ-like spectra overlaid for all the modes.

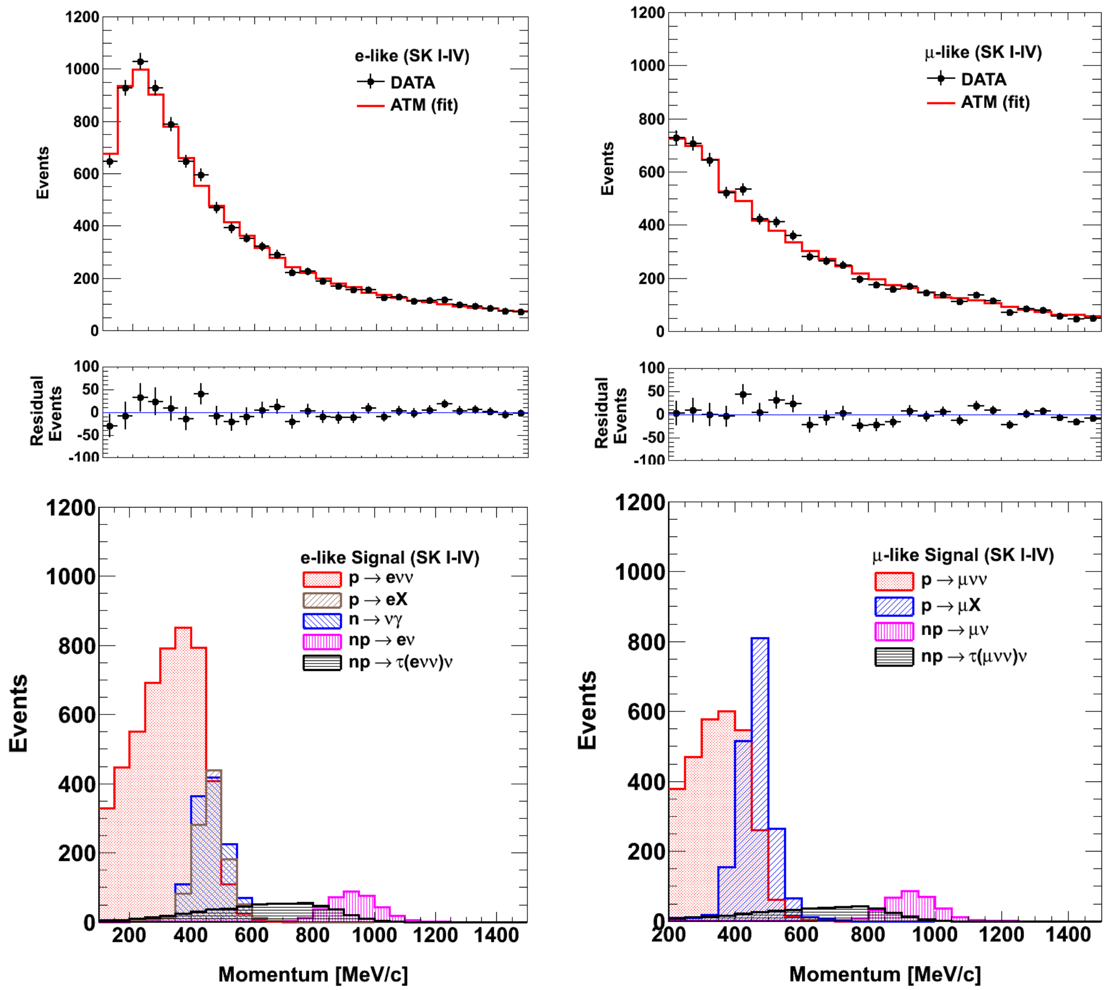

Figure 6.8: [top] Reconstructed momentum distribution for 273.4 kton·years of combined SK data (black dots) and the best-fit result for the atmospheric neutrino background Monte Carlo (solid line). The corresponding residuals are shown below, after fitted background subtraction from data. [bottom] The 90% confidence level allowed nucleon decay signal multiplied by 10 (hatched histograms), from the signal and background MC fit to data. All modes are shown (overlaid), with e-like channels on the left and μ-like channels on the right.

Chapter 7

Summary and Future Prospects

While baryon number violation is expected from theoretical considerations in various contexts (see Chapter 1), it remains to be seen experimentally. In this Thesis, we have described searches for eight exotic baryon-number violating processes using 273.4 kton·years of combined data from the Super-Kamiokande large underground water Cherenkov experiment. All of the searched channels produce single ring showering or non-showering signatures, which are well described by atmospheric neutrinos, within the detector. We have studied the single Cherenkov ring momentum spectra, including the effect of neutrino oscillation and systematic uncertainties, up to 1500 MeV/c. No significant excess of signal over background has been observed in the data, allowing us to set the following lower lifetime limits on the processes, as shown in Table 7.1.

Decay mode	Sensitivity ($\times 10^{31}$ yr.)	$\tau/\mathcal{B}$ ($\times 10^{31}$ yr.)	Previous $\tau/\mathcal{B}$ ($\times 10^{31}$ yr.)
$p \to e^+ X$	79	79	-
$n \to \nu\gamma$	58	55	2.8 [131]
$p \to \mu^+ X$	77	41	-
$p \to e^+ \nu\nu$	27	17	1.7 [131]
$p \to \mu^+ \nu\nu$	25	22	2.1 [138]
$np \to e^+ \nu$	10	26	0.3 [138]
$np \to \mu^+ \nu$	11	20	0.2 [138]
$np \to \tau^+ \nu$	1	3	-

Table 7.1: Final analysis results (sensitivity and lifetime limits) for the eight studied nucleon decay modes. Comparison to previous experimental results is shown. The results for dinucleon channels are reported per nucleus.

The obtained lifetime limits for the trilepton decay channels $p \to e^+\nu\nu$ and $p \to \mu^+\nu\nu$

are an order of magnitude improvement over the previous searches, conducted by IMB [131] and Frejus [138]. These results provide strong constraints to both the permitted parameter space of models presented in Refs. [135, 139], which predict lifetimes of around $10^{30} - 10^{33}$ years, and the other GUT models that allow for similar processes. The analyses for these channels presented in this work are only weakly model dependent, due to the assumption of a flat phase space in the signal generation. However, this assumption agrees well with alternative phase space considerations [157] (see Appendix B) in the context of vector- or scalar-mediated proton decays, which are typical of GUT models [49, 54, 137]. The obtained limits on the other six channels represent more than an order of magnitude improvement over the previous analyses of $n \to \nu\gamma$ at IMB [131] and two orders of magnitude for the $np \to e^+\nu$ and $np \to \mu^+\nu$ searches at Frejus [138]. The searches for $p \to e^+X$, $p \to \mu^+X$ (where X is an invisible, massless particle) and $np \to \tau^+\nu$ are novel. The results of all of the above analyses provide a stringent test of new physics. The dinucleon decay limits restrict $\Delta B = 2$ processes with L violated by either zero or two units.

In the future, the proposed Hyper-Kamiokande [245] large underground water Cherenkov experiment with a half-megaton fiducial volume (20 times that of Super-K) is expected to allow for a factor of $\sim 5 - 10$[1] improvement in the lifetime reach over the SK results within a $\sim$ 10 year running period. Additionally, the proposed 40 kiloton underground liquid argon TPC (LArTPC) experiment DUNE/LBNF [246] is expected to also improve the nucleon decay studies. The LArTPC technology will allow to see kaons, which are below threshold at the water Cherenkov experiments for the $p \to \nu K^+$ decays.

[1] Rough sensitivity estimates have been calculated by the author.

Bibliography

[1] H. Weyl, *Z. Phys.* **56**, 330 (1929)

[2] C.D. Anderson, *Phys. Rev.* **43**, 491 (1933)

[3] E.C.G. Stueckelberg, *Helv. Phys. Acta* **11**, 299 (1938)

[4] E.P. Wigner, *Am. Phil. Soc.* **93**, 521 (1949)

[5] A.D. Sakharov, *Pisma Zh. Eksp. Teor. Fiz.* **5**, 32 (1967)

[6] L. Canetti, M. Drewe and M. Shaposhnikov, *New J. Phys.* **14**, 095012 (2012), arXiv:1204.4186 [hep-ph]

[7] V.A. Kuzmin, V.A. Rubakov and M.E. Shaposhnikov, *Phys. Lett.* **B155**, 36 (1985)

[8] R. Mohapatra, *Unification and Supersymmetry: The Frontiers of Quark-Lepton Physics*, Springer (2012)

[9] T. Banks and N. Seiberg, *Phys. Rev.* **D83**, 084019 (2011), arXiv:1011.5120 [hep-th]

[10] F.C. Adams and G. Laughlin, *Rev. Mod. Phys.* **69**, 337 (1997), arXiv:astro-ph/9701131

[11] K.S. Babu *et. al.*, *Snowmass 2013 Intensity Frontier Report* (2013), arXiv:1310.6677 [hep-ph]

[12] W. Pauli, *Rev. Mod. Phys.* **13**, 203 (1941)

[13] J.S. Schwinger, *Phys. Rev.* **82**, 914 (1951)

[14] E. Noether, *Gott. Nachr.* **1918**, 235 (1918), arXiv:physics/0503066

[15] T.D. Lee and C.N. Yang, *Phys. Rev.* **104**, 254 (1956)

[16] J.H. Christenson *et. al.*, *Phys. Rev. Lett.* **13**, 138 (1964)

[17] Y. Fukuda *et. al.* (Super-Kamiokande Collaboration), *Phys. Rev. Lett.* **81**, 1562 (1998), arXiv:hep-ex/9807003

[18] Q.R. Ahmad *et. al.* (SNO Collaboration), *Phys. Rev. Lett.* **87**, 071301 (2001)

[19] J.P. Lees *et. al.* (BaBar Collaboration), *Phys. Rev. Lett.* **109**, 211801 (2012) arXiv:1207.5832 [hep-ex]

[20] E. Majorana, *Nuovo Cim.* **14**, 171 (1937)

[21] J.D. Vergados, H. Ejiri and F. Simkovic, *Rept. Prog. Phys.* **75**, 106301 (2012), arXiv:1205.0649 [hep-ph]

[22] Y. Fukuda *et. al.* (Super-Kamiokande Collaboration), *Nucl. Instrum. Meth.* **A501**, 418 (2003)

[23] P. Langacker, *The Standard Model and Beyond*, CRC Press (2009)

[24] S.L. Glashow, *Nucl. Phys.* **22**, 579 (1961)

[25] S. Weinberg, *Phys. Rev. Lett.* **19**, 1264 (1967)

[26] A. Salam, *Conf. Proc.* **C680519**, 367 (1968)

[27] H.D. Politzer, *Phys. Rev. Lett.* **30**, 1346 (1973)

[28] D.J. Gross and F. Wilczek, *Phys. Rev. Lett.* **30**, 1343 (1973)

[29] N. Cabibbo, *Phys. Rev. Lett.* **10**, 531 (1963)

[30] M. Kobayashi and T. Maskawa, *Prog. Theor. Phys.* **49**, 652 (1973)

[31] B. Pontecorvo, *Sov. Phys. JETP* **6**, 429 (1957)

[32] B. Pontecorvo, *Sov. Phys. JETP* **26**, 984 (1968)

[33] Z. Maki, M. Nakagawa and S. Sakata, *Prog. Theor. Phys.* **28**, 870 (1962)

[34] F. Englert and R. Brout, *Phys. Rev. Lett.* **13**, 321 (1964)

[35] G.S. Guralnik, C.R. Hagen and T.W.B. Kibble, *Phys. Rev. Lett.* **13**, 585 (1964)

[36] P.W. Anderson, *Phys. Rev.* **130**, 439 (1963)

[37] K.A. Olive *et. al.* (Particle Data Group), *Chin. Phys.* **C38**, 090001 (2014)

[38] J.S. Bell and R. Jackiw, *Nuovo Cim.* **A60**, 47 (1969)

[39] S.L. Adler, *Phys. Rev.* **177**, 2426 (1969)

[40] J. Steinberger, *Phys. Rev.* **76**, 1180 (1949)

[41] P.F. Perez and M. Wise, *Phys. Rev.* **D82**, 011901 (2010), arXiv:100.1754 [hep-ph]

[42] A.A. Belavin *et. al.*, *Phys. Lett.* **B59**, 85 (1975)

[43] N.S. Manton, *Phys. Rev.* **D28**, 2019 (1983)

[44] G. t' Hooft, *Phys. Rev. Lett.* **37**, 8 (1976)

[45] P.B. Arnold and L.D. McLerran, *Phys. Rev.* **D37**, 1020 (1988)

[46] M. Dine *et. al.*, *Nucl. Phys.* **B342**, 381 (1990)

[47] S. Coleman, *Aspects of Symmetry*, Cambridge University Press (1989)

[48] M. Dine, *Proc. 18th SLAC Inst. Part. Phys.* (1990)

[49] H. Georgi and S.L. Glashow, *Phys. Rev. Lett.* **32**, 438 (1974)

[50] J.C. Pati and A. Salam, *Phys. Rev.* **D8**, 1240 (1973)

[51] E. Golowich, *Phys. Rev.* **D24**, 2899 (1981)

[52] S. Dimopoulos and F. Wilczek, *Proc. Eric Sum. Sch.* (1981)

[53] P. Langacker and N. Polonsky, *Phys. Rev.* **D47**, 4028 (1993), arXiv:hep-ph/9210235

[54] H. Fritzsch and P. Minkowski, *Annals Phys.* **93**, 193 (1975)

[55] S.M. Barr, *Phys. Lett.* **B112**, 219 (1982)

[56] J.R. Ellis, D.V. Nanopoulos and J. Walker, *Phys. Lett.* **B550**, 99 (2002), arXiv:hep-

ph/0205336
[57] P. Minkowski, *Phys. Lett.* **B67**, 421 (1977)
[58] M. Gell-Mann, P. Ramond and R. Slansky, *Proceedings to Supergravity Workshop* (1979)
[59] T. Yanagida, *Prog. Theor. Phys.* **64**, 1103 (1980)
[60] R.N. Mohapatra and G. Senjanovic, *Phys. Rev. Lett.* **44**, 912 (1980)
[61] J. Schechter and J.W.F. Valle, *Phys. Rev.* **D22**, 2227 (1980)
[62] G. Altarelli and F. Feruglio, *Rev. Mod. Phys.* **82**, 2701 (2010)
[63] R.N. Mohapatra and M.K. Parida, *Phys. Rev.* **D47**, 264 (1993), hep-ph/9204234
[64] D.I. Kazakov, *Proc. of Eu. School of High En. Phys. 2000* (2000), arXiv:hep-ph/001228
[65] S.P. Martin, *Adv. Ser. Direct. High Energy Phys.* **18**, 1 (1998), arXiv:hep-ph/9709356
[66] R. Haag, J.T. Lopuszanski and M. Sohnius, *Nucl. Phys.* **B88**, 257 (1975)
[67] S. Chatrchyan *et. al.* (CMS Collaboration), *Phys. Rev.* **D88**, 0520217 (2013)
[68] G. Aad *et. al.* (ATLAS Collaboration), *Phys. Rev. Lett.* **106**, 131802 (2011), arXiv:1102.2357 [hep-ex]
[69] L.B. Anderson, J. Gray and A. Lukas, *Phys. Rev.* **D84**, 106005 (2011), arXiv:1106.4804 [hep-th]
[70] B. Volker *et. al.*, *J. High Energy Phys.* **05**, 043 (2006), arXiv:hep-th/0512177
[71] W. Buchmuller *et. al.*, *Phys. Rev. Lett.* **96**, 121602 (2006), arXiv:hep-ph/0511035
[72] W. Buchmuller *et. al.*, *Nucl. Phys.* **B785**, 149 (2007), arXiv:hep-th/0606187
[73] B.S. Acharya, G. Kane and P. Kuma, *Int. J. Mod. Phys.* **A27**, 1230012 (2012), arXiv:1204.2795 [hep-ph]
[74] A. Hebecker and J. March-Russell, *Phys. Lett.* **B539**, 119 (2002), arXiv:hep-ph/0204037
[75] Y. Kawamura, *Prog. Theor. Phys.* **105**, 999 (2001), arXiv:hep-ph/0012125
[76] P. Nath and P.F. Perez, *Phys. Rept.* **441**, 191 (2007), arXiv:hep-ph/0601023
[77] T. Haines *et. al.* (IMB Collaboration), *Phys. Rev. Lett.* **57**, 1986 (1986)
[78] W. Gajewski *et. al.* (IMB Collaboration), *Phys. Rev.* **D42**, 2974 (1990)
[79] K.S. Hirata *et. al.* (Kamiokande Collaboration), *Phys. Lett.* **B220**, 308 (1989)
[80] M. Shiozawa *et. al.* (Kamiokande Collaboration), *Phys. Rev. Lett.* **D81**, 3319 (1998), arXiv:hep-ex/9806014
[81] M.B. Einhorn and D.R.T. Jones, *Nucl. Phys.* **B196**, 475 (1982)
[82] L.E. Ibanez and G.G. Ross, *Phys. Lett.* **B105**, 439 (1981)
[83] S. Dimopoulos and H. Georgi, *Nucl. Phys.* **B193**, 150 (1981)
[84] M.C. Chen, M. Ratz and V. Takhistov, *Nucl. Phys.* **B891**, 322 (2014), arXiv:1410.3474 [hep-ph]
[85] G.R. Farrar and P. Fayet, *Phys. Lett.* **B76**, 575 (1978)
[86] H.M. Lee *et. al.*, *Phys. Lett.* **B694**, 491 (2011), arXiv:1009.0905 [hep-ph]

[87] J. Hisano, H. Murayama and T. Yanagida, *Nucl. Phys.* **B402**, 46 (1993), hep-ph/9207279

[88] Y. Aoki *et. al.* (RBC-UKQCD Collaboration), *Phys. Rev.* **D78**, 054505 (2008), arXiv:0806.1031 [hep-lat]

[89] Y. Aoki *et. al.*, *Phys. Rev.* **D75**, 014507 (2007), arXiv:hep-lat/0607002

[90] H. Murayama and A. Pierce, *Phys. Rev.* **D65**, 055009 (2002), arXiv:hep-ph/0108104

[91] K. Kobayashi *et. al.* (Super-Kamiokande Collaboration), *Phys. Rev.* **D72**, 052007 (2005), arXiv:hep-ex/0502026

[92] J. Beringer *et. al.* (Particle Data Group), *Phys. Rev.* **D86**, 010001 (2012)

[93] R.N. Mohapatra, *J. Phys.* **G36**, 104006 (2009), arXiv:0902.0834 [hep-ph]

[94] M. Baldo-Ceolin *et. al.*, *Z. Phys.* **C36**, 409 (1994)

[95] K.S. Babu and R.N. Mohapatra, *Phys. Lett.* **B715**, 328 (2012), arXiv:1206.570 [hep-ph]

[96] P.A.M. Dirac, *Proc. Roy. Soc. Lond.* **A133**, 60 (1931)

[97] G. t' Hooft, *Nucl. Phys.* **B79**, 276 (1974)

[98] A.M. Polyakov, *JETP Lett.* **20**, 194 (1974)

[99] V.A. Rubakov, *JETP Lett.* **33**, 644 (1981)

[100] C.G. Callan, *Nucl. Phys.* **B212**, 391 (1983)

[101] S. Coleman, *Phys. Lett.* **B262**, 263 (1985)

[102] G.R. Dvali, A. Kusenko and M.E. Shaposhnikov, *Phys. Lett.* **B417**, 99 (1998), arXiv:hep-ph/9707423

[103] P.A.R. Ade *et. al.* (Planck Collaboration), *Astron. Astrophys.* **571**, A16 (2014), arXiv:1303.5076 [astro-ph.CO]

[104] C.L. Bennett *et. al.* (WMAP Collaboration), *Astrophys. J. Suppl.* **208**, 20 (2013), arXiv:1212.5225 [astro-ph.CO]

[105] O. Adriani *et. al.* (PAMELA Collaboration), *Phys. Rev. Lett.* **105**, 121101 (2010), arXiv:1007.0821 [astro-ph.HE]

[106] A.H. Guth, *Phys. Rev.* **D23**, 347 (1981)

[107] A.D. Linde, *Phys. Lett.* **B108**, 389 (1982)

[108] A. Albrecht and P.J. Steinhardt, *Phys. Rev. Lett.* **48**, 1220 (1982)

[109] J. Martin *et. al.* (WMAP Collaboration), *JCAP* **1403**, 039 (2014), arXiv:1312.3529 [astro-ph.CO]

[110] A.G. Cohen, A.D. Rujula and S.L. Glashow, *Astrophys. J.* **495**, 539 (1998)

[111] M. Dine and A. Kusenko, *Rev. Mod. Phys.* **76**, 1 (2003)

[112] M. Fukugita and T. Yanagida, *Phys. Lett.* **B174**, 45 (1986)

[113] I. Affleck and M. Dine, *Nucl. Phys.* **B249**, 361 (1985)

[114] M. Goldhaber, *unpublished* (1954)

[115] F. Reines, C.L. Cowan and M. Goldhaber, *Phys. Rev.* **96**, 1157 (1954)
[116] F. Reines, C.L. Cowan and H.W. Kruse, *Phys. Rev.* **109**, 609 (1958)
[117] G.N. Flerov *et. al.*, *Sov. Phys. Dokl.* **3**, 79 (1958)
[118] G.K. Backenstoss *et. al.*, *Nuovo Cim.* **16**, 749 (1960)
[119] C.C. Giamati and F. Reines, *Phys. Rev.* **126**, 2178 (1962)
[120] W.R. Kropp and F. Reines, *Phys. Rev.* **137**, B740 (1965)
[121] H.S. Gurr *et. al.*, *Phys. Rev.* **158**, 1321 (1967)
[122] L. Bergamasco and P. Picchi, *Nuovo Cim. Lett.* **11**, 636 (1974)
[123] F. Reines and M.F. Crouch, *Phys. Rev. Lett.* **32**, 493 (1974)
[124] R.I. Steinberg and J.C. Evans, *Proceedings for 5th Neutrino Conference* (1977)
[125] E.L. Fireman, *Proceedings for 16th International Cosmic Ray Conference* (1977)
[126] M.L. Cherry *et. al.* (Homestake Collaboration), *Phys. Rev. Lett.* **47**, 1507 (1981)
[127] G. Battistoni *et. al.* (NUSEX Collaboration), *Phys. Lett.* **B118**, 461 (1982)
[128] M.R. Krishnaswamy *et. al.* (KGF Collaboration), *Nuovo Cim.* **C9**, 167 (1986)
[129] J.E. Bartelt *et. al.* (Soudan Collaboration), *Phys. Rev.* **D36**, 1987 (1990)
[130] C. Berger *et. al.* (Frejus Collaboration), *Z. Phys.* **C50**, 385 (1991)
[131] C. McGrew *et. al.* (IMB Collaboration), *Phys. Rev.* **D59**, 052004 (1999)
[132] H. Nishino *et. al.* (Super-Kamiokande Collaboration), *Phys. Rev.* **D85**, 112001 (2012), arXiv:1203.4030 [hep-ex]
[133] Y. Takenaga *et. al.* (Super-Kamiokande Collaboration), *Phys. Lett.* **B647**, 18 (2007), arXiv:hep-ex/0608057 [hep-ex]
[134] K. Ueno *et. al.* (Super-Kamiokande Collaboration), *Astropart. Phys.* **36**, 131 (2012), arXiv:1203.0940 [hep-ex]
[135] J.C. Pati, *Phys. Rev.* **D29**, 1549 (1984)
[136] J.C. Pati, A. Salam and U. Sarkar, *Phys. Lett.* **B133**, 330 (1983)
[137] J.C. Pati and A. Salam, *Phys. Rev.* **D10**, 275 (1974)
[138] C. Berger *et. al.*, *Phys. Lett.* **B269**, 227 (1991)
[139] P.H. Gu and U. Sarkar, *Mod. Phys. Lett.* **A28**, 1350159 (2013), arXiv:1110.4581 [hep-ph]
[140] W.A. Mann, T. Kafka and W. Leeson, *Phys. Lett.* **B291**, 200 (1992)
[141] P.J. O'Donnell and U. Sarkar, *Phys. Lett.* **B316**, 121 (1993), arXiv:hep-ph/9307254
[142] Y. Fukuda *et. al.* (Kamiokande Collaboration), *Phys. Lett.* **B335**, 237 (1994)
[143] R. Becker-Szenday *et. al.* (IMB Collaboration), *Phys. Rev.* **D46**, 3720 (1992)
[144] J. Learned, F. Reines and A. Soni, *Phys. Rev. Lett.* **43**, 907 (1979)
[145] D. Silverman and A. Soni, *Phys. Lett.* **B100**, 131 (1981)
[146] J.M. Arnold, B. Fornal and M. Wise, *Phys. Rev.* **D88**, 035009 (2013), arXiv:1304.6119

[hep-ph]
[147] M. Litos *et. al.* (Super-Kamiokande Collaboration), *Phys. Rev. Lett.* **13**, 112 (2014)
[148] T. Araki *et. al.* (KamLAND Collaboration), *Phys. Rev. Lett.* **96**, 101802 (2006), arXiv:hep-ex/0512059
[149] R.N. Mohapatra and G. Senjanovic, *Phys. Rev. Lett.* **49**, 7 (1982)
[150] L. Arnellos and W.J. Marciano, *Phys. Rev. Lett.* **48**, 1708 (1982)
[151] D. Bryman, *Phys. Lett.* **B733**, 190 (2014), arXiv:1404.7776 [hep-ex]
[152] R. Wendell *et. al.* (Super-Kamiokande Collaboration), *Phys. Rev.* **D81**, 092004 (2010), arXiv:1002.3471 [hep-ex]
[153] K. Choi *et. al.* (Super-Kamiokande Collaboration), *Phys. Rev. Lett.* **114**, 141301 (2015), arXiv:1503.04858 [hep-ex]
[154] G. Fogli *et. al.*, *Phys. Rev.* **D66**, 053010 (2002), arXiv:hep-ph/0206162
[155] V. Takhistov *et. al.* (Super-Kamiokande Collaboration), *Phys. Rev. Lett.* **113**, 101801 (2014), arXiv:1409.1947 [hep-ex]
[156] V. Takhistov *et. al.* (Super-Kamiokande Collaboration), *Phys. Rev. Lett.* **115**, 12 (2015), arXiv:1508.05530 [hep-ex]
[157] M.C. Chen and V. Takhistov, *Phys. Rev.* **D89**, 095003 (2014)
[158] K. Abe *et. al.* (Super-Kamiokande Collaboration), *Nucl. Instrum. Meth.* **A737**, 418 (2003), arXiv:1307.0162 [physics.ins-det]
[159] I.M. Frank and I. Tamm, *C. R. Acad. Sci. USSR* **14**, 109 (1937)
[160] Y. Ashie *et. al.* (Super-Kamiokande Collaboration), *Phys. Rev.* **D71**, 112005 (2005)
[161] L.R.B. Elton and A. Swift, *Nucl. Phys.* **A94**, 52 (1967)
[162] K. Nakamura *et. al.*, *Nucl. Phys.* **A268**, 381 (1976)
[163] R. Woods and D. Saxon *Phys. Rev.* **95**, 577 (1954)
[164] M. Shiozawa, Ph.D. Thesis, University of Tokyo (1999)
[165] T. Yamazaki and Y. Akaishi, *Phys. Lett.* **B453**, 1 (1999)
[166] H. Ejiri, *Phys. Rev.* **C48**, 1442 (1993)
[167] Y.A Kamyshov and E. Kolbe, *Phys. Rev.* **D67**, 076007 (2003)
[168] K. Abe *et. al.* (Super-Kamiokande Collaboration), *Phys. Rev.* **D90**, 072005 (2014), 1408.1195 [hep-ex]
[169] Y. Suzuki *et. al.* (Kamiokande Collaboration), *Phys. Lett.* **B311**, 357 (1993)
[170] R. Brun, F. Carminati and S. Giani, CERN-W5013 (1994)
[171] S. Jadach *et. al.*, *Comp. Phys. Comm.* **76**, 361 (1993)
[172] K. Abe *et. al.* (Super-Kamiokande Collaboration), *Phys. Rev. Lett.* **110**, 181802 (2013), arXiv:1206.0328 [hep-ex]
[173] W. Fetscher, *Phys. Rev.* **D42**, 1544 (1990)

[174] B. Louis *et. al.*, *Los Alamos Sci.* **25**, 16 (1997)

[175] M. Honda *et. al.*, *Phys. Rev.* **D70**, 4 (2004)

[176] W.R. Webber, R.L. Golden and S.A. Stephens, *Proceedings of 20th Int. Cosmic Ray Conf.* **1**, 325 (1987)

[177] W.S. Seo *et. al.* (LEAP Collaboration), *Astrophys. J.* **378**, 763 (1987)

[178] P. Pappini *et. al.* (WIZARD-MASS Collaboration), *Proceedings of 23rd Int. Cosmic Ray Conf.* **1**, 579 (1993)

[179] G. Boezio *et. al.* (CAPRICE Collaboration), *Astrophys. J.* **518**, 457 (1999)

[180] W. Menn *et. al.* (IMAX Collaboration), *Astrophys. J.* **533**, 281 (2000)

[181] T. Sanuki *et. al.* (BESS Collaboration), *Astrophys. J.* **545**, 1135 (2000)

[182] S. Alcaraz *et. al.* (AMS Collaboration), *Phys. Lett.* **B490**, 27 (2000)

[183] M. Ryan, J.F. Ormes and V.K. Balasubrahmanyan, *Phys. Rev. Lett.* **28**, 985 (1972)

[184] K. Asakimori *et. al.* (JACEE Collaboration), *Astrophys. J.* **502**, 278 (1998)

[185] I.P. Ivanenko *et. al.*, *Proceedings of 23rd Int. Cosmic Ray Conf.* **2**, 17 (1993)

[186] Y. Kawamura *et. al.*, *Phys. Rev.* **D40**, 729 (1989)

[187] A.V. Apanasenko *et. al.* (RUNJOB Collaboration), *Astropart. Phys.* **16**, 13 (2001)

[188] K. Hänssgen and J. Ranft, *Comp. Phys. Comm.* **39**, 1153 (1986)

[189] S. Roesler, R. Engel and J. Ranft, *Phys. Rev.* **D57**, 2889 (1998)

[190] G. Battistoni *et. al.*, *Astropart. Phys.* **19**, 269 (2003)

[191] G.D. Barr *et. al.*, *Phys. Rev.* **D70**, 023006 (2004)

[192] Y. Hayato, (Proceeding Suppl.) *Nucl. Phys.* **B112**, 171 (2002)

[193] D. Casper, (Proceeding Suppl.) *Nucl. Phys.* **B112**, 161 (2002)

[194] R. Wendell, Ph.D. Thesis, University of North Carolina at Chapel Hill (2008)

[195] C.H. Llewellyn-Smith, *Phys. Rep.* **3**, 261 (1972)

[196] R. Gran *et. al.*, *Phys. Rev.* **D74**, 052002 (2006)

[197] R.A. Smith and E.J. Moniz, *Nucl. Phys.* **B43**, 605 (2002)

[198] J. Nieves *et. al.*, *Phys. Rev.* **C70**, 055503 (2004)

[199] H. Nakamura *et. al.*, (Proceeding Suppl.) *Nucl. Phys.* **B112**, 197 (2002)

[200] C.H. Albright *et. al.*, *Phys. Rev.* **D14**, 1780 (1976)

[201] K. Abe *et. al.*, *Phys. Rev. Lett.* **56**, 1107 (1986)

[202] S.J. Barish *et. al.*, *Phys. Rev.* **D16**, 3103 (1977)

[203] S. Bonetti *et. al.* (Gargamelle Collaboration), *Nuovo Cim.* **A38**, 260 (1977)

[204] M. Pohl *et. al.* (Gargamelle Collaboration), *Lett. Nuovo Cim.* **26**, 332 (1979)

[205] N. Armenise *et. al.* (Gargamelle Collaboration), *Nucl. Phys.* **B152**, 365 (1979)

[206] A.S. Vovenko *et. al.*, *Sov. J. Nucl. Phys.* **30**, 528 (1979)

[207] S.V. Belikov *et. al.*, *Z. Phys.* **A320**, 625 (1985)

[208] J. Brunner *et. al.* (SKAT Collaboration), *Z. Phys.* **C45**, 551 (1990)

[209] Y. Hayato, (Proceedings) *Acta Phys. Polon.* **B40**, 2477 (2009)

[210] D. Rein and L.M. Sehgal, *Ann. Phys.* **133**, 79 (1981)

[211] D. Rein, *Z. Phys.* **C35**, 43 (1987)

[212] R.P. Feynman, M. Kislinger and F. Ravndal, *Phys. Rev.* **D3**, 2706 (1971)

[213] T. Kitagaki *et. al.*, *Phys. Rev.* **D34**, 2554 (1986)

[214] S.K. Singh, M.J. Vicente-Vacas and E. Oset, *Phys. Lett.* **B416**, 23 (1998)

[215] M. Hasegawa *et. al.* (K2K Collaboration), *Phys. Rev. Lett.* **95**, 252301 (2005)

[216] A. Kartavtsev, E.A. Paschos and G.J. Gounaris, *Phys. Rev.* **D74**, 054007 (2006)

[217] M. Glück, E. Reya and A. Vogt, *Eur. Phys. J.* **C5**, 461 (1998)

[218] S.J. Barish *et. al.*, *Phys. Rev.* **D17**, 1 (1978)

[219] S. Barlag *et. al.*, *Z. Phys.* **C11**, 283 (1982)

[220] T. Sjöstrand *et. al.*, CERN-TH-7112-93 (1994)

[221] P. Musset and J.P. Vialle, *Phys. Rep.* **C39**, 1 (1978)

[222] J.E. Kim *et. al.*, *Rev. Mod. Phys.* **53**, 211 (1981)

[223] L. Salcedo *et. al.*, *Nucl. Phys.* **A484**, 577 (1988)

[224] D. Ashery *et. al.*, *Phys. Rev.* **C23**, 2173 (1981)

[225] C. Ingram *et. al.*, *Phys. Rev.* **C27**, 1578 (1983)

[226] H.W. Bertinie *et. al.*, *Phys. Rev.* **C6**, 631 (1972)

[227] S.J. Lindenbaum *et. al.*, *Phys. Rev.* **105**, 1874 (1957)

[228] K. Abe *et. al.* (Super-Kamiokande Collaboration), *Phys. Rev. Lett.* **107**, 241801 (2011), arXiv:1109.1621 [hep-ex]

[229] T. Gabriel, J. Brau and B. Bishop, *Nucl. Sci. IEEE Trans.* **36**, 14 (1989)

[230] C. Zeitnitz, T.A. Gabriel, *Nucl. Inst. and Meth. in Phys. Res.* **A349**, 106 (1994)

[231] M. Nakahata *et. al.* (Kamiokande Collaboration), *J. Phys. Soc. Jap.* **55**, 3786 (1986)

[232] E. Bracci *et. al.*, CERN-HERA-72-01 (1979)

[233] A. Carroll *et. al.*, *Phys. Rev.* **C14**, 635 (1976)

[234] C. Regis, Ph.D. Thesis, University of California at Irvine (2010)

[235] E. Davies, *Machine Vision: Theory, Algorithms, Practicalities*, Academic Press (1977)

[236] H. Nishino, Ph.D. Thesis, University of Tokyo (2009)

[237] Y. Itow, (Proceeding Supplements) *Nucl. Phys.* **B112**, 1 (2002)

[238] S. Kasuga *et. al.* (Kamiokande Collaboration), *Phys. Lett.* **B374**, 238 (1996)

[239] M. Litos, Ph.D. Thesis, Boston University (2010)

[240] Y. Takenaga, Ph.D. Thesis, University of Tokyo (2008)

[241] M. Honda *et. al.*, *Phys. Rev.* **D75**, 043006 (2007), arXiv:astro-ph/0611418

[242] M. Honda *et. al.*, *Phys. Rev.* **D83**, 123001 (2011), arXiv:1102.2688 [astro-ph.HE]

[243] K. Abe *et. al.* (Super-Kamiokande Collaboration), *Phys. Rev. Lett.* **12**, 113 (2014), arXiv:1305.4391 [hep-ex]

[244] L.K. Pik, Ph.D. Thesis, University of Tokyo (2012)

[245] K. Abe *et. al.* (Hyper-K Collaboration), (2011) arXiv:1109.3262 [hep-ex]

[246] J. Strait *et. al.* (DUNE Collaboration), (2016) arXiv:1601.05823 [physics.ins-det]

[247] J.C. Pati and A. Salam, *Phys. Rev. Lett.* **31**, 661 (1973)

[248] E. Commins and P. Bucksbaum, *Weak Interactions of Leptons and Quarks*, Cambridge University Press (1983)

[249] T. Kinoshita and A. Sirlin, *Phys. Rev.* **113**, 1652 (1959)

[250] L. Michel, *Proc. Phys. Soc.* **A63**, 514 (1950)

[251] T. Kinoshita and A. Sirlin, *Phys. Rev.* **108**, 844 (1957)

[252] R. Behrends, R. Finkelstein and A. Sirlin, *Phys. Rev.* **101**, 866 (1956)

[253] W. Fetscher, *Phys. Rev.* **D42**, 1544 (1990)

Appendix A

Trilepton Decay Channels from Pati-Salam

We provide an overview of the Pati-Salam model that could lead to sizable trilepton decay channels, following Ref. [135]. The minimal Higgs content of the Pati-Salam theory needed to break $G_{PS} \to G_{SM}$ and explain the quark-lepton spectrum is the following [136]: $\Delta_R(10,1,3)$, $\Delta_L(10,3,1)$, $\phi(1,2,2)$ and $\xi(15,2,2)$ - where the $SU(4) \times SU(2)_R \times SU(2)_L$ gauge group transformations are noted in the parenthesis. Consistency with phenomenology requires that the vevs are taken to be $\langle \Delta_R \rangle \gg \langle \phi \rangle \sim \langle \xi \rangle \gg \langle \Delta_L \rangle$. The full symmetry breaking chain is

$$
\begin{array}{cl}
SO(10) & \\
\downarrow & M_{GUT} \\
SU(4) \times SU(2)_L \times SU(2)_R & \\
\downarrow & \langle \Delta_R \rangle \sim M_{Intermediate} \\
SU(3)_C \times SU(2)_L \times U(1) & \\
\downarrow & \langle \phi \rangle \sim \langle \xi \rangle \sim M_{EW} \\
SU(3)_C \times U(1)_{EM} &
\end{array}
\tag{A.1}
$$

where a choice of $M_U \sim 10^{15}$ GeV as well as $M_R \sim 10^{12}$ GeV is consistent with neutrino related measurements and gives $\sin\theta_W \sim 0.23$. The above can embedded into $SO(10)$, using **10** and **126** $SO(10)$ multiplets, which contain all of the Δ_R, Δ_L, ϕ and ξ PS multiplets. Additional $\mathbf{54}, \mathbf{210}$ can be used for $SO(10)$ breaking. The explicit decomposition of the relevant $SO(10)$ multiplets under PS $SU(4) \times SU(2)_R \times SU(2)_L$ is

$$\begin{aligned} \mathbf{54} &= (1,1,1) + (6,2,2) + (1,3,3) + (20,1,1) \ , \\ \mathbf{126} &= (10,1,3) + (10,3,1) + (15,2,2) + (6,1,1) \ , \\ \mathbf{10} &= (1,2,2) + (6,1,1) \ . \end{aligned} \tag{A.2}$$

In the scenario outlined above, the desired nucleon decay modes arise from invariant $\Delta^2\xi^2$ terms, which lead to diagrams on Figure A.1. Here, $\xi_{\bar{3}}$ and $\xi_{\bar{8}}$ are the triplet and the octet

Figure A.1: Diagrams for the $p \to l l \bar{l}$ [left] and the $p \to l +$ meson [right] nucleon decays. From Ref. [135].

components of ξ. The neutral component of $\Delta_R(10,1,3)$ obtains a vev.

The respective amplitudes for the processes are given by

$$A(p \to l \ + \text{meson}) \ = \ \frac{h(\lambda_\xi)^2\lambda_\Delta\langle\Delta_R\rangle}{(m_{\xi_{\bar{3}}} m_{\xi_{\bar{8}}} m_\Delta)^2} \ , \tag{A.3a}$$

$$A(p \to l \ l \ \bar{l}) \ = \ \frac{h(\lambda_\xi)^2\lambda_\Delta\langle\Delta_R\rangle}{(m^2_{\xi_{\bar{3}}} m_\Delta)^2} \ ,$$

where λ's denote the 3 Yukawa couplings of the lepto-quarks in the diagrams above, while m's are their masses and h is the $\Delta^2\xi^2$ coupling. A priori, masses of $m_{\xi_{\bar{8}}}$ and $m_{\xi_{\bar{3}}}$ (the octet and the triplet components of ξ) are of comparable magnitude and thus the above processes have similar rate. To get the corresponding decay rates sizable, one can introduce an additional $\xi'(15,2,2)$ (from **126** or **120** of $SO(10)$). This will allow to get the octet and the triplet light using a "Higgs see-saw"-like mixing between ξ and ξ'. More so, one can instead introduce $\sigma(6,2,2)$ (from **54** of SO(10)), which contains the triplet but not the octet. This allows to get the triplet light while keeping the octet heavy, which results in the tripleton modes being more dominant than the $p \to l + meson$ channels.

Appendix B

Approximating Spectrum of 3-body Decays

Consider n-body decays of particle b with a mass M. In the center of mass frame, the general partial decay rate ($d\Gamma$) of b into n constituents, with a Lorentz invariant matrix element $\mathscr{M}$, is given by [92]

$$d\Gamma = \frac{(2\pi)^4}{2M}|\mathscr{M}|^2 \, d\Phi_n \ , \tag{B.1}$$

where $d\Phi_n$ is the is the n-body phase space

$$d\Phi_n = \delta^4(P - \sum_{i=1}^{n} p_i) \prod_{i=1}^{n} \frac{d^3 p_i}{(2\pi)^3 2E_i} \ . \tag{B.2}$$

Here, P and p_i represent the momenta of the original and the final state particles, which have energy E_i.

Assuming a 2-body decay of b, each of the final state particles will obtain energy equal to $\sim M/2$. This uniquely determines the kinematics of the process, for which the partial decay width $d\Gamma_2$ is

$$d\Gamma_2 = \frac{1}{32\pi^2}|\mathscr{M}|^2 \frac{|\mathbf{p}_1|}{\mathrm{M}^2} \, d\Omega \ , \tag{B.3}$$

where $\mathbf{p}_1 = \mathbf{p}_2$ label the resulting particle 1 and 2 momenta and $d\Omega$ is the solid angle of particle 1.

In the case of 3-body decay of b, the partial decay width $d\Gamma_3$ is specified by

$$d\Gamma_3 = \frac{1}{(2\pi)^5}\frac{1}{16\mathrm{M}}|\mathscr{M}|^2 \, dE_1 \, dE_2 \, d\alpha \, d(\cos\beta) \, d\gamma \ , \tag{B.4}$$

with dE_1, dE_2 labeling energies of resulting particles 1 and 2 (with 3 being implicitly taken into account) and (α, β, γ) specifying the Euler angle orientation of momenta relative to the parent particle.

From the above, it can be seen that for 3-body decays, unlike for the 2-body decay case, energy and momenta conservation are insufficient to fully determine the kinematics. Possible energy dependence of the matrix element $\mathscr{M}$, which encodes the model-dependent mediation mechanism, can affect the energy distribution of the final state particles.

In the nucleon decay searches, one typically simulates only the final state particles, taking into account the 4-momentum conservation. Thus, one implicitly assumes a flat-distributed phase space. For nucleon decay channels with > 2 final state particles, the above decay-rate dependence on the matrix element can be a potential issue. The trilepton $p \to e^+\nu\nu$ and $p \to \mu^+\nu\nu$ modes are of this type. We note that $p \to e^+\nu\nu$ has the same final state particles as muon decay $\mu \to e^+\nu\nu$. It can be shown [157], that under a certain set of assumptions, we can employ the effective Fermi theory formalism for the muon decay to approximate the decay spectra of the trilepton nucleon decay channels.

We will now outline the argument presented in Ref. [157]. Starting with the most general 4-fermion decay amplitude with arbitrary fermion couplings (of the vector and axial-vector (V), the scalar and pseudo-scalar (S) as well as the tensor (T) types) and assuming that detector is insensitive to the spin of the charged lepton (e^+) and neutrinos are massless, the decay rate of $\mu \to e^+\nu\nu$ is given by [248]

$$\begin{aligned}\frac{d\Gamma}{dx \, d\cos\theta} = & \ \frac{D}{32}\frac{G_F^2 m_\mu^5}{192\pi^3} \times x^2 \Big\{ \frac{1+h(x)}{1+4(m_e/m_\mu)\eta} \\ & \times \Big[12(1-x) + \frac{4}{3}\rho(8x-6) + 24\frac{m_e}{m_\mu}\frac{(1-x)}{x}\eta \Big] \\ & \pm P_\mu \xi \cos\theta \Big[4(1-x) + \frac{4}{3}\delta(8x-6) + \frac{\alpha}{2\pi}\frac{g(x)}{x^2} \Big] \Big\} \ ,\end{aligned} \tag{B.5}$$

where G_F, m_e, m_μ, E_e, P_μ are the Fermi constant, electron mass, muon mass, electron energy and muon polarization, respectively. Here, $\cos\theta$ is the angle between the electron momentum and muon spin, with $x = 2E_e/m_\mu$. Functions $g(x)$ and $h(x)$ incorporate radiative corrections [249], which in the case of muon decay give the usual peak shape in the electron's

Michel spectrum. Parameters $D,\ \rho,\ \eta,\ \xi,\ \delta$ are the Michel parameters [250, 251]. At this point all the possible S, V and T couplings, are allowed. The information about the couplings is encoded inside the Michel parameters, which are functions of the possible couplings. In the case of SM, only the left-left vector coupling g^V_{LL} is non-zero, corresponding to $(V-A)$ type current, with the full set of parameters determined to be $\rho = \xi\delta = 3/4,\ \xi = 1,\ \eta = 0$ [92].

To employ Equation (B.5) for the $p \to e^+\nu\nu$ proton decay, we substitute m_p instead of m_μ. To simplify this to the form that is useful, we note that we are only interested in the isotropic part of the spectrum, allowing us to integrate over the $\cos\theta$ portion. Additionally, since the energy spectrum (in case of free nucleon) is within 0 to $m_n/2 \sim 470$ MeV region with a mean of around $m_n/3 \sim 315$ MeV, the low energy parameter η can be neglected.

Hence, neglecting the overall normalization and assuming that mass of the final state charge lepton m_e is small with respect to mass of the initial particle m_p, the approximate isotropic spectrum for the trilepton nucleon decay can be stated as

$$\frac{d\Gamma_{\rm nuc}}{d\bar{x}} \sim \bar{x}^2 \Big\{ (1 + h(\bar{x})) \cdot \Big[12(1-\bar{x}) + \frac{4}{3}\rho(8\bar{x} - 6) \Big] \Big\}\ , \tag{B.6}$$

where we have substituted proton mass into $\bar{x} = 2E_e/m_p$. Therefore, as seen from the above, all the information about possible $S,\ V,\ T$ couplings is encoded into a single Michel parameter ρ. It should be noted, that the radiative correction function $h(\bar{x})$ has similar distribution irrespective of considered couplings [252]. Thus, Eq. B.6 is considerably general.

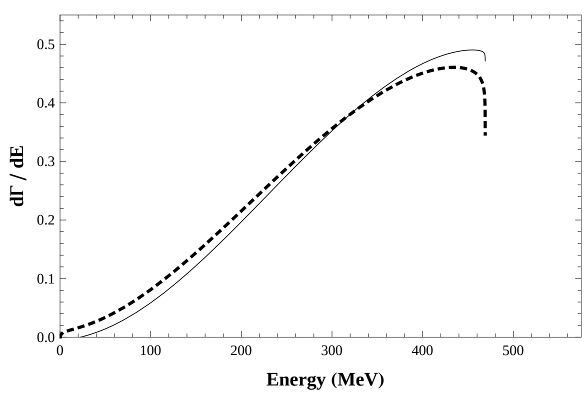

Figure B.1: Decay spectra of charge leptons e^+ (dotted line) and μ^+ (continuous line) in respective $p \to e^+\nu\bar{\nu}$ and $p \to \mu^+\nu\bar{\nu}$ decays. From Ref. [157].

Therefore, the whole isotropic energy spectra (up to normalization) for trilepton nucleon decays depends on a single parameter ρ that is a function of possible fermion S, V, T couplings, depending on the theory. In SM $\rho = 3/4$, which is responsible for the familiar Michel spectrum shape of the decay-electrons. This value is in fact quiet general and naturally appears if tensor as well as vector left-right couplings are neglected. This can be seen [253] in the SM $\tau \to e^+\nu\nu$ decay spectrum calculations. Since the decay in question is mediated by the extra Higgs (scalars) of the Pati-Salam [135] and because there is usually no tensor mediated proton decay in GUTs (e.g. $SU(5)$ [49]), the above assumption is valid for our analysis.

We can now apply the given framework to the trilepton nucleon decays to obtain the charged lepton spectra. Taking into account the radiative corrections as well as the charged lepton and the initial particle masses of $m_e = 0.511$ MeV and $m_p = 938.2$ MeV, the isotropic spectrum, up to overall normalization, is shown in Fig. B.1 as a function of energy, for the approximate e^+ spectrum in $p \to e^+\nu\bar{\nu}$ decay and the approximate μ^+ spectrum in $p \to \mu^+\nu\bar{\nu}$. The μ^+ spectrum is also reasonably approximated since the condition that the final state charged lepton mass m_μ is significantly smaller than the original parent particle mass m_p still holds, given that mass of the muon is $m_\mu = 105.7$ MeV.

Appendix C

Additional Analysis Information

C.1 Final Momentum Distributions

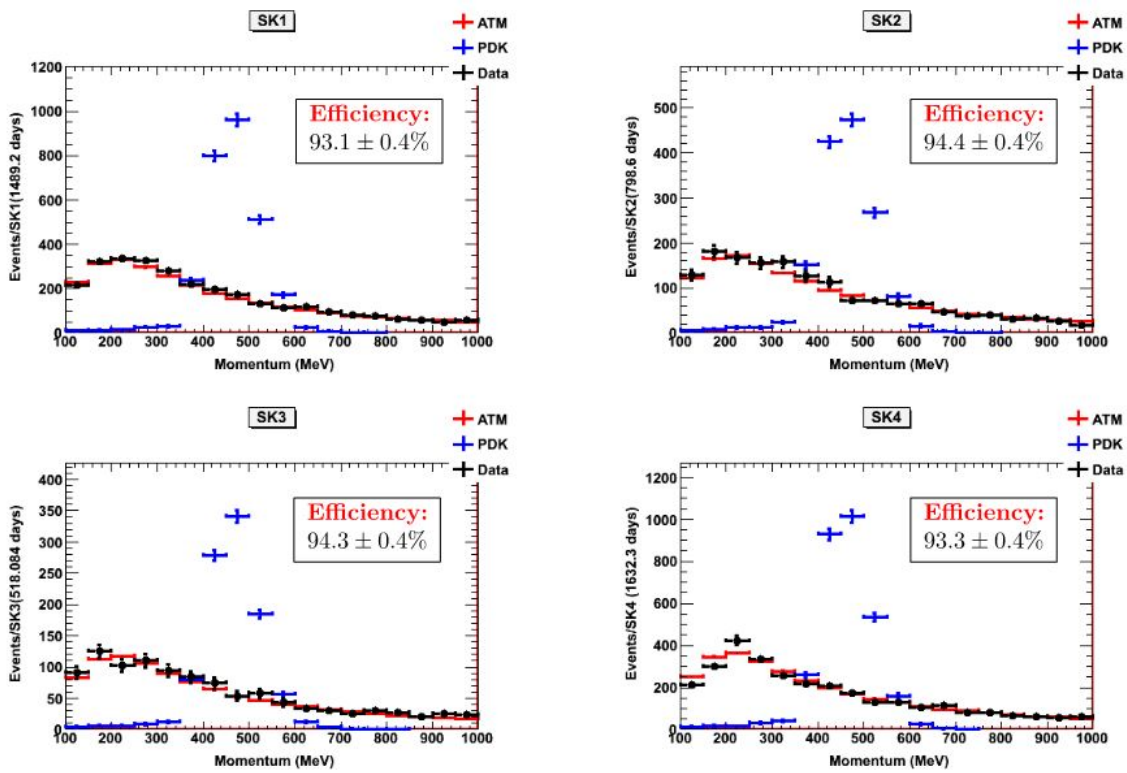

Figure C.1: Final e-like momentum distributions for $n \rightarrow \nu\gamma$.

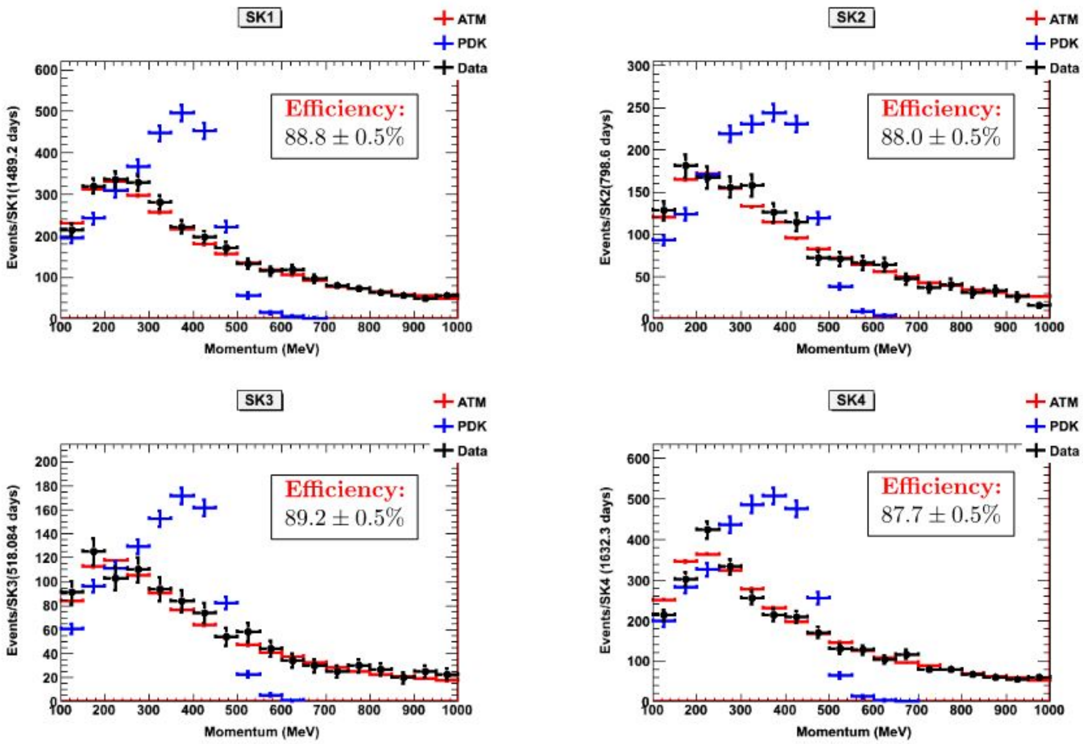

Figure C.2: Final e-like momentum distributions for $p \to e^+\nu\nu$.

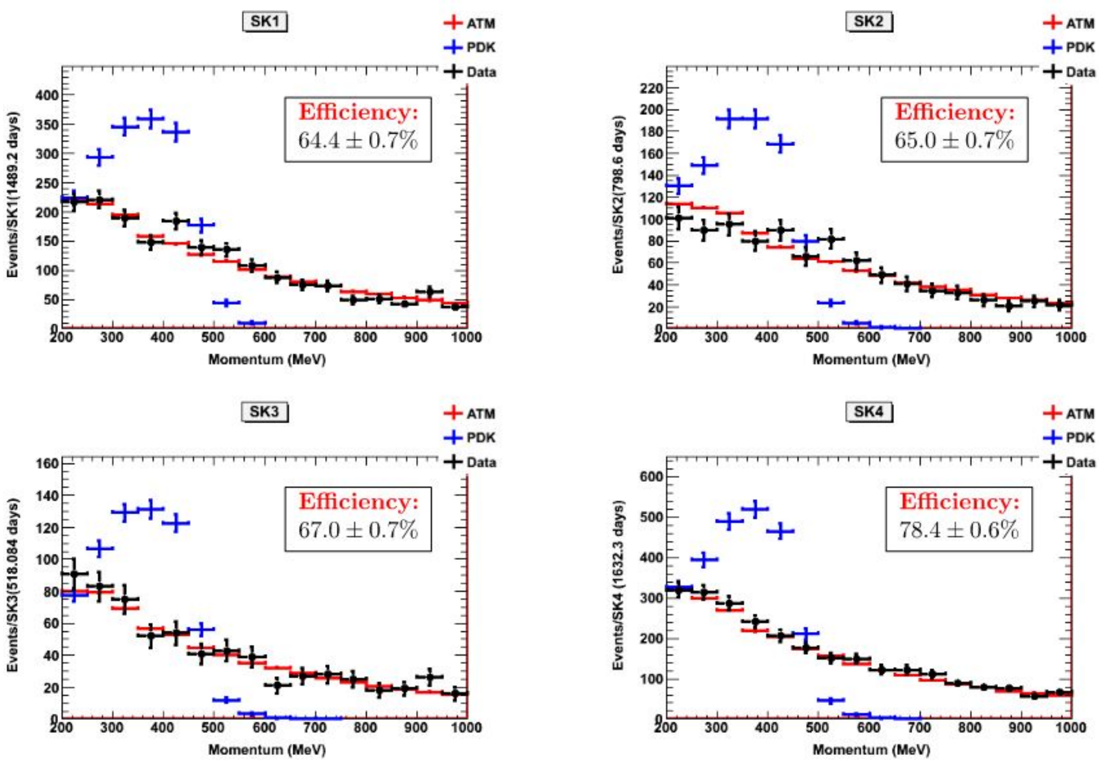

Figure C.3: Final μ-like momentum distributions for $p \to \mu^+\nu\nu$.

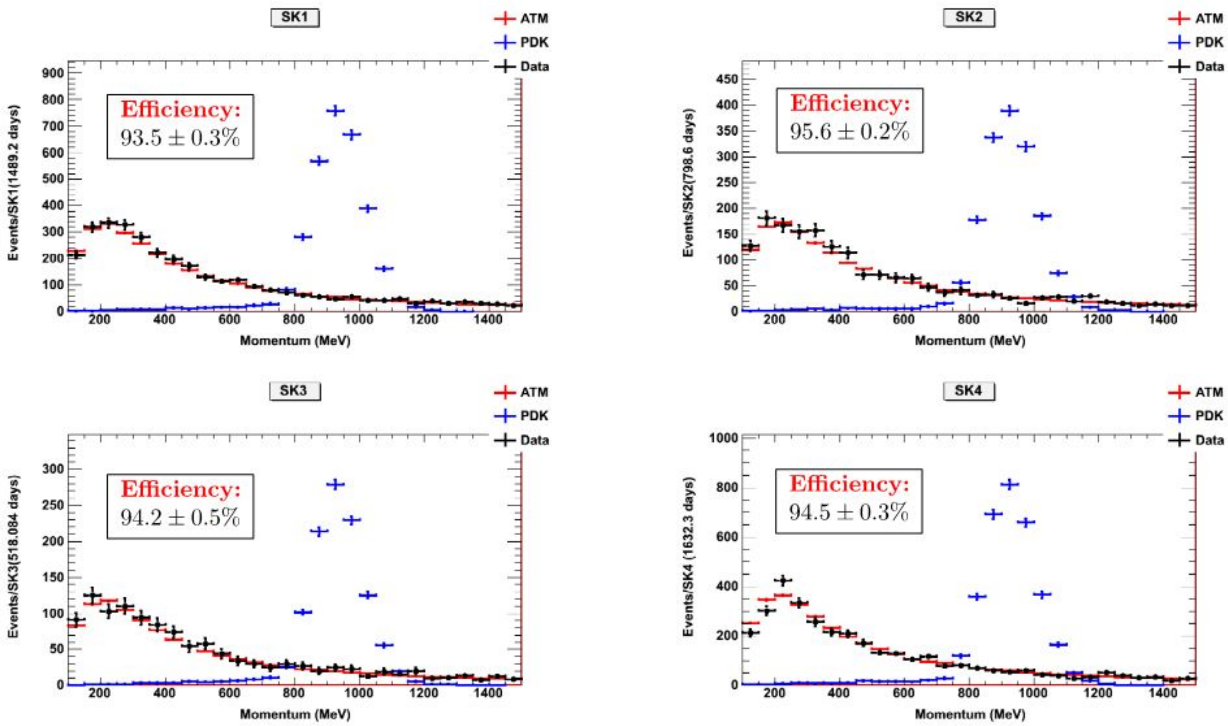

Figure C.4: Final e-like momentum distributions for $np \to e^{+}\nu$.

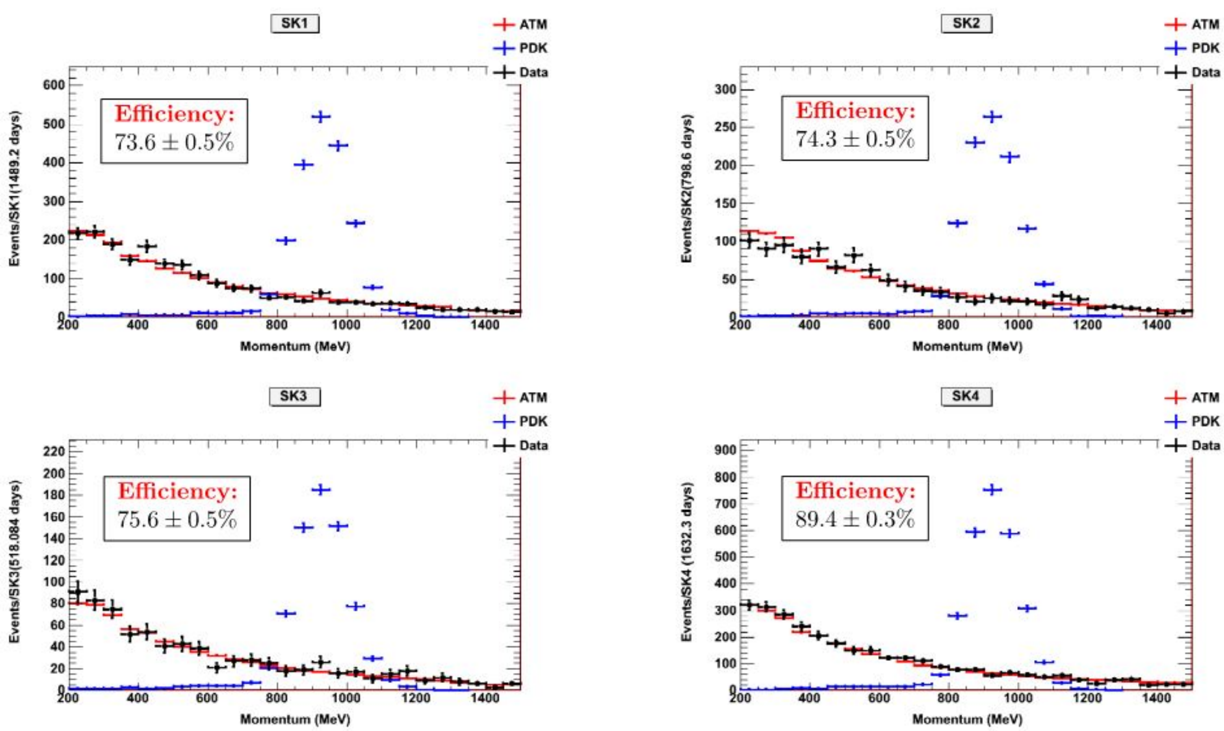

Figure C.5: Final μ-like momentum distributions for$np \to \mu^{+}\nu$.

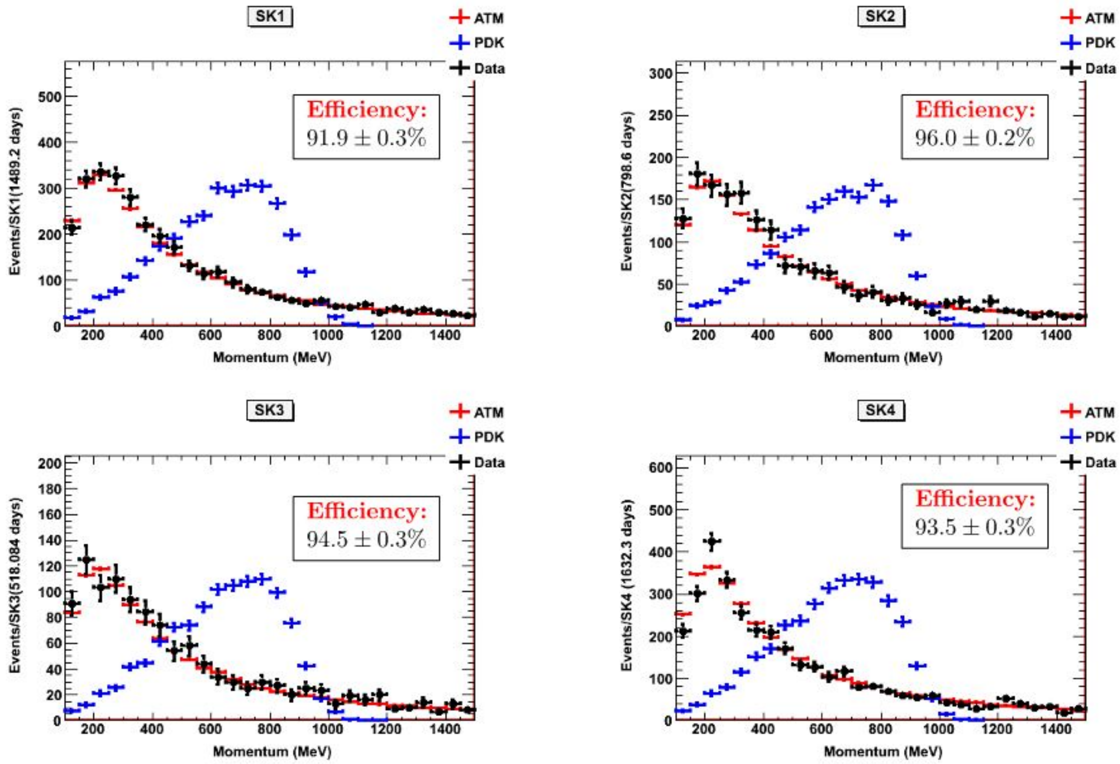

Figure C.6: Final e-like momentum distributions for $np \to \tau^+\nu(\tau^+ \to e^+\nu\nu)$.

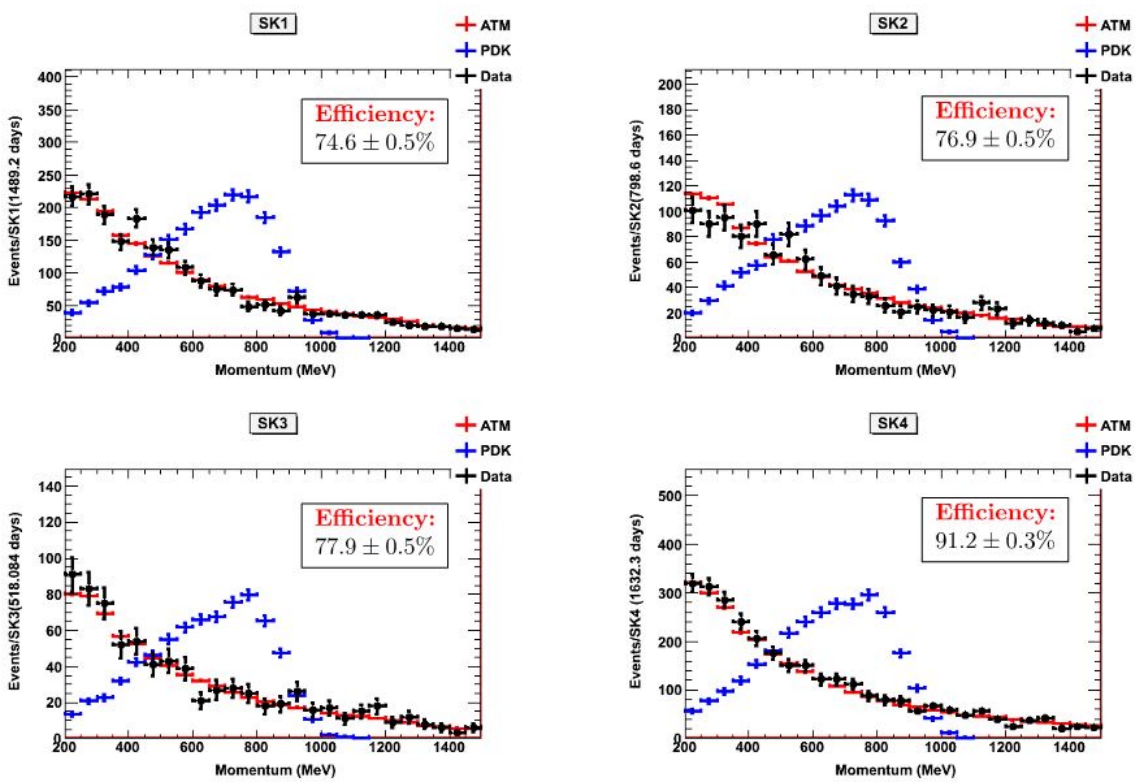

Figure C.7: Final μ-like momentum distributions for $np \to \tau^+\nu(\tau^+ \to \mu^+\nu\nu)$.

C.2 Sensitivity Results

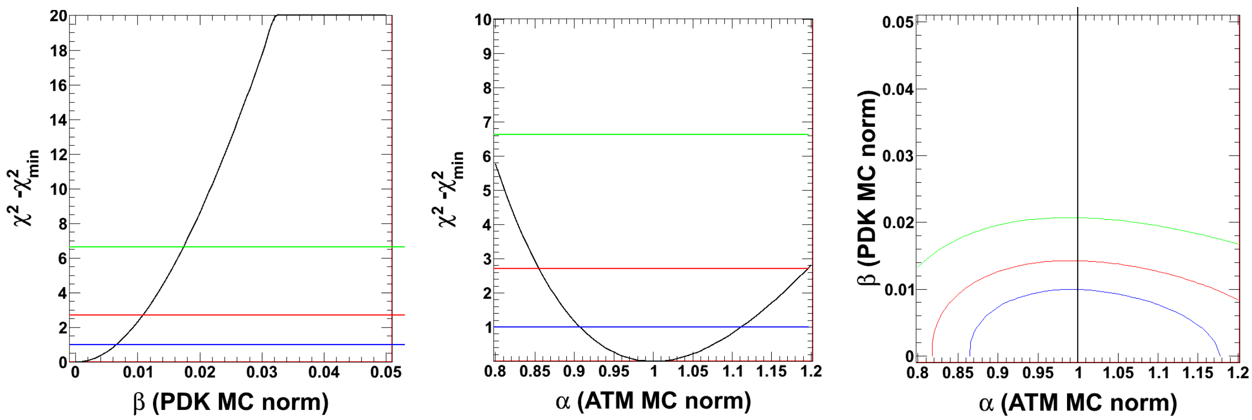

Figure C.8: MC sensitivity fit for $n \to \nu\gamma$, resulting in $\beta_{90CL} = 0.014$ (at $\alpha = 1$) [right].

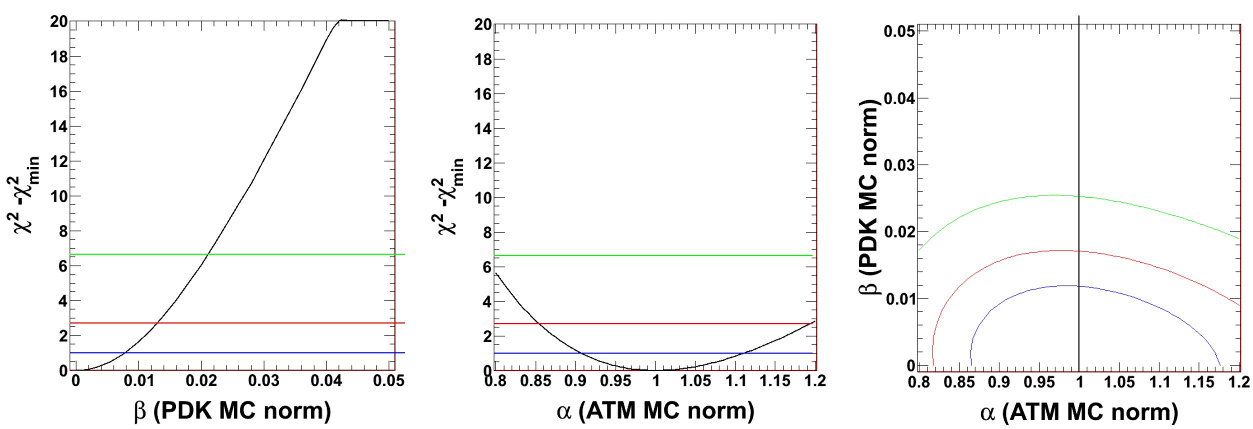

Figure C.9: MC sensitivity fit for $p \to \mu^+ X$, resulting in $\beta_{90CL} = 0.017$ (at $\alpha = 1$) [right].

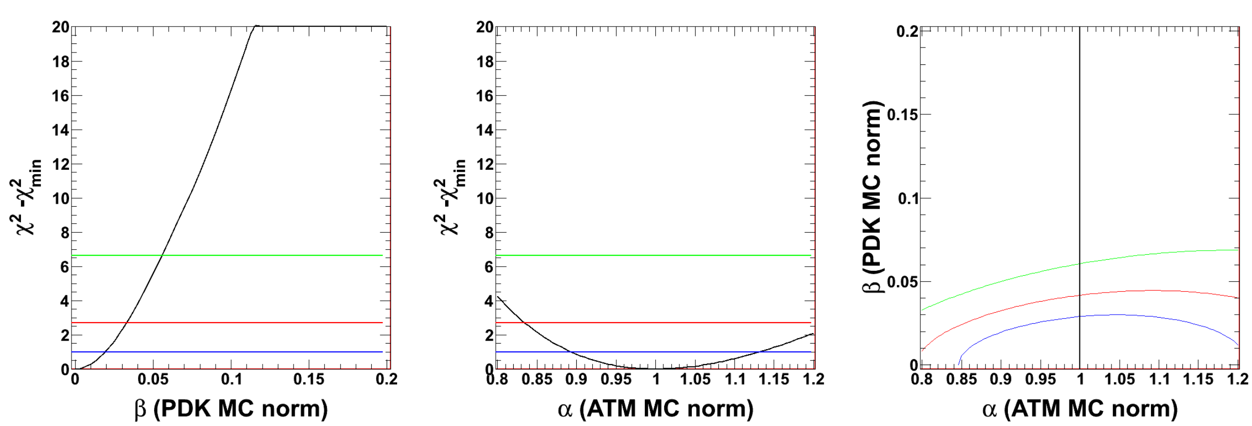

Figure C.10: MC sensitivity fit for $p \to e^+\nu\nu$, resulting in $\beta_{90CL} = 0.042$ (at $\alpha = 1$) [right].

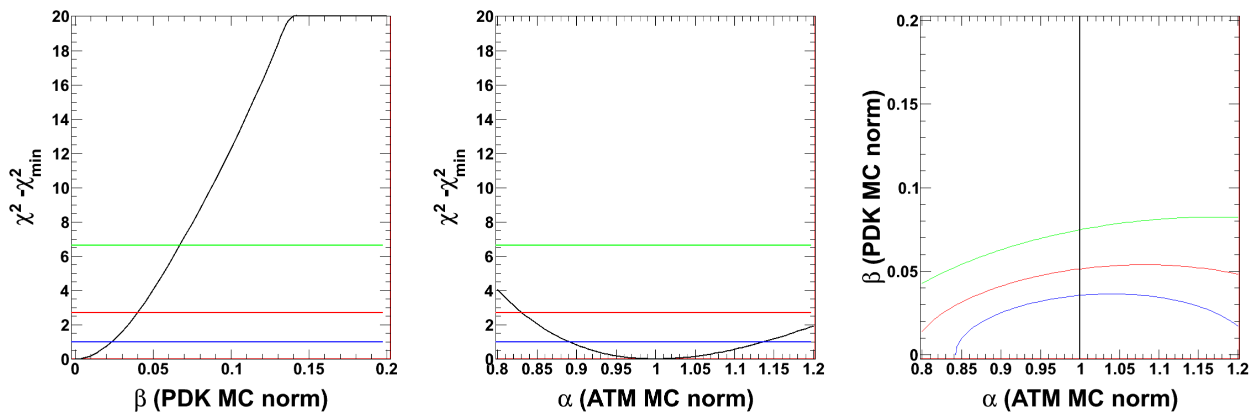

Figure C.11: MC sensitivity fit for $p \to \mu^+ \nu\nu$, resulting in $\beta_{90CL} = 0.051$ (at $\alpha = 1$) [right].

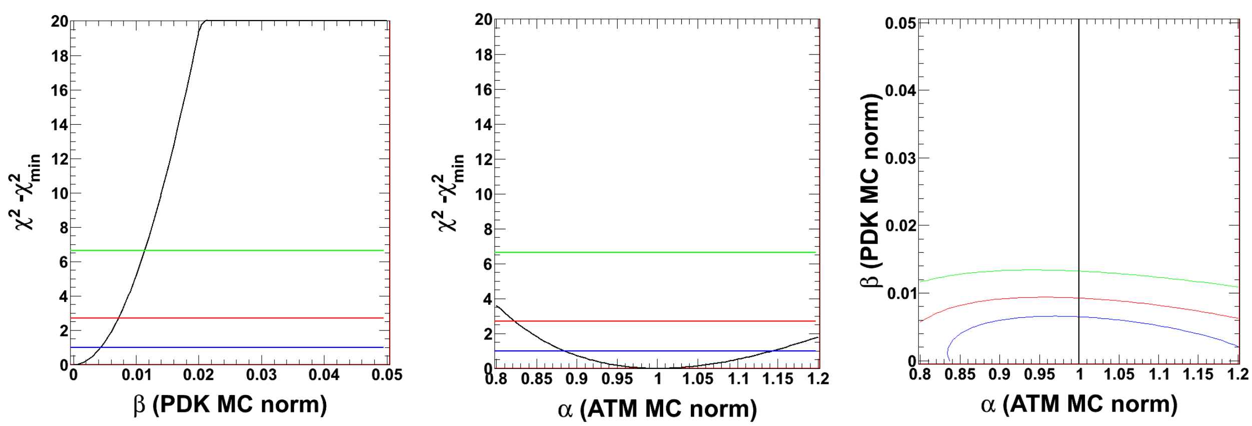

Figure C.12: MC sensitivity fit for $np \to e^+ \nu$, resulting in $\beta_{90CL} = 0.009$ (at $\alpha = 1$) [right].

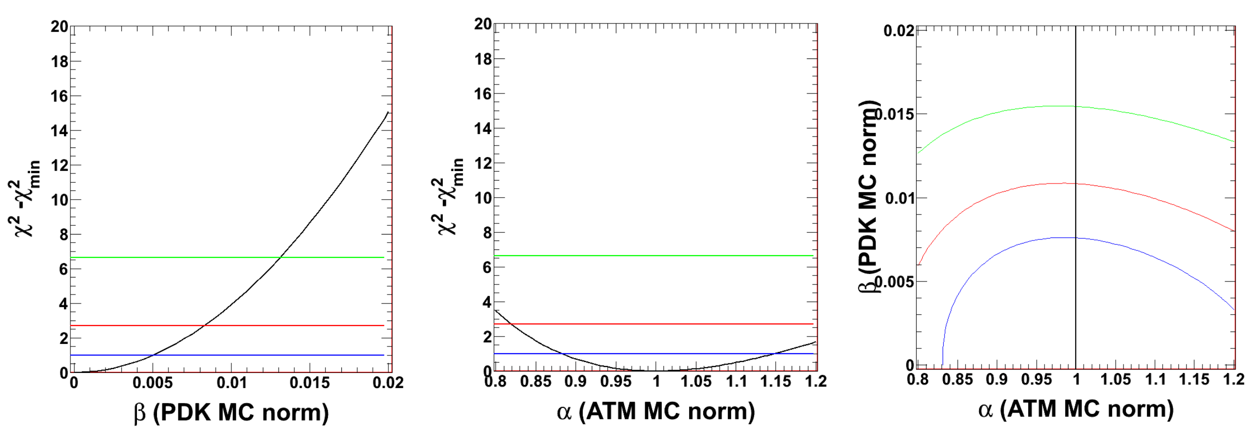

Figure C.13: MC sensitivity fit for $np \to \mu^+ \nu$, resulting in $\beta_{90CL} = 0.010$ (at $\alpha = 1$) [right].

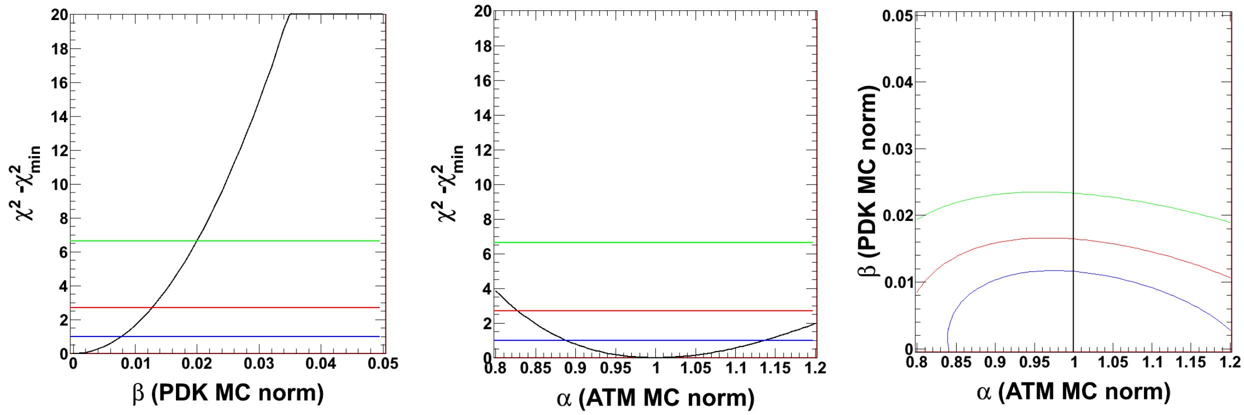

Figure C.14: MC sensitivity fit for $np \to \tau^+ \nu$, resulting in $\beta_{90CL} = 0.010$ (at $\alpha = 1$) [right].

C.3 Data Fit Results

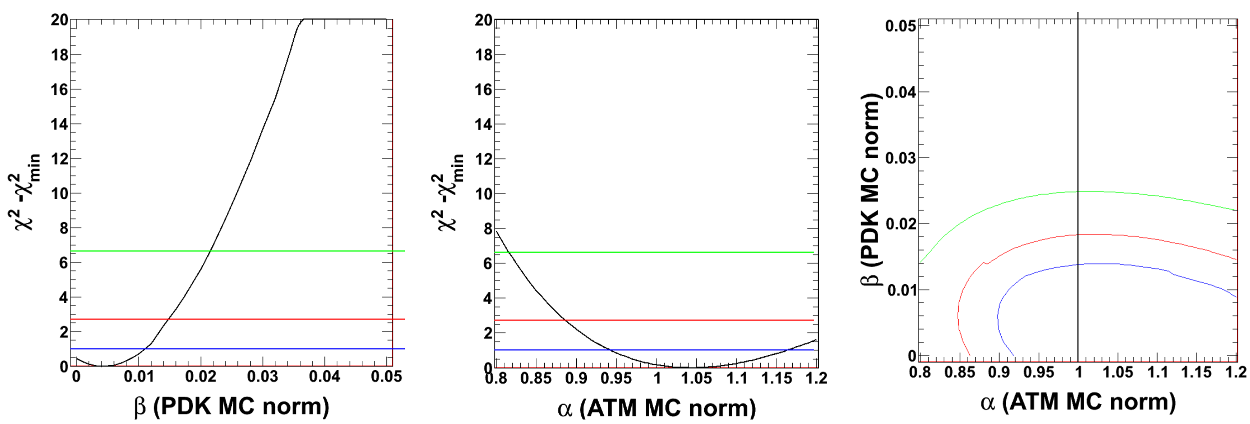

Figure C.15: Data fit for $n \to \nu\gamma$, resulting in $\beta_{90CL} = 0.015$ [left].

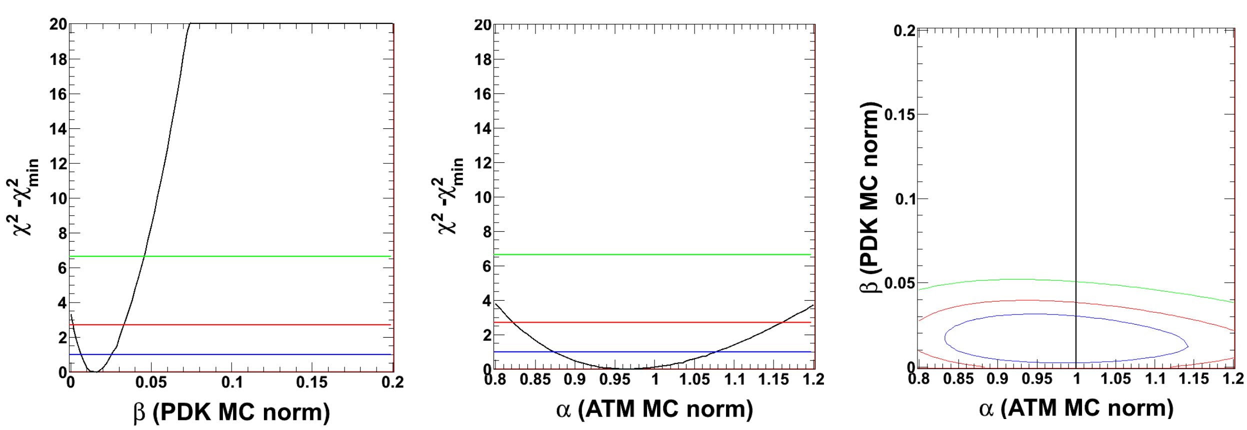

Figure C.16: Data fit for $p \to \mu^+ X$, resulting in $\beta_{90CL} = 0.032$ [left].

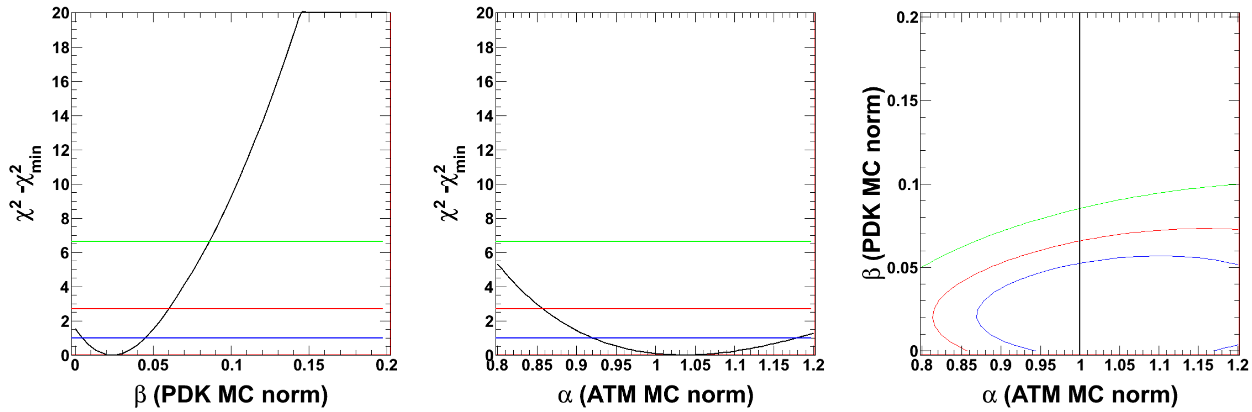

Figure C.17: Data fit for $p \to e^+\nu\nu$, resulting in $\beta_{90CL} = 0.050$ [left].

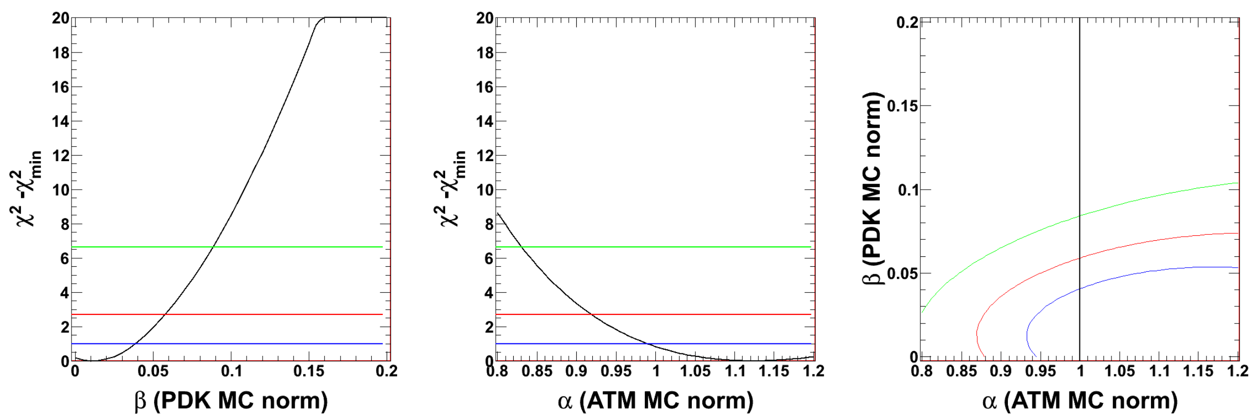

Figure C.18: Data fit for $p \to \mu^+\nu\nu$, resulting in $\beta_{90CL} = 0.060$ [left].

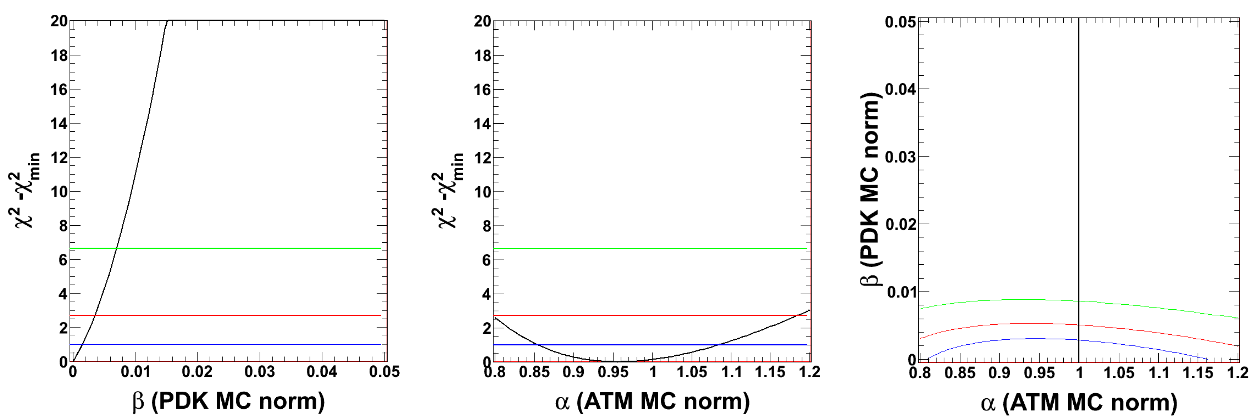

Figure C.19: Data fit for $np \to e^+\nu$, resulting in $\beta_{90CL} = 0.004$ [left].

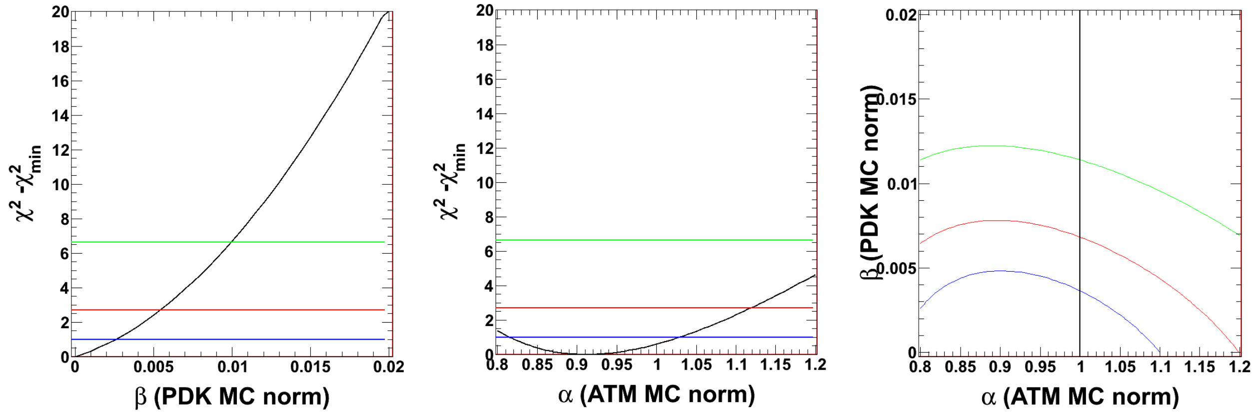

Figure C.20: Data fit for $np \rightarrow \mu^{+}\nu$, resulting in $\beta_{90CL} = 0.005$ [left].

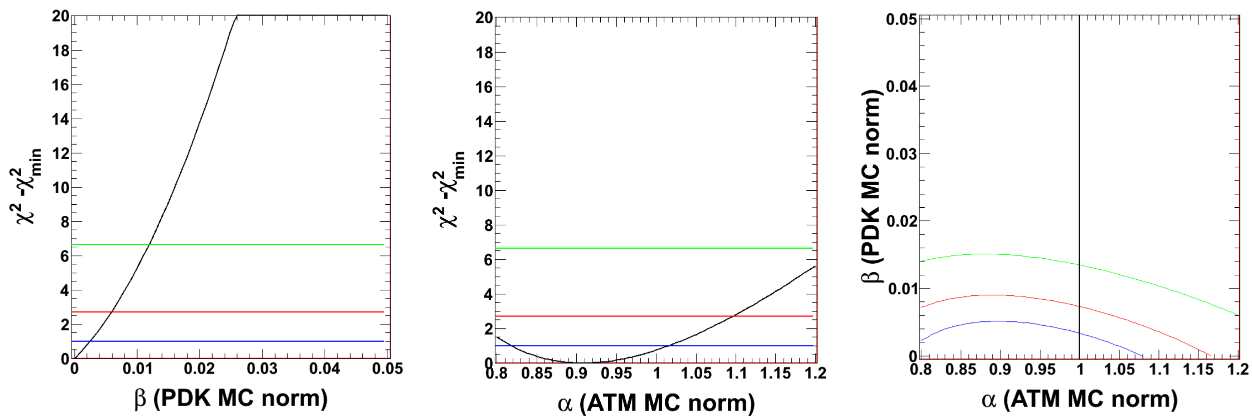

Figure C.21: Data fit for $np \rightarrow \tau^{+}\nu$, resulting in $\beta_{90CL} = 0.006$ [left].